



TECHNISCHE FAKULTÄT DER  
CHRISTIAN-ALBRECHTS-UNIVERSITÄT  
ZU KIEL

# Magnetic nanocomposites

Dissertation  
zur Erlangung des akademischen Grades  
Doktor der Ingenieurwissenschaften  
(Dr.-Ing.)



der Technischen Fakultät  
der Christian-Albrechts-Universität zu Kiel

Amit Kulkarni

Kiel  
March 2012



1. Gutachter: Prof. Dr. Franz Faupel

2. Gutachter : Prof. Dr.-Ing. Eckhard Quandt

Datum der mündlichen Prüfung: 16.04.2012



# Contents

<b>1</b>	<b>General Introduction</b>	<b>3</b>
<b>2</b>	<b>Theory</b>	<b>7</b>
2.1	Nanocomposite morphology . . . . .	7
2.1.1	Percolation theory . . . . .	9
2.2	Magnetism in small dimensions . . . . .	12
2.2.1	Inter particle interaction . . . . .	16
2.3	Tunnel magnetoresistance . . . . .	17
2.4	Ferromagnetic materials in high frequency fields . . . . .	20
2.4.1	Complex permeability . . . . .	21
2.4.2	Ferromagnetic resonance . . . . .	22
2.4.3	Eddy currents . . . . .	25
2.5	Magnetostriction . . . . .	27
<b>3</b>	<b>Fabrication and Characterization Techniques</b>	<b>29</b>
3.1	2D metal/polymer nanocomposite . . . . .	29
3.1.1	Drop coating . . . . .	30
3.1.2	Thermal evaporation . . . . .	30
3.2	3D Nanocomposite thin films . . . . .	34
3.2.1	Sputtering . . . . .	34
3.3	Structural characterization . . . . .	39
3.3.1	Energy dispersive X-ray analysis . . . . .	40
3.3.2	Transmission electron microscopy . . . . .	42
3.4	Magnetic measurements . . . . .	43
3.4.1	Vibrating sample magnetometer . . . . .	43
3.4.2	Magnetoresistance measurement . . . . .	45
3.4.3	High frequency permeability measurement . . . . .	45

---

<b>4</b>	<b>2D Nanocomposites to Monitor Magnetostriction Through Quantum Tunneling</b>	<b>49</b>
4.1	Concept and fabrication details . . . . .	49
4.2	Sensor characterization . . . . .	53
4.2.1	Dependence of sensitivity of sensor on gold layer coverage . . . . .	54
4.2.2	Repeatability . . . . .	56
4.2.3	Aging and preventive measures . . . . .	57
4.3	Model to use metal/polymer composite in cantilever-type actuators . . . . .	60
<b>5</b>	<b>3D Nanocomposites Exhibiting Tunnel Magnetoresistance</b>	<b>65</b>
5.1	Evolution of morphology with respect to metal volume fraction . . . . .	67
5.1.1	Annealing . . . . .	68
5.2	Magnetic properties . . . . .	69
5.3	Magneto-transport properties . . . . .	73
5.3.1	Aging . . . . .	78
<b>6</b>	<b>3D Nanocomposites as Core Material for High Frequency Application</b>	<b>81</b>
6.1	FeCo-SiO <sub>2</sub> system . . . . .	83
6.2	FeNiCo/PTFE multilayer . . . . .	91
6.3	Integration of core into toroidal thin film inductor . . . . .	94
6.4	Alternative approaches . . . . .	98
<b>7</b>	<b>Summary and Outlook</b>	<b>103</b>
	<b>Bibliography</b>	<b>111</b>
	<b>List of Publications</b>	<b>131</b>
	<b>Abbreviations</b>	<b>132</b>



# 1 General Introduction

The way we perceive, use and create materials has changed to a great extent in past many decades. The current trend in creation of ever smaller products and devices needs materials whose response can be intelligently tailored to the changing environment. Microelectronics industry is best example showcasing the continuous shrinkage in weight, size and cost of the devices, especially the communication devices and at the same time offering new functionalities. Thus, functional nanomaterials have attracted great deal of interest as macroscopic properties can be tailored by controlling the microstructure at nanometer level. They include broad range of materials such as nanostructures, nanowires, nanocomposite, nanoparticles etc. Among functional nanomaterials, nanocomposites where nanoscale filler material is embedded in a matrix material are focus of this thesis. They derive benefits from the fact that they combine favorable features of the constituents and secondly, one of the constituent being in nanoscale gives extra degree of freedom with which physical properties can be manipulated to obtain new functional properties [1]. Electronic transport in nanocomposite is function of metal volume fraction and near to percolation threshold electronic transport in these nanocomposites occurs via inter-particle tunneling. Tunnel current is exponentially dependent on the inter particle separation and can be utilized as a detection mechanism for a process which changes the inter-particle separation for example as strain sensor.

By choosing the filler material different functionalities can be obtained such as optical nanocomposites (Au, Ag in insulating matrix exhibiting surface plasmon resonance), magnetic nanocomposites, antibacterial coatings (incorporating Ag which is antibacterial in bio-compatible  $\text{TiO}_2$  matrix) [2] etc. Amongst these, magnetic nanocomposites are of particular interest due to their applications in spintronics [3], magnetic sen-

sors and as core materials for high frequency circuits [4]. Today use of hand held electronic devices is massively growing and driving the trend of miniaturization thus necessitating size reduction and performance enhancement of passive components such as inductors, capacitors which are crucial for high frequency circuits. The operating frequencies of such devices are also steadily increasing typically to GHz range, GSM mobile (Global System for Mobile Communications) 0.8 - 1.9 GHz, GPS (Global Positioning System) 1,2 - 1.6 GHz, and WLAN (Wireless Local Area Network) devices in 2.4 - 2.5 GHz. Present state-of-the-art micro-inductors include planar spirals and consume large area. To improve the performance of high frequency components, integration of soft magnetic core material is most promising [5]. Ideally the permeability of the magnetic layer material increases the inductance, so that the dimensions of the conductors and thus, the ohmic resistance of the micro-inductors can be reduced. Besides, magnetic particles and clusters offer innovative prospects as diagnostic and therapeutic tools in medicine and other life sciences [6].

The main aim of this thesis is to prepare, characterize and tailor host of nanocomposites in accordance with the field of application. In particular the focus is on application in the field of tunnel magnetoresistance, as strain sensor and as materials for high frequency application. Here physical vapor phase deposition technique is employed to prepare nanocomposites and characterized by metal volume fraction with respect to microstructure and magnetic properties. Figure 1.1 provides an overview of nanocomposite studied in this work. **Chapter 2** provides the underlying concepts to understand these nanocomposites and the requirements that they should adhere to in order to use them. **Chapter 3** gives detailed experimental know-how of fabricating the nanocomposites and various characterization techniques to understand the functional properties. Subsequent chapters deal with possible application areas of these nanocomposites. For the sake of simplicity the results and discussions will be presented in three separate chapters (4, 5 and 6). Each chapter focuses on the target nanocomposite application. In **Chapter 4**, development of hybrid material consisting of quasi two dimensional metal-polymer nanocomposite and a magnetostrictive crystal is presented. With this set up it is possible to monitor the strain by easy electrical read out. **Chapter 5** deals with the morphology and magneto-transport properties of ceramic based nanocomposites with respect to metal volume fraction. This knowledge

is further extended to fabricate FeCo-SiO<sub>2</sub> which are promising for high frequency applications (**Chapter 6**).

	Type	Possible application areas described in the thesis
Nanocomposite	Quasi 2D metal/polymer (PMMA + Au)	Stain sensor (chapter 4)
	3D nanocomposites (FeCo-TiO <sub>2</sub> and FeCo-SiO <sub>2</sub> )	Tunnel magnetoresistance (chapter 5) High frequency (chapter 6)
	2-2 Nanocomposites (PTFE + FeNiCo)	High frequency (chapter 6)
	Nanocomposites by dewetting (Co + SiO <sub>2</sub> )	High frequency (chapter 6)

Figure 1.1: Overview of the nanocomposites studied during this thesis



## 2 Theory

### 2.1 Nanocomposite morphology

Nanocomposites can be classified in number ways based on arrangement of constituents, functional properties, type of the constituent. They can also be classified by their functional properties, e.g., as optical, magnetic, antibacterial and magneto-electric nanocomposites. The morphology of nanocomposite depends on type of deposition process, materials used and the order in which they are deposited. In simplest form, two dimensional metal nanoparticles can be formed on a surface, sequential deposition of metal and matrix material leads to multilayer configuration and co-deposition of metal and matrix form 3D network of metallic clusters inside the matrix. In each case the resulting morphology is different and hence functional properties can be tailored to certain extent [7, 8, 9]. In figure 2.1 transmission electron microscopy images are shown as an example for the above mentioned three cases.

The surface energy plays dominant role and is governing factor for the type of growth mode. Since the surface energy of metals  $\gamma_M$  is much higher than the sum of surface energy of polymer/ceramic  $\gamma_P$  and substrate film interface energy  $\gamma_{MP}$ , the metal atoms tend to agglomerate and form clusters to minimize the total energy of the system. This type of growth mode is known as Volmer-Weber growth mode which is found in many systems of metals on insulators, polymers, graphite and mica substrate [13]<sup>1</sup>.

$$\gamma_M > \gamma_{MP} + \gamma_P \quad (2.1)$$

---

<sup>1</sup>page no. 197

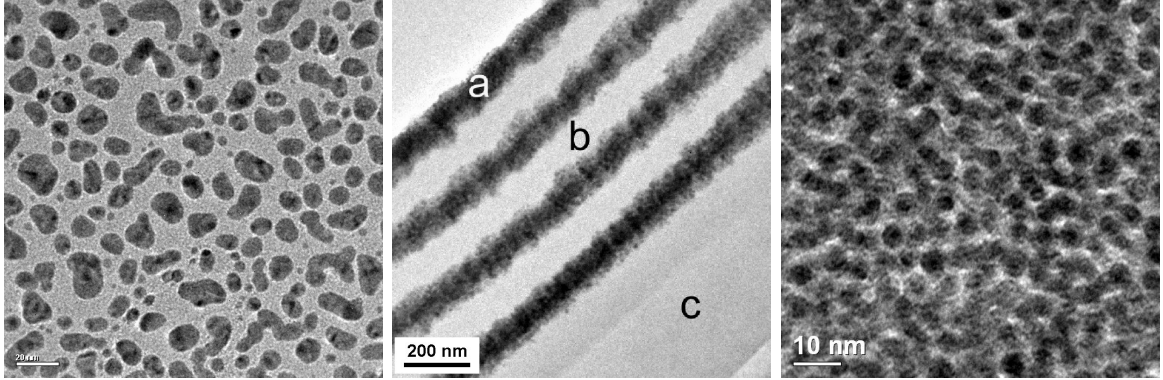


Figure 2.1: TEM images showing morphology of nanocomposites of Au on PMMA [10], multilayer system [11] and FeNiCo-Teflon AF co-evaporated [12] (from left to right).

Let us consider particular case of deposition of metal on polymer surface. Polymers and metals have strongly contrasting properties. Polymers consist of large covalently bonded macromolecules, which are held together by very weak Van-der-Waals interactions. Metals on other hand are densely packed crystalline solids with a high cohesive energy. The cohesive energy of metals is typically two orders of magnitude higher than the cohesive energy of polymers [14]. Interaction between metals and polymers is generally very weak in comparison to the strong metal-metal binding forces. As a consequence, these metals are expected to exhibit a strong aggregation tendency and form clusters (Volmer-Weber growth mode). The size and density of the metal cluster formed depends on several factors. Higher substrate temperature, lower interaction energy and/or lower deposition lead to an enlargement of the metal cluster and vice versa. Furthermore, presence of trapping sites on polymer surfaces will lead to preferential nucleation. These centers may consist of chemically active polymer end groups or impurities. Cluster density can be controlled to certain extent by creation of such trapping site by ion irradiation [15]. A more detailed description of basic processes occurring during the initial stages of polymer-interface have been investigated extensively at the group of F. Faupel [14, 15].

Process described above can be extended to obtain multilayer arrangement simply by sequential deposition of metal and the matrix material. In co-deposition along, with metal atoms now matrix material also impinge on the substrate, metal atoms still

agglomerate and form clusters. These however are covered and embedded into the matrix thus forming a 3 dimensional cluster network in the matrix [16, 17]. The resulting microstructure depends mainly on deposition rate ratio of the two components and substrate temperature.

### 2.1.1 Percolation theory

Percolation theory describes phenomena where at critical point some of the properties of the system undergo abrupt changes [18]. This point where the sharp change in property takes place is called as Percolation threshold. Electrical properties of disordered systems, amorphous semiconductors and materials formed as mixtures of dielectric and metal are some of the best understood applications of Percolation theory [18]<sup>2</sup>. Here, percolation theory is relevant to understand electrical conductivity and magnetic interaction of the nanocomposites which are function of inter-particle separation.

Broadbent and Hammersley [19] were the first to come up with the word Percolation while analyzing an interesting problem related to gas mask design. The motion of gas through a maze was new type of process which differed from diffusion [18]. They called the phenomenon "Percolation" and dealt with it using geometrical and probability concepts. Since then the Percolation theory has been used to interpret an exceptionally wide variety of physical and chemical phenomena as simple as planting tree in a regular order to formation of polymer chain and to calculate the electrical properties of hybrid systems.

Consider a computer generated two-dimensional lattice with occupation probabilities  $P$  0.5 and 0.6 respectively as shown in figure 2.2. Occupied squares are marked with \* and empty squares are ignored. For  $p > 0.6$  a connecting network is established from top to bottom and from left to right. Percolation threshold ( $P_c$ ) is when largest cluster forms. Numerical computations show that for this two-dimensional lattice  $P_c$  is 0.593 [19]<sup>3</sup>.

---

<sup>2</sup>page no. 10

<sup>3</sup>page no. 4

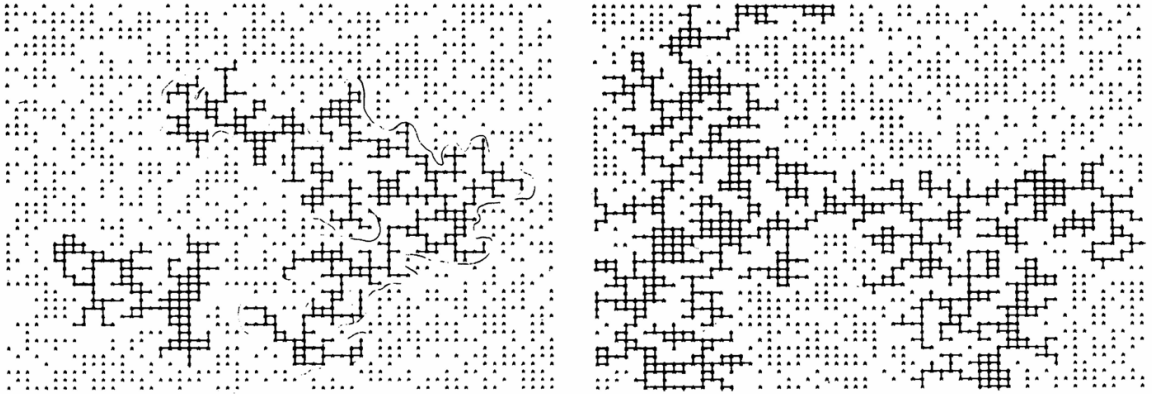


Figure 2.2: Finite two-dimensional lattice below and above percolation [19]

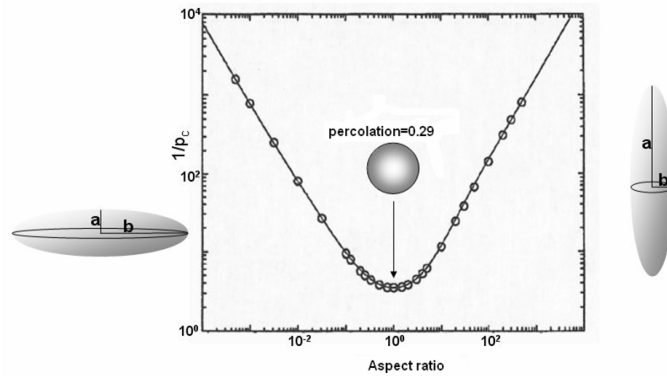


Figure 2.3: Inverse of volume fraction vs aspect ratio of ellipsoids of revolution [20]

### Electrical percolation in composites

Electrical conductivity in nanocomposites is a function of metal volume fraction and accordingly three distinct regimes can be observed.

- Dielectric regime: This regime occurs when metal nanoparticles are well separated by dielectric medium. Metal volume fraction is typically below percolation threshold.
- Transition regime: In this regime metal volume fraction is in the vicinity of percolation threshold. Electrical conductivity is due to thermally activated electron tunneling between metal particles and is very sensitive for any small change in the inter-particle distances.

- Metallic regime: Here the metal volume fraction is above percolation threshold. Metal nanoparticles are in physical contact and form a conducting network.

The cluster geometry itself has a decisive influence on the percolation threshold demonstrated by numerically computed percolation threshold for object size ranging from extreme oblate limit to plate like particles [20]. For spherical particles (figure 2.3) the percolation threshold is 29%. Another important influence on the percolation threshold is the size of the nanoparticle and size distribution because the percolation threshold depends directly on the cluster size. Deviations in the percolation threshold values calculated from numerical solutions are bound to exist, as in reality composite films are far from ideal conditions. Deposition parameters, size distribution, condensation coefficients specific to the material have influence on percolation threshold. Figure 2.4 best shows the influence of preparation parameters and the materials on the percolation threshold. Here the polymer nanocomposites were prepared by co-evaporation [21] and Fe-SiO<sub>2</sub> by co-sputtering [22] techniques. For Ag-Teflon AF and Au-Teflon AF the region in which most pronounced change occurs is at about 42% where as for Au-Nylon it is at 32%. The difference in the percolation threshold values stems from the differences in the microstructure. Condensation coefficients of Ag and Au on Teflon AF surface are very similar thus nucleation and growth process takes place in similar manner, which results in nearly similar microstructure but the condensation of Au on Teflon AF and Nylon is quite different, hence difference in percolation threshold. While the change in the electrical resistivity for the co-evaporated films shows sharp features, the change in Fe-SiO<sub>2</sub> is gradual. This indicates it is not possible to arrive at a particular value for percolation threshold applicable to all nanocomposites but certainly the transition is manifested by change of measurable physical properties.

### **Magnetic percolation**

Magnetic properties of the granular films also depend on the magnetic separation of the particles in the matrix. Magnetic interactions occurring in such systems will be discussed in the section below. Asakura *et al.* [23] studied the magnetic domain percolation in Co<sub>x</sub>-(SiO<sub>2</sub>)<sub>100-x</sub> granular films and the results are summarized in figure 2.5. The electrical percolation for films deposited at room temperature occurs at approx

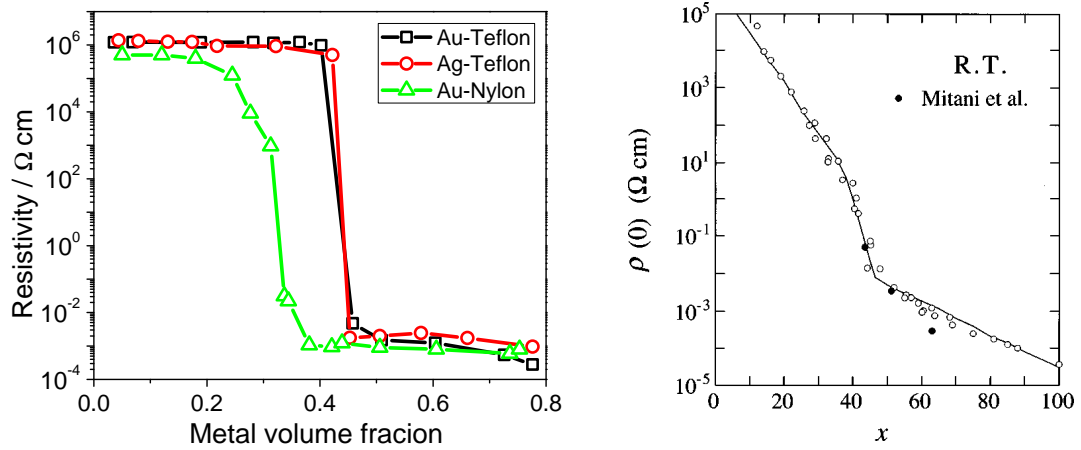


Figure 2.4: Electrical resistivity as a function of metal volume fraction in co-evaporated polymer nanocomposite [21] and co-sputtered Fe-SiO<sub>2</sub> granular films [22].

45%. They found out that the domain structure strongly correlates to the electrical percolation. The stripe domain was observed in the Co-rich region, the divided stripe domain was observed in the intermediate region and the domain structure disappears below the percolation composition ( $x_p$ ), 45%.

## 2.2 Magnetism in small dimensions

The structure sensitive properties of solids show significant size effects when one or more dimensions are in nanoscale. Among magnetic properties, saturation magnetization  $M_s$  is independent of the size [24]<sup>4</sup> on other hand coercivity is not. When the particle size is smaller than the domain wall thickness it cannot have two domains separated by domain wall. In terms of energetic consideration, single domain state is preferred when it costs more energy to create domain wall than to support the magnetostatic energy of the single domain state. The critical size for spheres (with strong anisotropy  $K_u$ ) can be estimated by magnetic domain theory [25]<sup>5</sup> and is given by

$$r_c = 9 \left[ \frac{\sqrt{AK_u}}{\mu_0 M_s^2} \right] \quad (2.2)$$

<sup>4</sup>page no. 359

<sup>5</sup>page no. 305

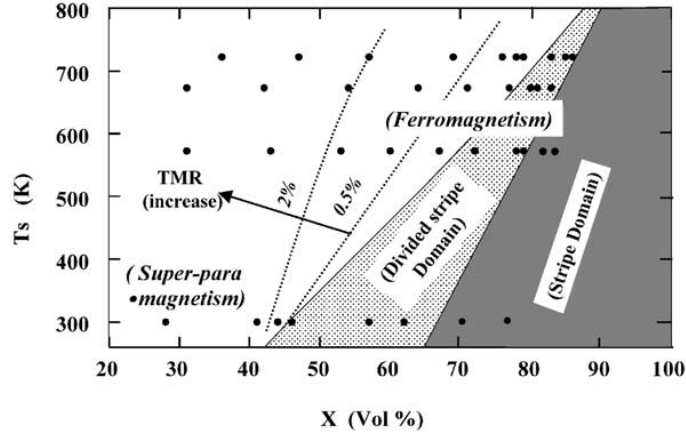


Figure 2.5: Dependence of magnetic domain on the composition  $x$  and substrate temperature for  $\text{Co}_x\text{-(SiO}_2\text{)}_{100-x}$  granular films [23].

where  $r_c$  is the critical size below which particles are single domain,  $A$  is the exchange constant and  $M_s$  the saturation magnetization. The calculated and experimental critical radius for Fe, Co, and Ni are listed in table 2.1. The shape of the particle has large influence on critical radius and non-spherical particles usually have higher  $r_c$ . As mentioned earlier, coercivity shows striking size effects, typically it increases as the particle size is reduced and goes through a maxima before reaching zero. In figure 2.6 summarized are the regions of size ranges in relation to the coercivity. The mechanism by which the magnetization of a particle reverses is different in different regions. One can distinguish three distinct regions beginning with larger particle sizes.

- Multidomain: In this region coercivity decreases as the particle size increases and is proportional to  $1/r^n$ . Magnetization changes by domain wall motion.
- Single domain: As the particle size decreases further, the coercivity increases and reaches highest in this region. Below the critical size  $r_c$  particles are in single domain state. For non-interacting particles coercivity is given by  $H_c \approx a/r^2 - b$  and for exchange-coupled particles  $H_c \approx r^{-6}$ . The magnetization change is by spin rotation and there exist several mechanisms like fanning, curling [24]<sup>6</sup>.

<sup>6</sup>page no. 364

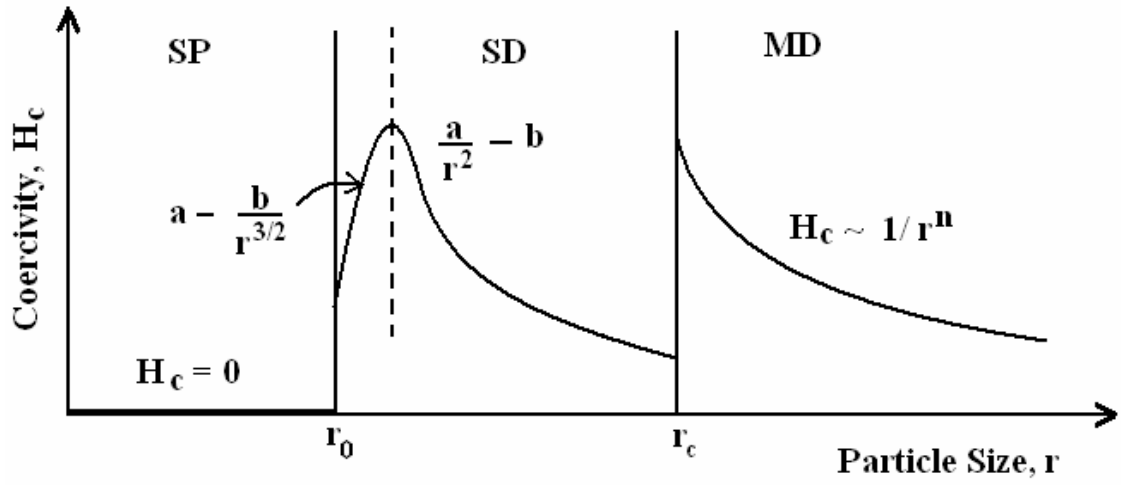


Figure 2.6: Coercivity as function of particle size, showing multidomain (MD) behaviour for  $r \geq r_c$ , single domain (SD) behaviour between  $r_0$  and  $r_c$  and superparamagnetic (SP) region below  $r_0$ . Relationship between the coercivity and the particle size for each region is also shown, from [25]

- Superparamagnetism: Further decrease in particle size results in decrease in the coercivity due to thermal fluctuations and reaches zero at  $r_0$ . The remanent magnetization is no longer fixed as the ambient thermal energy may be strong enough to cause the moment to randomly flip.

	$M_s$ (G)	A (erg/cm)	K (erg/cm <sup>3</sup> )	$r_c$ (the)(nm)	$r_c$ (exp)(nm)
Fe	1710	$5.03 \times 10^{-6}$	$0.8 \times 10^6$	9.8	10.5
Co	1430	$5.40 \times 10^{-6}$	$0.35 \times 10^6$	9.6	10
Ni	485	$2.45 \times 10^{-6}$	$0.05 \times 10^6$	21.2	16

Table 2.1: Single domain size for Fe, Co, Ni from [26], here 'the' refers to theoretical and 'exp' to experimental.

The minimum particle radius which is stable against the ambient thermal demagnetization can be estimated from following relation [25]<sup>7</sup>

<sup>7</sup>page no. 307

$$r_0^{1yr} \approx \left( \frac{10k_bT}{K_u} \right)^{1/3} \quad r_0^{1s} \approx \left( \frac{6k_bT}{K_u} \right)^{1/3} \quad (2.3)$$

For spherical particles with anisotropy constant  $K_u = 10^5 J/m^3$  approximate superparamagnetic radii for stability over 1 year and 1 second are 7.3 nm and 6 nm respectively. Superparamagnetic state is characterized by two experimental features: one there is no hysteresis and second the magnetization curves measured at different temperatures superimpose in a plot of  $M$  vs  $H/T$ . Deviations from the  $H/T$  may be possible due the broad distribution of particle sizes or anisotropy effects. In superparamagnetic state, for a noninteracting system the magnetization curves are described by Langevin function.

$$M = M_s L \left( \frac{\mu H}{k_B T} \right) \quad (2.4)$$

where  $L$  is Langevin function. Magnetic measurements of superparamagnetic particles can be used qualitatively to estimate the particle size. By integration of Langevin function over the particle size, total magnetization of the sample can be determined. Since in all real systems there exists a particle size distribution, the resultant magnetization must take this into account and hence given by [27]

$$M = M_s \int L \left( \frac{M_s V H}{k_B T} \right) f(V) d(V) \quad (2.5)$$

where  $f(V)$  is size distribution function. From magnetization as a function of field with known size distribution, function average particle size and width of the distribution function can be calculated [28]. Many distribution functions have been suggested depending on the preparation conditions, generally log normal size distribution is used for nanocomposites prepared by physical vapor deposition technique [29, 30, 31].

When particles of certain size are cooled below a critical temperature superparamagnetic state will disappear as the characteristic relaxation time ( $\tau$ ) for a particle's

moment varies exponentially with temperature. The magnetization switches to a stable state as the temperature is reduced. The temperature at which this occurs is called Blocking temperature  $T_B$ . For spherical particles with uniaxial anisotropy and relaxation time of 100 sec (roughly the time required to measure the remanence of a sample [24]<sup>8</sup>),  $T_B$  is given by

$$T_B = \frac{KV}{25k} \quad (2.6)$$

where  $K$  anisotropy constant,  $V$  volume of the particle and  $k$  Boltzmann constant. Transition to stable behavior occurs at temperature below  $T_B$ .

### 2.2.1 Inter particle interaction

Superparamagnetic description refers to non-interacting particles, however the situation is quite different when the particles are in contact. The main types of magnetic interactions associated with fine-particle assemblies are (1) dipole-dipole interactions (2) exchange interactions through the surface of the particles which are in close contact and (3) interactions associated with nanocomposite, where magnetic nanoparticles are dispersed in non-magnetic matrix [32]. In the case of metallic matrix, Rudermann-Kittel-Kasuda-Yosida (RKKY) like interactions [33, 34, 35] are known to occur and super exchange interactions when the matrix is insulating [32].

For a magnetic particle system, ferromagnetic exchange interaction may occur when the average particle size and the distance between them is smaller than the exchange length  $L_{ex}$  [36]. The interaction tends to align the magnetic moments of the neighboring particles thus overcoming the magnetocrystalline anisotropy and demagnetization effects of individual particles. The existence of exchange coupling can be observed experimentally by plotting  $\Delta M(H)$  curves. Stoner-Wohlfarth theory describes the behavior of an assembly of single domain non-interacting particles with uniaxial anisotropy. Wohlfarth relation [37] states a simple relationship involving the behaviour of remanence

---

<sup>8</sup>page no.386

$$I_{DCD}(H) = I_{IRM}(\infty) - 2I_{IRM}(H) \quad (2.7)$$

where  $I_{DCD}(H)$  is Direct Current Demagnetization curve (DCD) and  $I_{IRM}(H)$  is the Isothermal Remanent Magnetization (IRM) curve. IRM curve is obtained by increasing the field to a value of  $H$  and then measuring the magnetization at zero field with the sample initially in demagnetized state. DCD curve is generated in the same manner except that the sample is initially saturated in a positive field and the remanent magnetization is measured after applying a field  $-H$  [38]. However many real systems may not satisfy the Stoner-Wohlfarth model and deviate from the equation 2.7. It was Henkel [39] who first proposed that the deviation from this behavior in real systems was caused by the interactions between particles. He plotted  $I_{IRM}(H)$  against  $I_{DCD}(H)$  this is known as the Henkel plot.

$$\Delta M(H) = I_{DCD}(H) - [1 - 2I_{IRM}(H)] \quad (2.8)$$

If  $\Delta M(H)$  is positive, the interaction are ferromagnetic like and the negative values indicate magnetization tends to be antiparallel.

## 2.3 Tunnel magnetoresistance

Tunneling is a phenomena involving charge transport between two conducting electrodes separated by a dielectric few nanometers in thickness. The phenomena arise due to the wave nature of the electrons and can only be described by quantum mechanics. Consider a particle with Energy  $E$  approaching a potential barrier (let  $V$  and  $L$  be height and width of the barrier) shown schematically in figure 2.7. In quantum mechanical treatment of the electron considering the wave particle duality the particle can overcome the potential barrier and there exist a certain probability that the particle can be found on the other side of the barrier [40]. The evanescent nature of charge transport through the tunnel barrier leads to the exponential dependence of

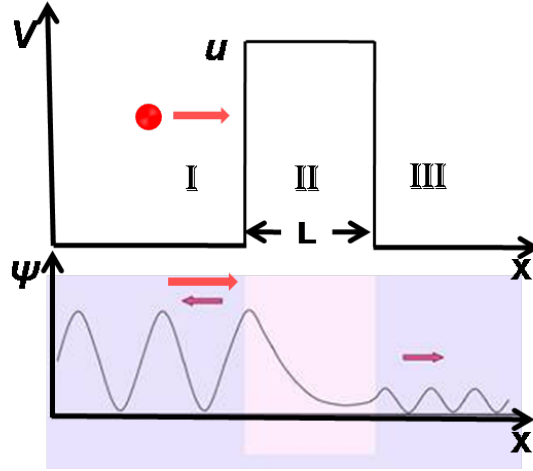


Figure 2.7: Schematic showing the particle tunneling through a finite potential well and the wave function of the particle as a function of the tunnel barrier width

tunneling current with the barrier thickness. The relationship between the tunneling current and the barrier thickness is given by [41]

$$I(V) = f(t_b) \left\{ \left[ \bar{\phi} - \frac{V}{2} \right] e^{[1.025\sqrt{\bar{\phi} - \frac{V}{2}}t_b]} - \left[ \bar{\phi} + \frac{V}{2} \right] e^{[1.025\sqrt{\bar{\phi} + \frac{V}{2}}]} \right\} \quad (2.9)$$

where  $I$  is the tunneling current,  $\bar{\phi}$  and  $V$  are the average tunnel barrier height and bias voltage across the junction in volts and  $t_b$  is the barrier thickness in angstroms. The exponential dependence of tunneling current to the barrier width can be used e.g., in strain sensors, in tunnel magneto resistance and numerous other real time devices.

When the electrodes are of ferromagnetic material, a further interesting phenomenon takes place known as tunnel magneto resistance (TMR). Julliere designed a junction involving two ferromagnetic layers (FM) separated by a insulating layer (Fe/Ge/Co) where electrons tunnel from Fe layer to Co through the Ge layer [42] giving rise to TMR ratio of 14% at 4K. This phenomenon was explained by taking into account that the electron spin is conserved during tunneling and the tunneling current depends on the density of states of the FM layer. The tunnel current depends on the

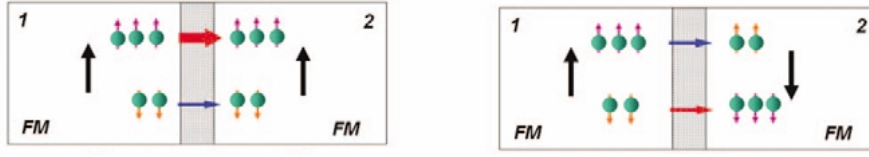


Figure 2.8: Schematic of the TMR effect in magnetic tunnel junctions. A change from the parallel configuration (left) to the antiparallel configuration (right) of the magnetizations of the two electrodes results in an exchange of the spin subband for electrode 2, causing a corresponding change in the conductance from [43].

relative orientation of the magnetic moments of the two magnetic layers. The tunnel magnetoresistance is then defined as

$$TMR = \frac{R_{AP} - R_P}{R_P} \quad (2.10)$$

where  $R_P$  and  $R_{AP}$  are the resistance in parallel and antiparallel configurations respectively. As explained by Zhu *et al.* [43] the origin of TMR arises from the difference in the electronic density of states (DOS) at the Fermi level  $E_F$  between spin-up and spin-down electron. Electrons preserve their spin orientation during the tunneling process therefore they can only tunnel into the subband of the same spin orientation. Thus, the tunneling conductance is proportional to the product of the Fermi level DOS values of the two electrodes with same spin orientation. A change from the parallel magnetization configuration (figure 2.8 left) to the antiparallel configuration (figure 2.8 right) of the two electrodes will result in an exchange between the two spin subbands of one of the electrodes for the tunneling process. Consequently, a corresponding change in the conductance will be seen, provided that the Fermi-level DOS values are different for the two spin subbands [43].

### TMR in nanocomposites

Analogous to magnetic tunnel junctions the nanocomposite film can be thought as assembly of many FM/I/FM junctions. Inoue and Maekawa [44] explained the tunnel magnetoresistance in nanocomposite films based on FM/I/FM neglecting the correla-

tion between magnetic moments of neighboring particles. The tunneling conductance in granular films can be expressed as

$$G = G_o [1 + P^2 m^2] \exp \left( -2\sqrt{2\kappa C/kT} \right) \quad (2.11)$$

where P is spin polarization and  $m = (M/M_S)$  is relative magnetization of the system. The magnetoresistance is give as

$$\Delta\rho/\rho_0(H) = \frac{G(0)^{-1} - G(H)^{-1}}{G(0)^{-1}} = \frac{-P^2(M/M_S)^2}{1 + P^2(M/M_S)^2} \quad (2.12)$$

The theory is able to explain well the observed MR dependence on  $m^2$  in many systems [45] and the weak temperature dependency. In the model presented by Inoue *et al.* exchange interaction was considered to be negligibly small thus the MR ratio dependence on temperature is smaller than  $T^{-1}$ . However, in some granular films [46, 47] this theory does not explain the strong enhancements of MR observed at low temperature (below 100 K). Mitani *et al.* [48] explained the phenomena by considering higher order tunneling process between large granules through intervening small granules taking into account the broad particle size distribution. The MR ratio is given by

$$\Delta\rho/\rho_0 = 1 - (1 + P^2 m^2)^{-(n^*+1)} \quad (2.13)$$

The structural feature of granular systems was modeled with assumption that large granules with size  $n\langle d \rangle$  and charging energy  $\langle E_c \rangle/n$  are separated by an array of  $n$  granules with average size  $\langle d \rangle$  and charging energy  $\langle E_c \rangle$  on a conduction path, as illustrated in figure 2.9. These processes are negligible at higher temperatures as the tunneling takes place through particles of similar sizes [27, 49].

## 2.4 Ferromagnetic materials in high frequency fields

In the following section a brief description of important concepts related to high frequency behavior of ferromagnetic materials will be presented. When a high frequency

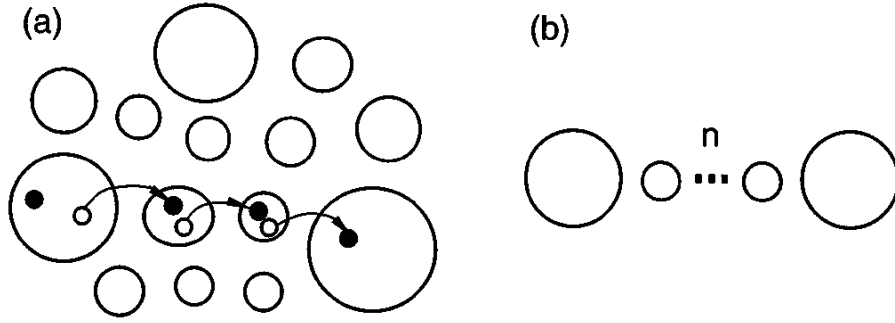


Figure 2.9: (a) Schematic illustration of granular structure and a higher-order tunneling process where a charge carrier is transferred from the charged large granule (left), through the two small ones, to the neutral large one (right). (b) Model structure used for conductivity calculation [48].

alternating magnetic field is applied to a substance certain resonance effects are observed at particular values of the frequency and magnitude of the field [24]<sup>9</sup>.

### 2.4.1 Complex permeability

When a magnetic material is subjected to an ac magnetic field, the magnetic induction ( $B$ ) lags behind magnetic field strength ( $H$ ) by the phase angle  $\delta$  because of presence of losses. Magnetic field strength and magnetic flux in the sample then can be defined as follows

$$H(t) = H_o e^{i\omega t}, B(t) = B_o e^{i\omega(t-\delta)} \quad (2.14)$$

where  $H_o$  and  $B_o$  are the maximum amplitude,  $\omega$  the angular frequency,  $t$  time and  $\delta$  being the phase angle. The real and imaginary part of the permeabilities are defined as

$$\mu = \frac{B}{H} = \frac{B_o}{H_o} e^{-i\delta} = \frac{B_o}{H_o} \cos \delta - i \frac{B_o}{H_o} \sin \delta = \mu' - i\mu'' \quad (2.15)$$

<sup>9</sup>page no. 433

The ratio of imaginary to real part  $\tan \delta$  is called loss factor or the quality factor of the high frequency (HF) material. If there are no losses then  $B$  and  $H$  are in phase and  $\mu''$  is zero.

$$\tan \delta = \frac{\mu''}{\mu'} \quad (2.16)$$

This quality factor is very significant which comes into discussion very often. The lower the imaginary part, higher will be the quality factor and better the performance of HF material. The complex permeability and the quality factor depend on many parameters such as loss mechanisms in the HF material, limitation caused by resonance and anisotropy distribution in the HF material. Each will be given a special attention in following paragraphs.

## 2.4.2 Ferromagnetic resonance

The effect of an applied static magnetic field on atomic moments is the precession of atomic moments about the applied field at a frequency proportional to  $H$  as each atom possesses a certain angular momentum and magnetic moment. This frequency is called as Larmor frequency given by

$$\omega_L = \gamma \vec{H}_{eff} = g \frac{e}{2m} \vec{H}_{eff} \quad (2.17)$$

where  $\gamma$  is a constant called gyromagnetic ratio,  $m$  and  $e$  electron mass and charge respectively and  $H_{eff}$  is effective value of the external dc field at the location of the electron. If there were to be no damping processes to influence the precession of the magnetic moment, the  $H_{eff}$  will never become parallel to the applied field, it will only precess. In reality, however, the magnetization aligns with the applied magnetic field as result of damping processes (figure 2.10).

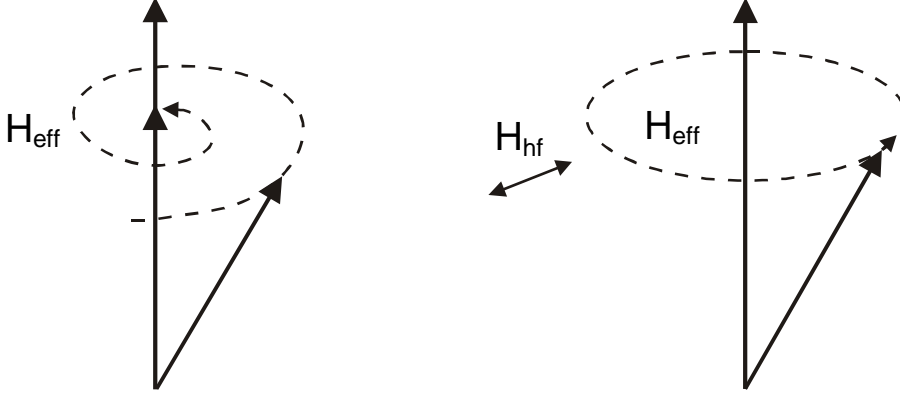


Figure 2.10: Schematic representation of Spin precession around an effective field  $H_{eff}$  for damped (left) and undamped (right) with high frequency alternating field  $H_{hf}$ .

When an alternating HF field is applied at right angles to the applied static magnetic field and when the Larmor frequency equals the HF field, resonance occurs. A sharp drop in the transmitted HF field is observed. This phenomenon is called ferromagnetic resonance (FMR) and the frequency at which FMR occurs is called as FMR frequency. Kittel [50] formulated the equation for calculating the FMR frequency considering the effective field  $H_{eff}$ . The formulation of the ferromagnetic resonance frequency is based on inner effective field and not on the external applied field. Thus the resonance condition is a classical equation of motion of magnetization, given by

$$\frac{d\vec{M}}{dt} = -\gamma \vec{M} \times \vec{H}_{eff} \quad (2.18)$$

The internal field here accounts for the magnetocrystalline anisotropy and the demagnetizing field arising due to the physical confinement of the magnetic sample. It is defined by the shape of the magnetic sample. The resonance frequency is given by

$$f_{FMR} = \frac{\gamma}{2\pi} \sqrt{[H_{eff} + (N_y - N_z)M_s][H_{eff}(N_x - N_z)M_s]} \quad (2.19)$$

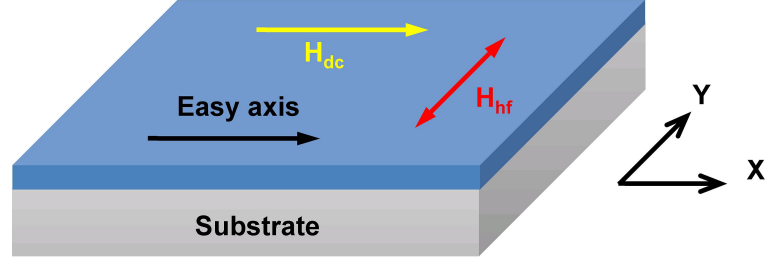


Figure 2.11: Schematic representation of arrangement of the film during high frequency measurements, the HF excitation field is perpendicular to the easy axis of the magnetic film and to the external static field  $H_{dc}$ .

Based on considerations of Landau and Lifshitz the theoretical description of the damping spin precession from equation of motion is given by

$$\frac{d\vec{M}}{dt} = -\gamma\vec{M} \times \vec{H}_{eff} + \frac{\gamma}{M} \alpha [M \times (M \times \vec{H}_{eff})] \quad (2.20)$$

This Landau-Lifshitz equation describes the course of complex permeability for damping constants  $\alpha$  from 0.001 to 0.2. Figure 2.11 shows the schematic drawing of the arrangement of fields involved (which is similar to the high frequency permeameter used in this work). A thin film lies in the XY plane with its easy axis along X-axis. The applied dc magnetic field is in the plane of the film along X-axis and perpendicular to the exciting AC field  $H_{HF}$ . Then the complex permeability  $\mu_r$  is given by

$$\mu_r = \mu'_r - i\mu''_r \quad (2.21)$$

$$\mu'_r = \gamma^2 \cdot \frac{M_s^2(\omega_0^2 - \omega^2)}{(\omega_0^2 - \omega^2)^2 + (4\pi\lambda\omega)^2} \quad (2.22)$$

$$\mu''_r = \gamma^2 \cdot \frac{4\pi\lambda\omega M_s^2}{(\omega_0^2 - \omega^2)^2 + (4\pi\lambda\omega)^2} \quad (2.23)$$

where  $\omega$  is the angular frequency and  $\omega_0 = 2\pi f_{FMR}$  and is given by

$$f_{FMR} = \frac{\gamma}{2\pi} \sqrt{M_s(H_k + H_{dc})} \quad (2.24)$$

for the case where  $\omega \rightarrow 0$  from equation 2.22, we have

$$\mu'_r = \frac{M_s}{(H_k + H_{dc})} + 1\mu''_r = 0 \quad (2.25)$$

### 2.4.3 Eddy currents

In addition to the losses due to ferromagnetic resonance a conductive material shows eddy current losses. Eddy currents are electric currents induced in a material with finite conductivity due to frequency dependent external magnetic fields. These electric currents in turn induce magnetic field within the material which oppose the changing external field, thus shielding the magnetic field from penetrating the material there by reducing the permeability at higher frequencies. The cut off frequency due to eddy currents,  $f_{EC}$ , is given by [51]<sup>10</sup>

$$f_{EC} = \frac{4\rho}{\pi\mu_0\mu_a d^2} \quad (2.26)$$

where  $\rho$  is resistivity of the material. The roll-off due to eddy currents can be increased to higher frequency by choosing smaller effective particle diameter and electrical resistivity as high as possible. One more parameter which is associated with eddy currents to be addressed is the penetration depth of the magnetic field. The magnetic field produced by the eddy currents always opposes the change in magnetization, so that the magnetization is damped away inside the specimen. The depth ( $\delta$ ) at which the magnetic field is reduced by the factor  $1/e$  is called the skin-depth and it is given by [52]<sup>11</sup>

---

<sup>10</sup>page no. 609

<sup>11</sup>page no. 552

$$\delta = \sqrt{\frac{\rho}{\pi f \mu_r \mu_0}} \quad (2.27)$$

The film thickness of the material used should be lesser than  $\delta$ . The computed skin depth values as a function of frequency, resistivity and permeability for FeCo-SiO<sub>2</sub> nanocomposite is given in chapter 6.1.

### Requirements for HF application

Considering all the parameters mentioned above, conditions and material parameters required for effective use of HF material in micro-inductor are as follows.

1. The real part of the hard axis permeability at the operating frequency should be as high as possible since, in ideal case the inductance of a micro-inductor is proportional to the HF permeability. Therefore  $M_s/H_k$  should be large (equation 2.25).
2. Cut-off frequency due to ferromagnetic resonance must be higher than the operating frequency. Controllable anisotropy field  $H_k$  ensures large  $f_{FMR}$  (equation 2.24). It is to be noted that point 1 and 2 are contradictory to each other, therefore a trade-off exist between permeability and FMR frequency.
3. Cut-off frequency due to eddy currents must be higher than the operating frequency. High frequency material should possess electrical resistivity as high as possible in order to suppress eddy currents (equation 2.26).
4. Magnetic losses in the material,  $\tan \delta$  (equation 2.16) must be as small as possible otherwise overall quality factor of the micro-inductor suffers.

## 2.5 Magnetostriction

Magnetostriction is a phenomenon where the physical dimensions of a ferromagnetic material changes in response to change in the magnetization state of the material [52]<sup>12</sup>. The effect was first observed by James P. Joule in 1842 hence also known as Joule magnetostriction (change of shape in the direction of the applied magnetic field). In simplistic form magnetostrictive factor  $\lambda$  can be defined as

$$\lambda = \frac{\text{change in length}}{\text{original length}} = \frac{\Delta l}{l} \quad (2.28)$$

Materials that elongate in the direction of applied field have positive  $\lambda$  and conversely materials with negative  $\lambda$  shrink. However  $\lambda$  is anisotropic, the magnitude depends on the direction of the applied magnetic field and crystallographic direction in which it is measured. The physical origin of magnetostriction stems from spin-orbit coupling which is relatively weak, a small magnetic field is enough to rotate the spins from easy direction [24]<sup>13</sup>. Macroscopically, the magnetostriction can be explained based on the domains. The external magnetic field leads to migration of domain walls within the material followed by rotation of the domains. These two mechanisms allow the material to change the domain orientation which in turn causes a dimensional change.

The relatively small magnetostriction coefficient of pure elements (Fe, Co and Ni) limits their use in engineering. A.E. Clark and his co-workers developed giant magnetostrictive materials containing Fe, Dy and Tb of the form  $Tb_xDy_{1-x}Fe_2$  since then known as Terfenol-D. Magnetically induced strain in Terfenol-D is up to  $2 \times 10^{-3}$  under a mechanical bias at room temperatures and is the most commonly used engineering magnetostrictive material for many transducer and actuator applications [53, 54]. In this work Terfenol-D of dimension 15 mm x 2.53 mm x 6.4 mm made by the company ETREMA Products, Inc.<sup>14</sup> is used to demonstrate the strain sensing capabilities of quasi 2 dimension metal-polymer nanocomposite.

---

<sup>12</sup>page no. 343

<sup>13</sup>page no. 257

<sup>14</sup><http://www.etrema-usa.com/products/terfenol/>



## 3 Fabrication and Characterization Techniques

In general, it should be possible to synthesize the nanocomposites by any method capable of producing nano size particles [55]. Over the years many techniques such as wet chemistry [56], physical vapor phase deposition, pulsed laser deposition [57, 58] and chemical vapor deposition have been established. Physical vapor phase deposition (PVD) provides certain advantages in terms of compatibility with the standard fabrication processes in microelectronics thus offering easy integration into ICs. As it has been emphasized throughout this thesis, control over the metal volume fraction is crucial to fine tune the functional properties, PVD is better suited [16] while wet chemical methods offer better control over particle size and shape [59]. Moreover by PVD technique different microstructures like multilayer, composites and nanocolumns [60] can be produced without changing the components and process significantly. PVD technique includes both evaporation and sputtering. In this chapter physical vapor phase deposition technique as a tool to produce nanocomposite will be presented. Preparation method employed and the characterization techniques necessary will follow through in subsequent sections.

### 3.1 2D metal/polymer nanocomposite

Metal-polymer nanocomposites were prepared by combination of wet chemistry and PVD; first by drop coating of the polymer film and then thermal evaporation of Au on to it. Formation of metal clusters is due to strong metal-metal binding forces compared to the weak interaction between metal and polymer (chapter 2.1).

### 3.1.1 Drop coating

Drop coating is probably the simplest technique available to form organic films [61], all one needs is a solution and a balanced horizontal work surface. The procedure is to apply the solution on to the substrate which results into film after evaporation of the solvent. The solution consists of measured quantity of the material to be coated, in this case organic molecule and an appropriate solvent. A micropipette can be used to apply the solution as it can measure accurately and give out small volumes of solution. This will make sure that every time same amount of solution is dispensed onto the substrate. The advantage of drop coating lies in it being a very simple procedure and relatively thick films can be produced with good homogeneity. This process can be easily adapted for disproportionate substrate sizes. Drop coating has some disadvantages like the formation of borders at the edges of the substrate and precipitation. Precipitation can be avoided to certain extent by choosing the right combination of solvent and material of interest.

### 3.1.2 Thermal evaporation

In this process atoms are removed from the source material by thermal means and are controllably transferred to the substrate where they condense. Source material is heated to a high vapor pressure until they evaporate. This process is carried out in vacuum ( $p < 10^{-6}$  mbar) to avoid reaction between vapor and the atmosphere. Mean free path of atoms at these low pressures is in the range of chamber dimensions (should be) so that the vapor can travel from the evaporator and condense on the substrate. The rate of evaporation is governed by the temperature of the crucible, type of material that is being evaporated and the pressure. Several techniques are available in use to heat the source material, in this work resistively heated evaporation source is employed. The most common and simplest case is evaporation of metals however, alloys and inorganic compounds can also be evaporated [62]. Thermal evaporation of alloys is not straight forward as the vapor pressure of the individual elements may vary leading to preferential deposition of the element with highest vapor pressure. Thus

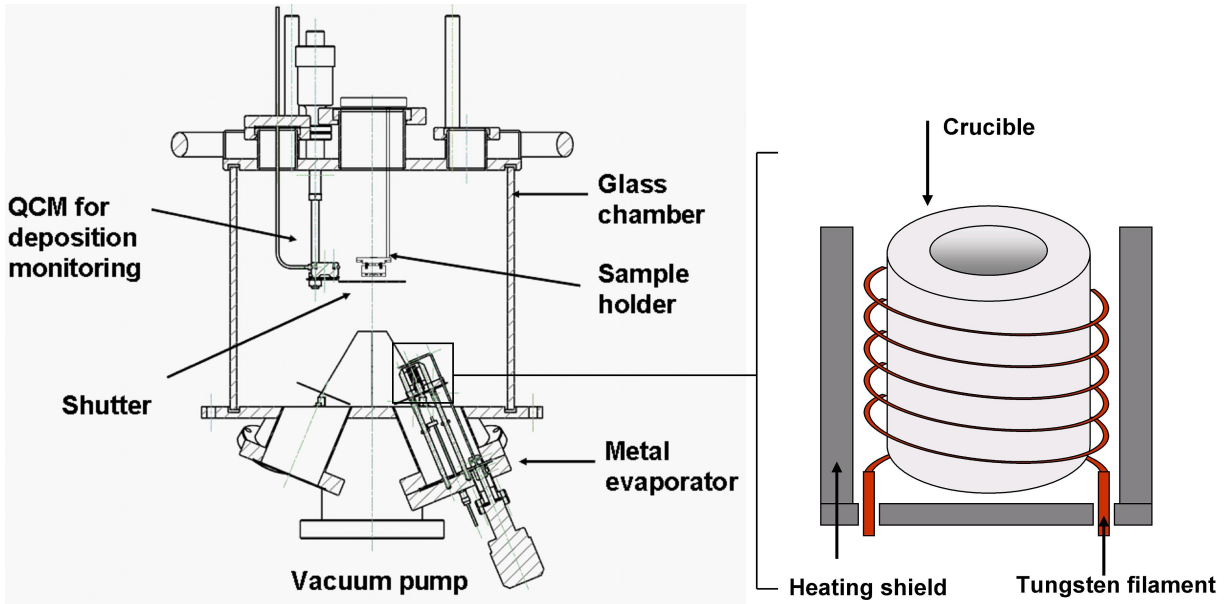


Figure 3.1: Schematic drawing of the vacuum system used for thermal evaporation of Au. The chamber is equipped with a thermal evaporator and a sample holder to measure the electrical current *in-situ*.

the composition of evaporated film is different from that of starting material [13]<sup>1</sup>. To overcome this separate evaporation source may be used for individual elements.

## Equipment

Thermal evaporation set up used in this work is shown figure 3.1. The chamber<sup>2</sup> is made up of cylindrical borosilicate glass with stainless steel bottom and top plates. The bottom plate has arrangement to connect to pumping system and three evaporators through DN63CF flanges. Similarly, the top lid has openings for sample holder and for any other accessories needed. Vacuum in the chamber is provided by a set of rotary and turbo molecular pump. Evaporator consists of a crucible made up of refractory material, Boron nitride or Alumina. Crucible is surrounded by tungsten filament for resistive heating as shown schematically in 3.1. Thermal evaporation of Au was carried out at  $\approx 80$  W (4.0 A and 20 V).

<sup>1</sup>page no. 85

<sup>2</sup>The chambers were designed and constructed by Dipl.-Ing. (FH) Stefan Rehders, and electronics by Dipl.-Ing. (FH) Rainer Kloth

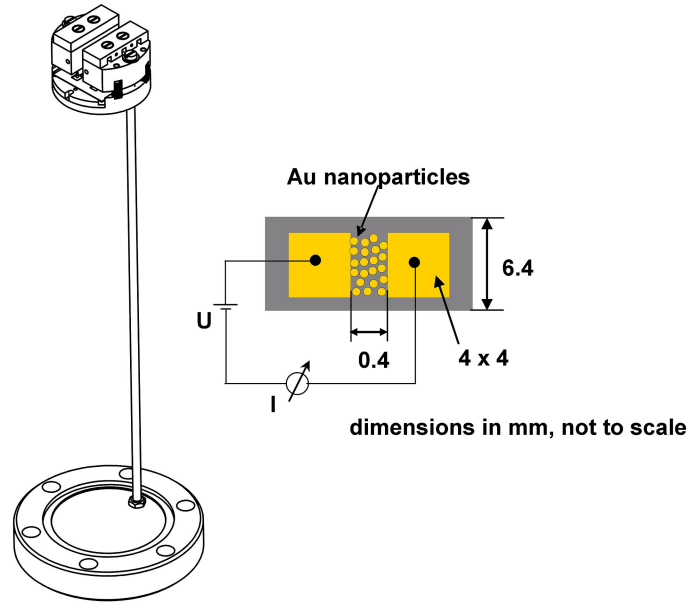


Figure 3.2: Schematic drawing of the sample holder to measure *in-situ* electrical current during deposition.

The chamber is equipped with a sample holder which can measure the electrical current arising due to the metal atoms between two contact pads 3.2. It consists of spring operated gold pins which establish contact with the contact pads on the substrate. During the evaporation process with this set up, one can measure current and temperature on the substrate simultaneously. The deposition rate was monitored through Quartz crystal microbalance. Here the rate was treated as an indicator of evaporation process rather than accurate measurement as the amount of Au deposited on each sample was based on the tunneling current. First step is to get percolation curve for the configuration of contact pad and polymer. Then the amount of Au deposited can be tuned in a way that the final room temperature current of the samples is in the percolation region (chapter 4.1).

Figure 3.3 shows a typical *in-situ* current measurement during Au deposition. Point A marked in figure 3.3 is when the evaporator was turned off. After turning off the evaporator, current starts to decrease and it takes a while to reach a steady state. Energy supplied by the heat to source material gives up upon condensation and is the principle source for substrate heating. During evaporation process the substrate is at temperature higher than the room temperature due to heat flux from the evaporator.

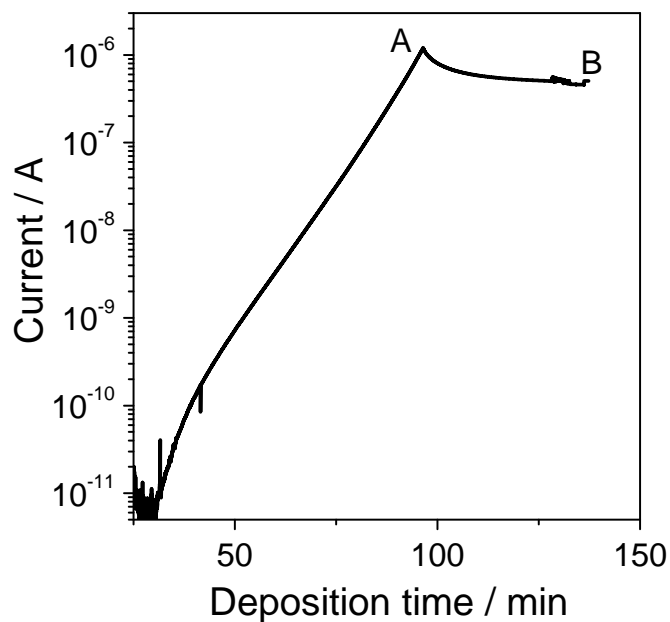


Figure 3.3: An example of *in-situ* current measurement during evaporation of Au on to a drop coated polymer, showing the drop in the current after switching off the evaporator (see text).

Therefore the current measured is not only due to the arriving Au atoms but also due to the heat flux and hence a drop in the current is apparent after switching off the evaporator. The amount of drop depends mainly on the evaporation rate, length of evaporation and sample temperature during evaporation process. Even though all samples were cooled down to 3 °C, the measured substrate temperature during evaporation was 50-60 °C. The measured current of the sample is due to surface conductivity by cluster film. Hence the classical resistivity cannot be estimated as there is no uniform closed film.

## 3.2 3D Nanocomposite thin films

### 3.2.1 Sputtering

Sputtering is one of the most widely used physical vapor deposition technique to deposit thin films. It refers to the process of emission of atoms, ions and molecules from a solid surface (target) which is bombarded with high energy ions in an electric field. First, plasma is initiated by applying several kilovolts of voltage to the target in a sputtering gas medium in which a discharge is initiated and sustained. Inert gas, typically Argon, is used as sputtering gas for no-reactive sputtering and mixture of Ar/O<sub>2</sub> and Ar/N<sub>2</sub> are used in the case of reactive sputtering. Plasma is a partially ionized gas consisting of equal numbers of positive and negative charges and neutral molecules [63]<sup>3</sup>. Once the plasma is generated positive ions in the plasma are attracted to the negatively charged target (cathode). This collision creates a momentum transfer and ejects atomic size particles from the target. These particles traverse the chamber and are deposited onto the substrates. In addition to the target material, secondary electrons, disrobed gases, negative ions and radiations are emitted from the target as well. The secondary electrons may collide with neutral gas species ionizing the gas further. In figure 3.4 a simple model of some the processes that may occur during ion solid interaction are shown developed by Wehner and Anderson [64], where chemical effects were ignored and the atoms were treated as spheres.

Depending upon the target material DC, pulsed DC, RF power supplies are used. DC sputtering is limited to electrically conductive targets. To sustain a DC-discharge, the electrodes have to be conducting. In the case of deposition of dielectric films, the electrodes will be charged up due to the accumulation of positive or negative charges and the discharge will be extinguished. Deposition of non-conducting thin films by DC sputtering requires impossible high voltage [13]<sup>4</sup>, therefore RF sputtering was invented. Here instead of direct current, an ac signal in MHz range<sup>5</sup> is applied to the electrodes and the charge accumulated during half cycle will be partially neutralized by

---

<sup>3</sup>page no. 49

<sup>4</sup>page no. 121

<sup>5</sup>13.56 MHz is specially reserved for this purpose

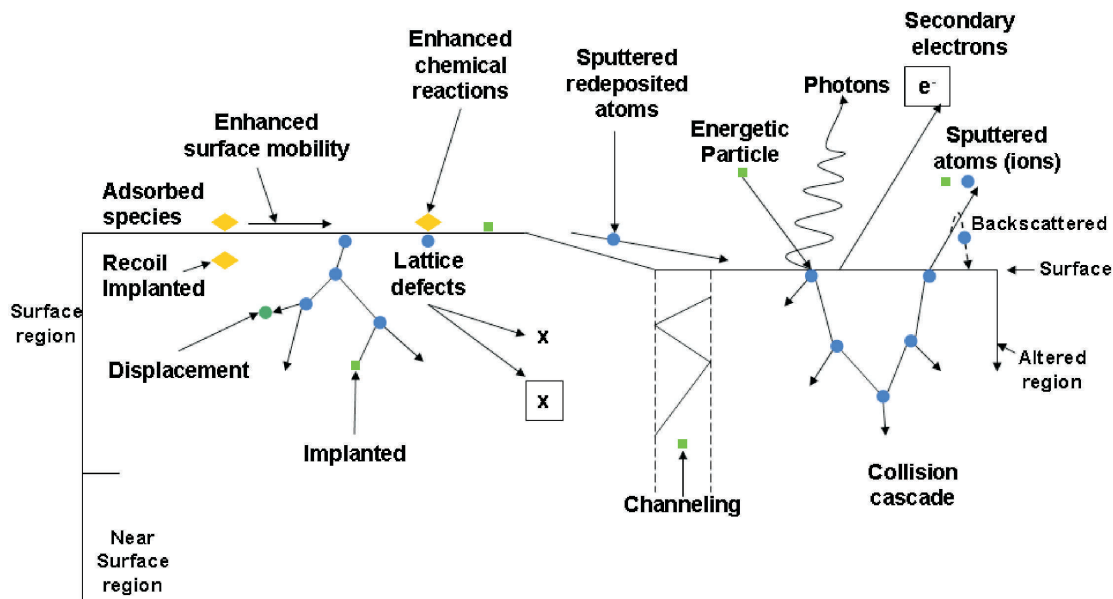


Figure 3.4: Schematic of model developed by Wehner and Anderson describing the processes that may occur during ion solid interaction [64]

the opposite charge accumulated during the next half cycle. Almost all materials are deposited by sputtering with the exception of some polymers and complex structures. In the case of sputtering of alloy target one must keep in mind that different elements have different sputtering yield for a given ion with a certain kinetic energy which results in preferential removal of the element with the higher sputter yield. The angular distribution of the sputtered elements and the position of the substrate too have influence on the composition of the deposited film.

The conventional sputtering process described above has some limitations due to less deposition rates and higher working pressure. In conventional sputtering electrons are soon lost due to recombination at the walls [63]<sup>6</sup>. These limitations are overcome by magnetron sputtering method, presently the most commercially popular technique. In magnetron sputter source presence of magnetic field leads to trapping of electrons near the surface thus enhancing the ionizing efficiency. Electrons follow helical motion around the magnetic field lines and they will travel a much longer path-length in the plasma than in conventional glow discharges, increasing the ionization collisions and consequently the ion fluxes. Purpose of using a magnetic field is to make more efficient

<sup>6</sup> page no. 260

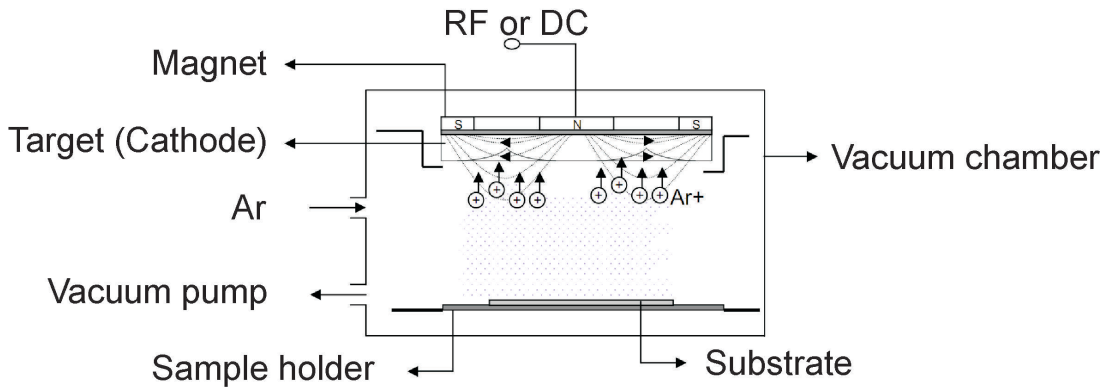


Figure 3.5: Schematic of magnetron sputtering

use of electrons and cause them to produce more ionization [63]<sup>7</sup>. The magnetic field can be supplied by using permanent magnets, electromagnets or by combination of both [65]. Many configurations of magnetic field and cathode shape have been developed such as planar, cylindrical and circular magnetron sputtering. In planar magnetron sputtering sources the magnetic field lines first emanate normal to the target, then bend with a component parallel to the target surface and finally complete the magnetic loop (figure 3.5).

### Sputtering of ferromagnetic material

When the sputtering target is ferromagnetic material the influence of the target on the field distribution of the magnetron must be considered. Depending on the permeability and thickness of the target, it will weaken the intensity of magnetic field exerted by the permanent magnets of the magnetron system (figure 3.6). This causes difficulty in sustaining the plasma and the effect only intensifies as the thickness of the target increases for a given configuration of the magnetron. To avoid this effect either strong permanent magnets must be used that means the size of the magnetron must be enhanced. Other possibility is to make the target thin enough to sustain constant plasma. The available magnetrons during this work were small and limited to use of target 50 mm in diameter. Therefore the maximum allowed thickness of the target (FeCo) was  $\approx 0.6$  mm. That means to produce thicker films the sputtering process

<sup>7</sup>page no. 260

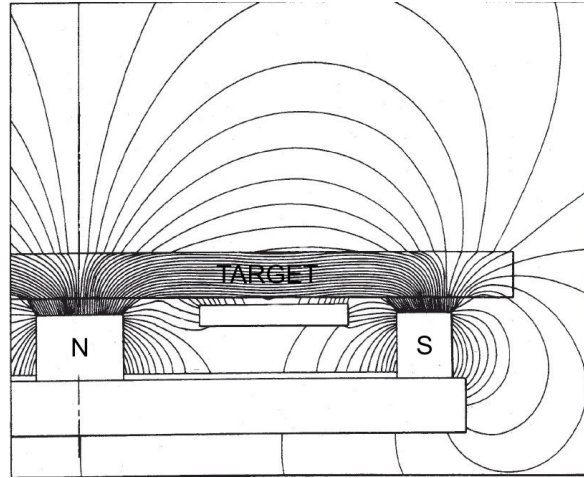


Figure 3.6: Schematic drawing of weakening of field due to ferromagnetic target [12]<sup>9</sup>

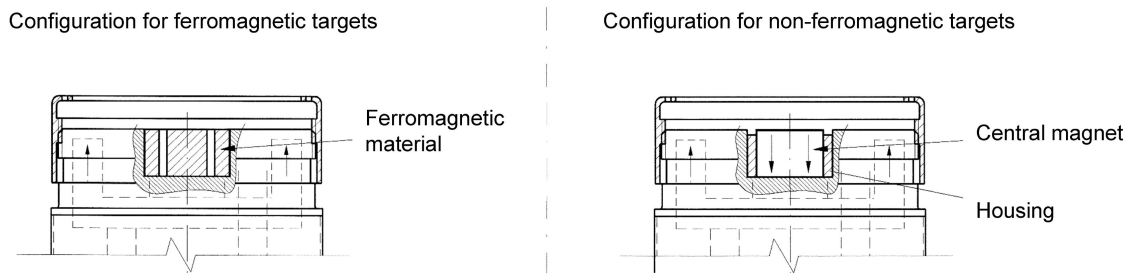


Figure 3.7: Arrangement of permanent magnets in magnetron for sputtering ferromagnetic materials (left) and non-ferromagnetic materials (right).

must be interrupted to allow the change of target. To circumvent this problem the availability of an alternate design of magnetron from Thin Film Consulting Company<sup>8</sup> was advantageous, in which the center magnet is replaced by a ferromagnetic material (figure 3.7). Here the magnet array uses the ferromagnetic target itself to direct and conduct the magnet flux deriving from the ring magnet. The magnetic energy of the ring magnet is so high to saturate the target and establish a magnetic field to confine the plasma in such a manner, that typical sputtering parameters like pressure and voltage are maintained at a level of non-magnetic targets sputtering. With this arrangement it was possible to sputter 2 mm thick FeCo target which lasted until deposition of film 3.5 microns in thickness.

<sup>8</sup><http://www.thfc.de/>

Nanocomposites were fabricated in an already existing sputtering system (in house design). The general structure of the system is shown in figure 3.8. It consist of a cylindrical stainless steel single vacuum chamber with flanges of different sizes (DN63CF) located at appropriate places as per the design. It does not have load lock facility meaning, the sample transfer is done manually through hinged main door located on the front side of the cylinder. The sample holder can work in two modes, stationary and rotation depending on the need. The chamber was evacuated by a turbomolecular (Pfeiffer TMU-260 or TMU-261) and a rotary vane pump (Pfeiffer Duo 5) capable of reaching base pressure of  $1 \times 10^{-7}$  mbar. In depth details of sputter system design and construction are described in previous work [11, 66, 12].

Ferromagnetic materials were sputtered by DC magnetron and  $\text{TiO}_2/\text{SiO}_2$  by RF magnetron sputter sources respectively (ION'X-2 "UHV 9109 - Thin Film Consulting). Argon was used as process gas and the flow was controlled by a gas dosing system (Pfeiffer Vacuum RVC 300).

#### **Chamber conditions**

The chamber was often used for deposition of materials other than ferromagnetic materials like PTFE,  $\text{SiO}_2$ ,  $\text{TiO}_2$ , Au, Ag, Cu etc. Over a period of time thick layers of these materials will be deposited on the walls of chamber. The high residual stresses in the magnetic material coated on the walls of chamber probably leads to cracks in the films leading to water absorption and bad vacuum conditions. Especially use of polymer degrades the vacuum conditions. The magnetic properties, mainly saturation magnetization are very sensitive to the chamber environment. In order to keep the walls of chamber free from forming thick films due to sputtering, an inner cylinder fitting exactly into the chamber was used. The cylinder prevented deposition of the material on the walls of the chamber except where opening are provided. After a certain set of deposition cycles the inner cylinder was removed and a new cleaned one was inserted instead of cleaning the whole chamber every time, which is time consuming exercise. Easily removable parts like shutters, sample holder, magnetron caps were cleaned thoroughly by sand blasting. By this arrangement, walls of chamber can be kept free from coating of materials sputtered in the chamber.

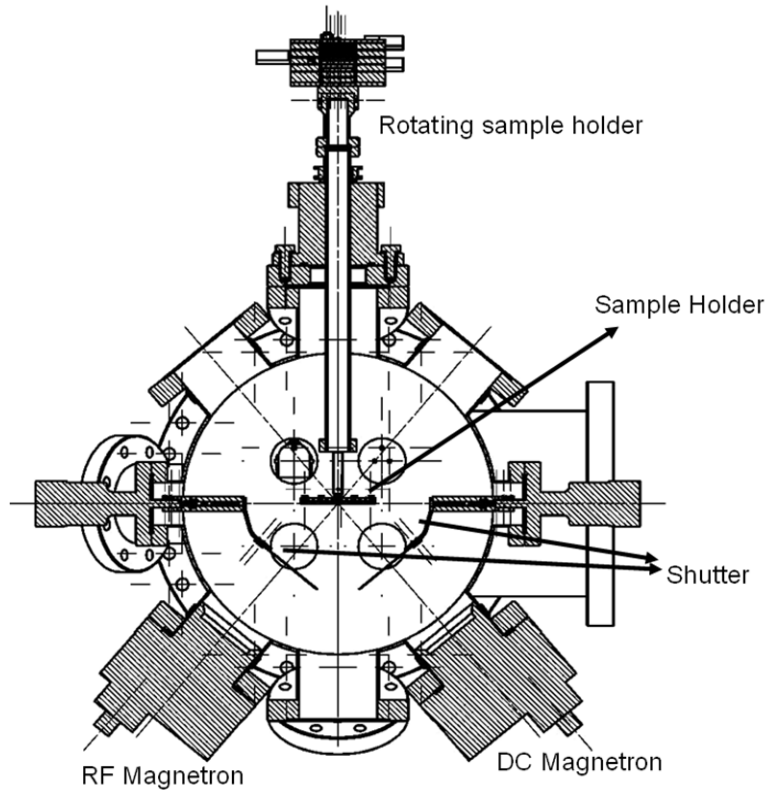


Figure 3.8: Schematic drawing of the vapor deposition system to produce nanocomposites. The chamber is equipped with two magnetrons, quartz crystal microbalance and a rotatable sample holder.

### 3.3 Structural characterization

Electron microscopy is a powerful method to investigate nanoparticle composite materials from the morphological and structural point of view. Metal volume fraction of the nanocomposite was estimated by Energy dispersive X-ray analysis. Transmission electron microscopy was used extensively to investigate the morphology of the nanocomposites.

#### 3.3.1 Energy dispersive X-ray analysis

The energy dispersive X-ray spectroscopy (EDS or EDX) is a widely used non-destructive technique for qualitative and quantitative characterization of the elemental composition of sample. It uses a high energy electron beam to generate X-rays within a sample. These X-rays are characteristics of the constituents of the sample and carry vital information. Electron microscope is designed to detect and measure these characteristic X-rays. The technique is very often used in conjunction with scanning electron microscopy and transmission electron microscopy.

#### Interaction of electrons with solids

Electron bombardment of the sample and its interaction with the matter produce number of effects. The interaction process involves collision of the electron with positively charged nucleus (elastic scattering) and orbital electrons of the atom (inelastic scattering) [67]<sup>10</sup>. In inelastic scattering, energy of the incident electrons is transferred to electrons of the atomic shell and it changes its direction and slows down. Inelastic interactions produce diverse effect including characteristics X-rays which are basis of electron microprobe technique. Due to these numerous different scattering processes, originally sharp focused electron probe spreads over a greater volume after interaction. The zone in which these interactions occur is the interaction volume whose shape and the size depend on the material (atomic number  $z$ ) and the energy and incidence angle of electron beam. The penetration depth of the electrons increases with increasing the acceleration voltage and decreases with increasing the atomic number.

During the electron bombardment of the sample the incident electron ionizes the sample atom by ejecting the inner-shell electron thus creating a vacancy. As a result the atom is at higher energy state and it returns to its ground state when the outer shell electrons fill the vacancy. The energy released in this process leads to emission of either a photon which is 'characteristics' of the element or Auger electron. The process repeats in similar sequence until the atom attains its neutral ground state. The whole series of X-ray emission signals can be sorted based on energy in an energy dispersive

---

<sup>10</sup>page no. 42

X-ray detector. Thus, an X-ray spectrum can be acquired giving information on the elemental composition of the material.

Typically  $K - \alpha$  are used for investigation. Energies of the K and L lines for the material relevant to this work are given in table 3.1. For analysis one must select an acceleration voltage exceeding the absorption energy of the line intended for analysis and in practice as a thumb rule a factor of 2 to 3 is used to efficiently excite the X-ray line with an electron beam.

Element	Z	$K_{\alpha 1}$	$K_{\alpha 2}$
Fe	26	6.40	0.60
Co	27	6.93	0.77
Oxygen	8	0.52	

Table 3.1: Atomic number  $Z$  and the energies of  $K$  and  $L$  lines of selected elements.

In general, the quantitative analysis is performed by comparing the characteristics X-ray intensity from the sample and that measured from the standard. The composition of the standard must be known and the measurement of the sample and standard must be carried out under same device parameters. However, a significant deviation may exist between the measured sample and the standard due to complex alloys, composites etc. The most common correction factors known as ZAF corrections are employed. Here Z refers to atomic number correction which is product of two components, backscattering and electron stopping power (s). The A-factor compensates for the different X-ray absorption. The absorption correction is a function of the take-off angle and Z. A material with higher atomic number absorbs more radiation before it can escape from the sample. The correction for fluorescence (F) is a function of the elements present, their concentrations, mass absorption coefficients and the take-off angle.

For the film thickness investigated in this work, the fluorescence and adsorption contributions play very minor role. The ZAF factor is calculated from the computer interface provided with the device. The metal volume fraction can be determined either by gravimetric method or by EDX analysis and also by thickness calibration.

In the work of Schürmann [11, 16] different techniques to determine the metal volume fraction have been reviewed. The metal filling factor in co-sputtered Ag-PTFE nanocomposite film was calculated by gravimetric method and EDX. It was found that for film thicknesses up to 250 nm there is a good agreement between two methods. For low filling factor the intensities obtained from EDX are associated with errors due to low amount of metal. For the gravimetric method it is important to determine the density of the matrix material (host) and that of metal accurately. Therefore the film thickness and the area must be significantly higher to avoid errors in weight measurement. In this work EDX was primarily used to determine the metal volume fraction of the composite for example FeCo in FeCo-TiO<sub>2</sub> nanocomposite. The X-ray spectra for the sample to be analyzed and the standard of known thickness are obtained under same device parameters. The standard here is the sputtered FeCo metallic film of known thickness. The thickness of the standard must be approximately in the same range as that of the nominal film thickness of metal in the composite films. A large difference in the layer thickness leads to errors due to the different excitation volumes of different elements. The MVF then is calculated by ratio of normalized sample intensity to the normalized standard intensity. The intensity values were normalized to counts of events per second (cps), as it changes with the beam current over a longer measurement.

#### 3.3.2 Transmission electron microscopy

Transmission Electron Microscopy (TEM) is a very powerful tool offering higher resolution down to atomic dimensions. It also gives valuable information about material structure such as grain size, crystal defects etc [67]<sup>11</sup>. In transmission electron microscopy thin specimens (electron transparent) are irradiated with a beam of high-energy electrons. The transmitted electrons through the specimen form an image which is magnified by several electron-optical lenses subsequently. This image can be viewed directly on a fluorescent screen or recorded by CCD camera.

---

<sup>11</sup>page no. 170

TEM can be operated either in imaging, diffraction and spectroscopy modes. Electron diffraction pattern essentially depends on the type of specimen. Amorphous substance produce diffuse rings, fine grained polycrystalline specimen produce ring patterns and thin single crystalline substance produce spot patterns [68]. Thus diffraction patterns provide vital information about the crystal system and the type of lattice of a material. There are different imaging modes in the TEM experiment depending on which part of the transmitted electrons used to form images. In bright field mode only unscattered electrons and electrons scattered up to a small objective aperture angle  $\theta_o$  are used.

Morphology and chemical analysis of FeCo-TiO<sub>2</sub> was carried at Synthesis and Real Structure group held by L. Kienle. Instrument type and the parameters are, HRTEM with a Tecnai F30 G<sup>2</sup> ST (FEG, 300 kV, spherical aberration  $C_s = 1.2$  mm) and a Philips CM 30 ST microscope (LaB6 cathode, 300 kV,  $C_s = 1.15$  mm). All images were recorded with Gatan Multiscan CCD cameras and evaluated with the programs Digital Micrograph 3.6.1 (Gatan) or Crisp (Calidris). Selected area electron diffraction (SAED) was carried out using a diaphragm which limited the diffraction to a circular area of 250 nm in diameter. Chemical analysis by an energy dispersive X-ray spectrometer (EDX) was performed in the nanoprobe mode and by spectral imaging (scanning mode) with a Si/Li detector (Noran, Vantage System). Heating experiments were performed *in-situ* within the Tecnai F30 G<sup>2</sup> by using a double-tilt Tantalum heating stage holder (Gatan)<sup>12</sup> in which sample can be heated up to 1000 °C.

## 3.4 Magnetic measurements

### 3.4.1 Vibrating sample magnetometer

One of the fundamental magnetic properties of a magnetic material is its magnetization behavior under the external magnetic field. Vibrating Sample Magnetometer (VSM) credited to S. Foner [69], is widely used instrument for characterizing the magnetic material. The operating principle is based on Faraday's law which states that an

---

<sup>12</sup>[http://www.gatan.com/holders/652\\_double\\_tilt\\_heat.php](http://www.gatan.com/holders/652_double_tilt_heat.php)

electromagnetic force is generated in a coil when there is a change in the flux linking the coil. The schematic of the instrument is shown in figure 3.9. The magnetization of the sample is achieved by pair of electromagnets which produce homogeneous magnetic field along the X-axis. Fixed pick up coils are mounted on the pole pieces of electromagnets and the sample mounted on sample holder is positioned centrally in the pick up coil. The other end of the rod is fixed to an oscillator which produces sinusoidal vibration giving a vertical motion to the sample (Z-axis).

The mechanical vibration of the sample gives rise to change in the magnetic moment of the sample which induces a voltage in the pickup coils. The magnitude of the voltage measured across the pickup coils is proportional to magnetic moment of the sample and the sensitivity of the pickup coils. It is also proportional to amplitude of vibration and frequency of vibration. The later can be separated by lock-in techniques by providing a reference signal at the vibrating frequency of the vibrating unit. The voltage generated is amplified by a lock-in amplifier which is sensitive to only the signals at the vibrating frequency.

In this work, a VSM 7300 from Lakeshore Cryotronics, Inc., Westerville, USA, was used. The instrument is capable of applying field up to 2 T and sensitive enough to measure the magnetic moment down to  $\mu emu$ . It is also possible to measure the magnetization in different directions by precise turning of the rotating and vibrating head. Before each measurement it is necessary to calibrate the instrument, which is done by a Ni-standard spherical in shape supplied by the instrument manufacturer. The magnetization of the sample is calculated through the magnetic volume of the sample. The plausible errors in the measurement of magnetization curve of the sample arise from the different geometry of the sample compared to that of the Ni-standards, and also from the volume determination necessary for the calculation of the magnetization. Thus the error is in the range of about 5% [70]<sup>13</sup>.

---

<sup>13</sup>page no. 32

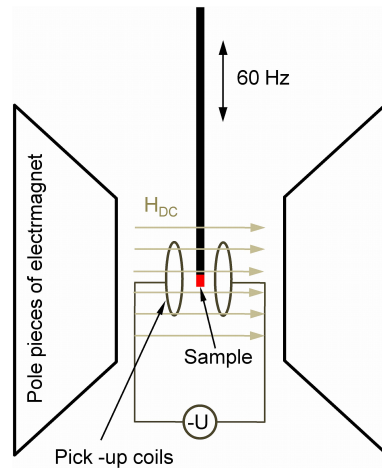


Figure 3.9: Schematic representation of the VSM set up. Sample attached to the sample holder oscillates in the presence of the static magnetic field. This movement of the sample creates an alternating voltage in the pick-up coils which is proportional to the magnetic moment of the sample

### 3.4.2 Magnetoresistance measurement

In this work the magnetoresistance measurements were carried out by two point measurement system at room temperature. The schematic of which is shown in figure 3.10. It consists of pair of electromagnets, mechanical manipulators attached to which are gold pins to contact the sample and a Keithely 2400 with built in power source. All these devices are interfaced through a computer program which provides control over the measurement parameters. The sample is placed in a homogeneous magnetic field generated by a pair of electromagnets. Magnetic field is swept from maximum to minimum value while measuring the current (at constant voltage).

### 3.4.3 High frequency permeability measurement

High frequency characteristics for the nanocomposite and multilayer system were carried out at Microwave group held by R. Knöchel at Institute of Electrical and Information Engineering. The detailed experimental procedure and measurement technique itself has been described at [71, 72, 73], only a brief description will be given here.

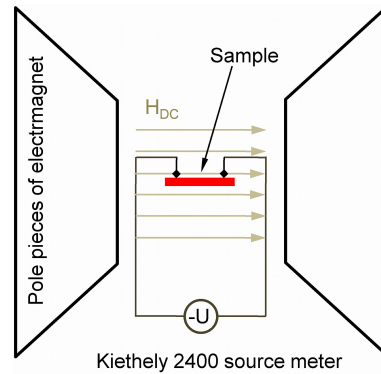


Figure 3.10: Schematic representation of the TMR measurement set up. The sample is placed in a homogeneous static magnetic field with current applied parallel to the magnetic field.

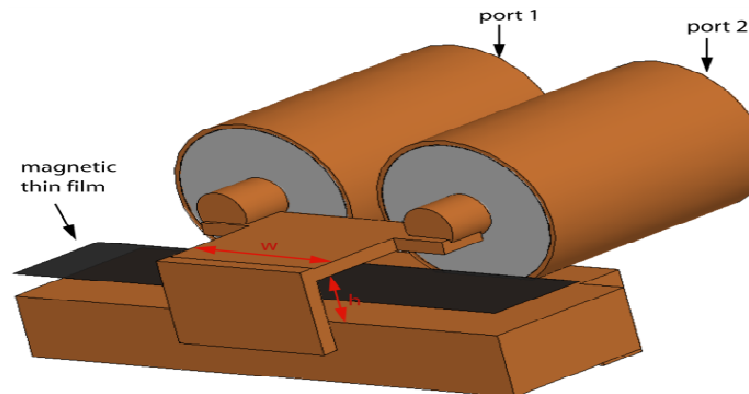


Figure 3.11: Schematic drawing of the high-frequency permeameter [71]

The permeability of magnetic thin films can be determined either by using it as core of suitable high frequency transformer [74] or coil [75]. Here, the magnetic permeability can be determined indirectly by the frequency-dependent transformer parameters or changing the impedance of the inductor with and without sample. Figure 3.11 shows the schematic drawing of the permeameter. It consists of a short circuited strip transmission line, which acts as an inductor. The magnetic thin film is inserted between the strip conductor and the ground. The set up works in a T-configuration similar to that described in [76] and allows transmission measurements. Permeability values are calculated from the measurement of transmission parameter  $S_{21}(f)$ .

$$z = j\omega L \quad (3.1)$$

With  $Z_0$  being the characteristic impedance of the connecting transmission lines,  $S_{21}$  is calculated as

$$S_{21} = \left[ 1 + \frac{Z_0}{2Z} \right]^{-1} \quad (3.2)$$

If the inductance of the empty fixture is  $L_0$ , the change through insertion of the film is assumed to be proportional to the magnetic susceptibility  $(\mu - 1)$ . Considering a filling factor  $F$ , the inductance  $L$  can be written as

$$L = L_0(1 + F(\mu - 1)) \quad (3.3)$$

For narrow strip conductors, the filling factor can be approximated by the ratio  $F = As/Ae$ , where  $As$  denotes the cross section area of the magnetic sample and  $Ae$  that of the empty fixture. For accuracy reasons  $Ae$  has to be determined in practice with 3.2 and using a sample with known parameters  $\mu$  and  $As$  (at low frequencies). There two ways to obtain the permeability spectrum. One possibility is to measure  $S_{21,e}$  with the empty permeameter ( $F = 0$ ) in order to determine  $L_0$ . Instead, the sample can be placed into the fixture and a strong B-Field (1 Tesla) is applied to saturate the magnetic material ( $\mu = 1$ ). This approach is by far more accurate because positioning errors and influence of the substrate are taken into account. Next step is the determination of  $S_{21,s}$  with the unknown magnetic thin film sample. To calculate  $\mu_r$  the ratio  $R = S_{21,s}/S_{21,e}$  and above equations are used

$$\mu_r = \frac{Z_0(R - 1 + F) - 2jL_0\omega(F - 1)(R - 1)}{F(Z_0 - 2j\omega(R - 1))} \quad (3.4)$$

For thin films using the approximations  $F \ll 1$  and  $R \approx 1$  equation 3.4 is simplified to

$$\mu_r - 1 = \frac{K}{F} \left[ \frac{S_{21,s}}{S_{21,e}} - 1 \right] \quad (3.5)$$

# 4 2D Nanocomposites to Monitor Magnetostriction Through Quantum Tunneling

## 4.1 Concept and fabrication details

Two different mechanisms or material properties can be combined in a way such that each phase adds to the functionality of the hybrid or the composite material, resulting in new sets of devices [77]. This concept of "Product Properties" has found great application, especially in the field of magneto-electric composites [78, 79]. Likewise, magnetostriction and quantum tunneling are two effects that can be combined to read a magnetically induced strain by a simple electrical resistance measurement. The hybrid material presented here consists of a macroscopic Terfenol-D crystal and a functional nanocomposite layer attached to its surface as illustrated schematically in figure 4.1. The functional nanocomposite layer is made of polymer and Au nanoparticles in a regime near to the percolation threshold and embedded just below the polymer surface. In this scenario, the elongation produced in a magnetostrictive element is transferred to assembly of Au nanoparticles by mechanical coupling. This magnetically induced strain leads to changes in interparticle separation in the nanoparticle assembly, giving rise to a change in tunneling current between the metal nanoparticles. Since the tunneling current is exponentially dependent on the interparticle distance, a small change in distance can lead to a large change in tunneling current. The functional layer can be transferred to any substrate easily. The presence of polymer is an added advantage when the substrate is conductive as is the case here. Fabrication procedure

specific to the hybrid system is described in the following section and experimental technique is explained in detail in chapter 3.1.

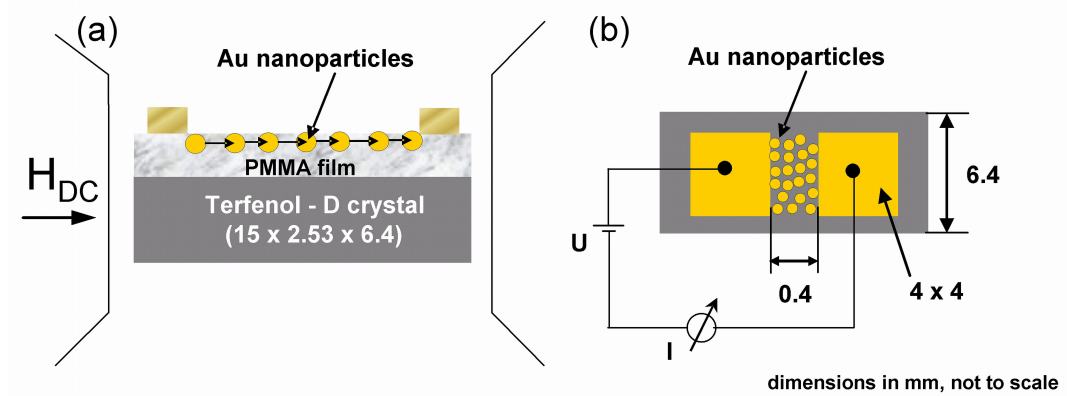


Figure 4.1: (a) Schematic view of the hybrid system and (b) top view showing the geometry of the contact pads.

Steps involved in the sample preparation are shown in figure 4.2. The fabrication process consists of drop coating of polymer solution on to a cleaned Terfenol-D crystal and drying in an air flow controlled set up to achieve maximum homogeneity. Polymer solution was formed by dissolving a known quantity of polymer granules in toluene. Two polymers were selected namely Poly(methyl methacrylate)(PMMA) and Polystyrene (PS).

For the sensor to function, it is essential that the polymer layer provides electrical insulation between the conducting Terfenol-D and the Au nanoparticles. A series of polymer films with different film thicknesses were tested to find the optimum layer homogeneity while providing a good electrical insulation. Polystyrene film could not provide electrical insulation between conducting Terfenol-D and contact pads sputter deposited on to the polymer (figure 4.2). The short cut suggests that there might be pin holes in the PS film through which electrical connection was established. Therefore PS was ruled out as it could not function as electrically insulating layer. It turned out that PMMA is suitable in preventing leakage currents better than PS. A ratio of 105.23 mg PMMA to 7 ml toluene which results in film thickness of few micrometer was used for all samples.

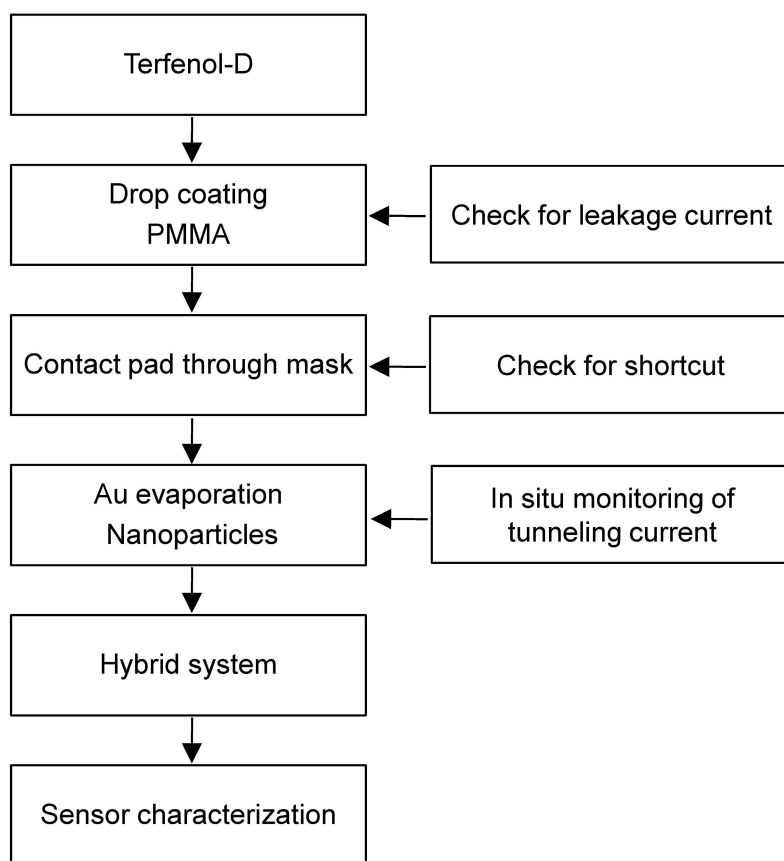


Figure 4.2: Process flow illustrating the steps involved in fabrication of hybrid system.

Next, two electrical Au contact pads with a narrow gap (0.4 mm) were realized by sputter deposition using a shadow mask (figure 4.1). Electrical resistance across the gap was checked to verify insulation by PMMA film. Nanoparticles were formed by thermal evaporation of Au (chapter 2.1). During the evaporation process, evaporation rate and amount of Au were controlled by a quartz crystal microbalance. Sample temperature was controlled by a thermocouple connected to an identical reference sample placed besides real sample. Electrical current across the gap arising due to arriving Au atoms was measured *in-situ* at 1 V. Five samples were prepared with different amounts of Au and hence different tunneling currents as listed in table 4.1. Samples can be classified either with respect to nominal amount of Au deposited or the tunneling current after evaporation. Tunneling current was chosen as it gives the direct interpretation. The change in electrical resistance due to magnetic field were measured in a two point probe setup using a Keithley 2400 source meter in a magnetic field of up to  $\mu_0 H_{ext} = 0.5 T$  (chapter 3.4.2). The tunneling current across the gap

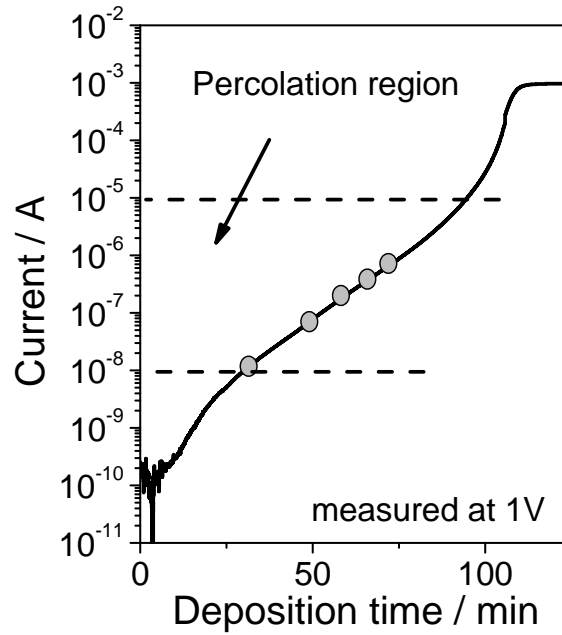


Figure 4.3: Electrical current measured *in-situ* as function of deposition time during evaporation of Au on PMMA. The circles represent approximately the tunneling current obtained for the five samples prepared

is function of the dimensions of the gap, deposition temperature and rate. Therefore prior to the preparation of five samples, percolation curve was generated (figure 4.3) which was used as reference. The result of such measurement from Au deposition on PMMA is shown in figure 4.3. Electrical current measured across the gap increases with deposition time (amount of Au) and finally when Au coverage is close to the film conductivity reaches metallic type. For the sensor, to function the current must be in the transition region, i.e., between pure insulating and metallic region. Therefore the amount of Au deposited on five samples were chosen such that the final room temperature current lies in the transition region. The circles marked on the graph represent approximately regions/final current obtained for the five samples studied in this work.

## 4.2 Sensor characterization

Strain as a function of magnetic field in Terfenol-D crystal is shown in figure 4.4. The maximum strain of 0.07% was obtained at a magnetic field of 0.5 T, which is consistent with other reports [80]. Shape of strain vs field curve fits well with that of data sheets from the company<sup>1</sup>. Magnetostriction of Terfenol-D crystal was measured by optical means. A home-made sample holder (figure 4.4) was used to position the sample in the center of Bruker electromagnet system. Due to space limitations, elongation of the crystal was translated into an orthogonal displacement of L-shaped lever with a mirror attached to it. Direct contact between lever and the crystal was ensured by a small preload ( $<0.5\text{ N}$ ) that was applied via mechanical spring. Movement of the lever was detected by laser triangulation and the elongation of the crystal was calculated by basic geometry.

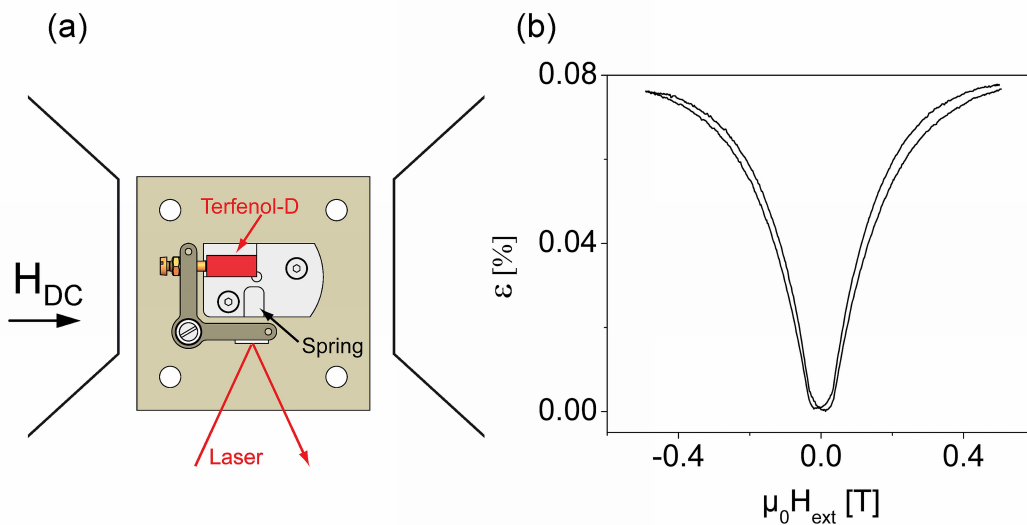


Figure 4.4: (a) Schematic of strain measurement setup (b) Magnetic field induced strain for Terfenol-D crystal

<sup>1</sup><http://www.etrema-usa.com/products/terfenol/>

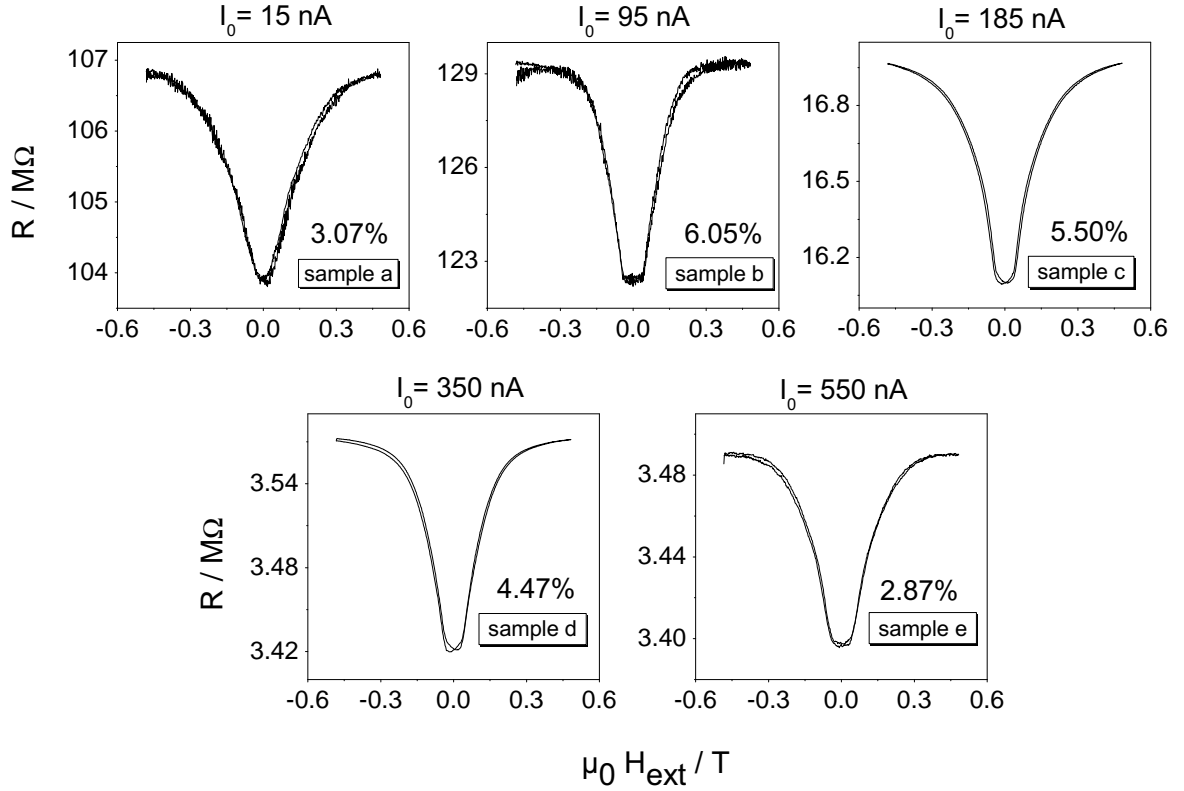


Figure 4.5: Electrical resistance as a function of applied magnetic field measured across the gap at 1 V for different initial tunnel current  $I_0$

#### 4.2.1 Dependence of sensitivity of sensor on gold layer coverage

Change in resistance through the Au nanoparticles as a function of applied magnetic field under equal loading conditions is shown in figure 4.5.

The resistance curve reveals an almost identical shape compared to the strain curve indicating transfer of strain without any hindrance by the polymer layer. Analogous to tunnel magnetoresistance the change in resistance was calculated by

$$QMR = \frac{R_H - R_0}{R_0} \quad (4.1)$$

where  $R_H$  and  $R_0$  are resistance measured under applied magnetic field and zero magnetic field respectively. Here QMR stands for "Quasi-Magneto-Resistance" to

Sample ID	$I_0$ (nA)	QMR (%)
a	15	3.07
b	95	6.07
c	185	5.50
d	350	4.47
e	550	2.87

Table 4.1: Comparison between QMR and tunnel current directly after evaporation ( $I_0$ ).

recognize the fact that the resistance change is not magnetoresistance effect but due to a combined effect of magnetostriction and quantum tunneling. A maximum change of 6.07% was observed among set of five samples prepared. The sensor characteristics diminish for samples having tunneling current higher and lower than sample c as seen in table 4.1. Higher effect can be achieved for a certain constant bias field which will shift the point of origin of the QMR curve to higher slope.

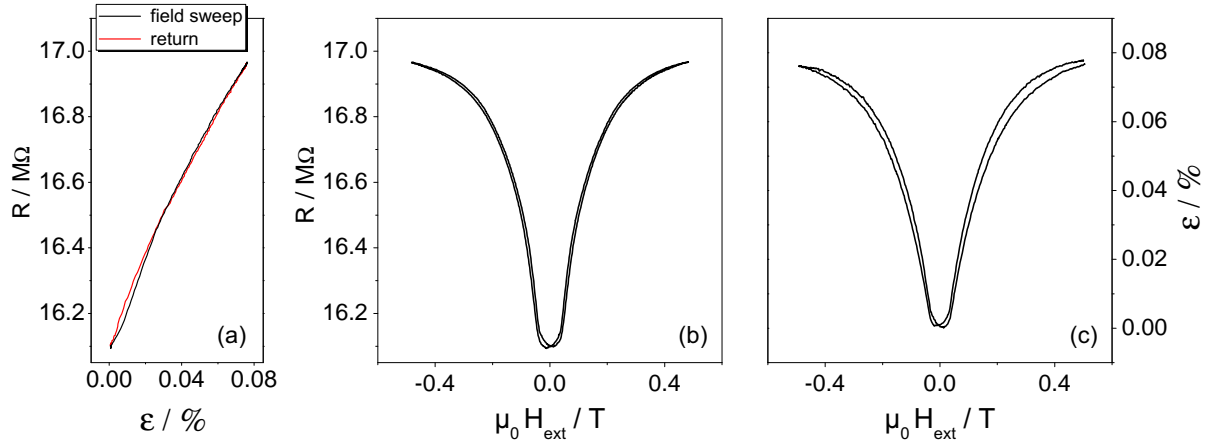


Figure 4.6: a) Resistance as function of magnetically induced strain for sample c, extracted from (b) QMR curve and (c) strain measurement curve.

Resistance as function of magnetically induced strain for sample c is shown in figure 4.6 a which is extracted from the strain measurement data and the QMR data. In limit to small strain, the change in resistance is directly proportional to strain. However, as seen in figure 4.6, there is a small deviation around 0.04% strain. The deviation might come from measurement of strain of the magnetostrictive crystal. However, this

deviation does not seem to have any considerable influence on the performance of the sensor and can be addressed systematically during future work.

Another important factor to characterize the strain sensors is gauge factor (GF) defined by relative change in the resistance divided by strain. Resistance as function of magnetically induced strain is shown in figure 4.6 for sample c. In the limit of small strain  $\Delta R/R = g\epsilon$  where  $g$  can be regarded as gauge factor. Sample c has gauge factor of about 80. This value ranges between those of commercially available metallic strain gauges (GF 2-4) and piezoresistive semiconductor strain gauges (GF 40-140) but it is much smaller than those achieved by sensors based on magnetic tunnel junctions (GF > 800) [81]. In comparison to strain gauges based on tunneling in nanoparticles assemblies [82, 83] whose gauge factor is in the range of 100, the present technique has advantage that, functionalization of nanoparticles is not required and most importantly the tunneling current can be monitored *in-situ* thus increasing the probability of reproducing the exact effect.

### 4.2.2 Repeatability

It is also important that the mechanism should be capable of sustaining repeated usage. Prepared sensors were subjected to multiple runs (each run comprised of two elongation and two contraction cycles) as shown figure 4.7. The difference in resistance measured at zero, +Ve and -Ve maximum fields were compared for each run to estimate the deviation  $\Delta R$ . These values for sample c are listed in table 4.2. Maximum  $\Delta R$  is less than 1% for all samples. For sample c, the maximum difference between each run at respective fields  $\Delta R$  is negligible and the variance of QMR over three runs is 0.24% thus showing better characteristics than the other four. These factors indicate the robustness of the device.

Measurand	1 <sup>st</sup> run	2 <sup>nd</sup> run	3 <sup>rd</sup> run	max $\Delta$
R at min B (M $\Omega$ )	16.960	16.959	16.953	0.03%
R at zero B (M $\Omega$ )	16.099	16.100	16.100	0.01%
R at max B (M $\Omega$ )	16.966	16.968	16.962	0.04%
QMR	5.501	5.501	5.488	0.24%

Table 4.2: Deviations in resistance  $\Delta R$  for sample c over three runs. R-Resistance; B-Magnetic field

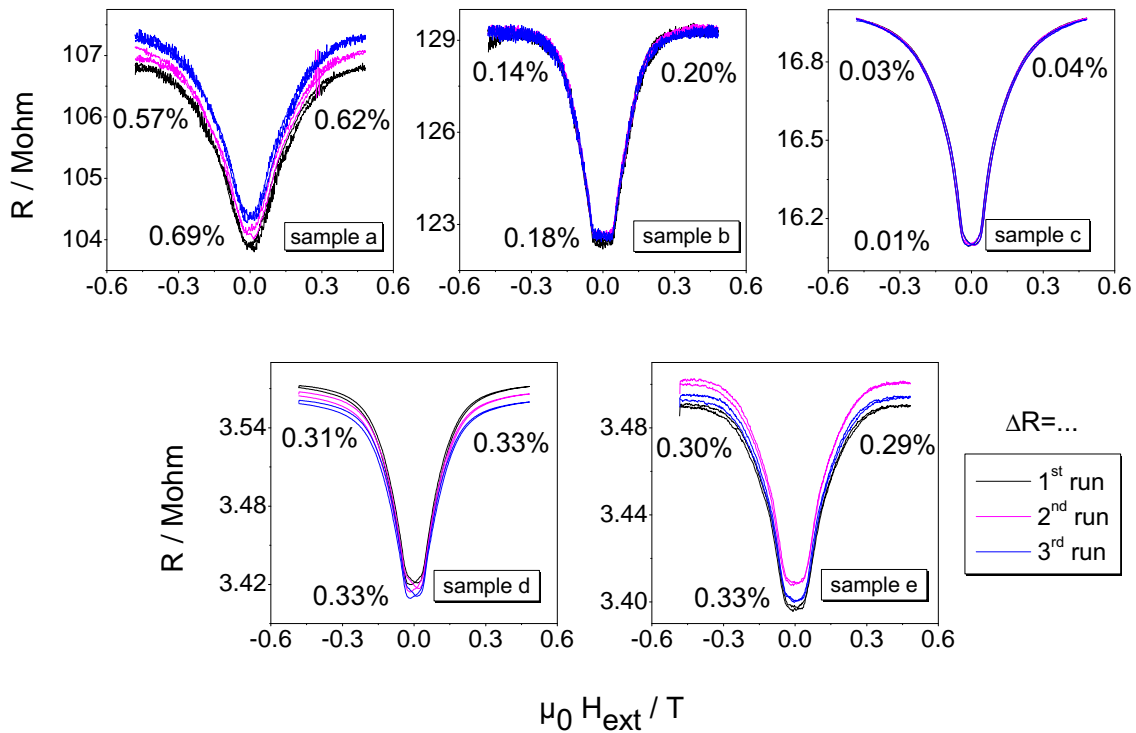


Figure 4.7: Repeatability of the signal trace.  $\Delta R$  indicates the maximum difference of resistance between each run at respective field.

### 4.2.3 Aging and preventive measures

Sensors have to work stable over a long period of time for effective usage in applications. Over a period of time aging processes adversely affect the stability of sensors and hence were also studied in detail. Among the set of five samples, c and d were selected for study. They were stored in ambient conditions and readings were taken over a period

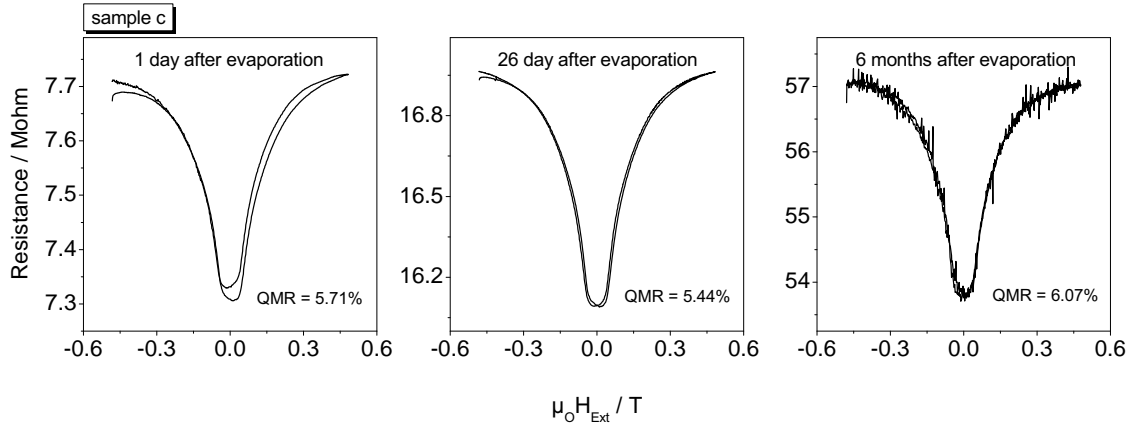


Figure 4.8: Effect of aging phenomena on the QMR behavior for sample c. The sample was stored in ambient condition for six months.

of six months. In figure 4.8 the effect of aging on the sample resistance and QMR for sample c is shown. The tunneling resistance has already increased from 5.4  $M\Omega$  to 7.3  $M\Omega$  in 24 hours and over the next 25 days it is twice as much as it was on day one of QMR measurement. Remarkably the QMR stayed in the same region with bit of degradation and overall symmetry of the QMR curve has improved. The question however is, whether this phenomena of change in tunneling resistance saturates at certain point in time and if the QMR is still measurable. After six months, when the QMR was remeasured it was clear that the tunneling resistance has increased considerably up to 54  $M\Omega$  answering our question. In fact, the resistance has increased to an extent that the signal is noisy and can no longer be measured at 1 V and in contrast, the QMR has remained nearly constant with negligible degradation.

In order to prevent significant aging behavior the cause has to be identified. The mobility of the nanoparticles in the polymer matrix could be one of the reasons otherwise one should not see such a change in the tunneling resistance over the time. One of the ways to inhibit this is to embed the Au nanoparticles into the underlying polymer layer. This process has been employed for stabilization of such metal/polymer system in different applications [84, 85].

The embedding process typically involves a heating cycle up to the glass transition temperature of the polymer matrix. Both current and temperature were recorded throughout the process as shown in figure 4.9. One can identify two distinct regions: a) an increasing current as temperature increases b) a decreasing current due to embedding of the nanoparticles. The nanoparticles below the polymer have lower Gibbs energy than those at the surface hence the reduction of high surface energy of the nanoparticles is the driving force for the embedding process [86]. As the temperature rises current increases at first, which is due to an increase in thermally activated hopping process between the nanoparticles. This process continues until the polymer reaches its surface glass transition temperature, in this case 75 °C marked by softening of the polymer near the surface and decrease in the current. Metal nanoparticles begin to embed into the polymer matrix [87] and thereby increasing the distance between the nanoparticles. Therefore a drop in the conductance is seen. After embedding, the nanoparticles below the polymer surface reach a metastable state at room temperature slowing down the movement further. Glass transition temperature  $T_g$  of pure PMMA is 105 °C [88]<sup>2</sup>, however in the present case the embedding process starts at temperatures below 105 °C as seen in resistance versus temperature measurements (figure 4.9). This difference can be explained by the importance of surface glass transition temperature for the embedding process which is lower than the bulk transition temperature [85].

In order to understand the effects of embedding combined with aging, the QMR was measured directly before and after embedding process and in addition after six months which are shown in figure 4.10. Initial resistance increased from 4  $M\Omega$  to 10  $M\Omega$ , however, the most important point to note is that the shape of hysteresis is preserved, indicating that the combined mechanism of the sensor is not affected by embedding process. Furthermore, the QMR also did not change significantly and the mirror symmetry around zero magnetic field of the measurement signal has also improved. Embedded sample was stored under the same conditions as that of previously mentioned sample c for six months. As shown in figure 4.10 b) and c), the change in the resistance is much smaller (2  $M\Omega$  compared to 38  $M\Omega$  of non embedded sample c) and remarkably the QMR amplitude did not change significantly.

---

<sup>2</sup>page no. 203

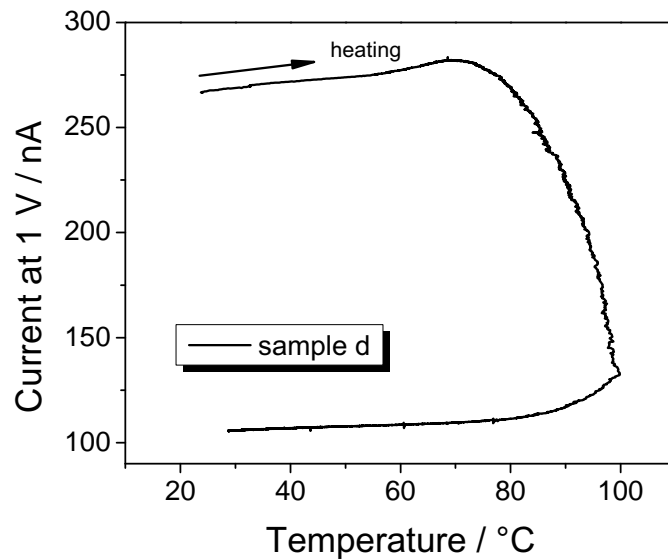


Figure 4.9: Changes in electrical resistance during embedding process.

### 4.3 Model to use metal/polymer composite in cantilever-type actuators

The quasi two dimensional metal/polymer system is not just restricted to Terfenol-D crystal, it could be transferred to any substrate. The functional layer can be downscaled to sub-micrometer dimensions where other strain measurement techniques become more and more complex and costly. Therefore, its application in magneto-electro-mechanical systems (MEMS) is highly promising, for instance in combination with cantilever-type actuators [89]. The coating of these actuators with the functional layer as presented here offers an easy and cheap way to monitor their bending behavior. This is also a promising concept, e.g., for atomic force microscopy (AFM) tips [90], where the electrical read out of the functional layer can be easily used for the surveillance of the mechanical behavior of the AFM tip. It has to be kept in mind that the average strain on the surface of the cantilever has to be in the range required by the 2-d functional layer.

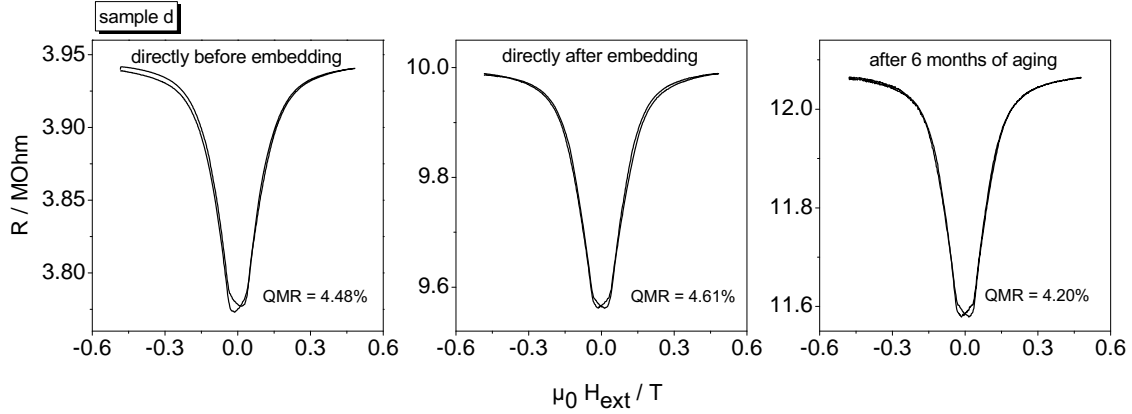


Figure 4.10: Aging and embedding phenomena for sample d. (a) QMR before embedding (b) QMR directly after embedding. The resistance has increased 3 times while change in the QMR is negligible. (c) Effect of aging. Unlike sample c, which did not undergo the embedding process, the change in the absolute value of the resistance is small ( $2 M\Omega$ ), while the QMR amplitude remained almost constant at above 4%.

In order to ascertain that the functional layer can be adapted to cantilever-type actuators, simple bending beam experiments were performed. A polyimide foil of dimension  $14 \text{ mm} \times 3.3 \text{ mm} \times 0.125 \text{ mm}$  was used as substrate. The functional layer was prepared on this foil in a similar way as that on the Terfenol-D crystal. In this case, the gap was located close to the hinge point as here a maximum bending occurs. Prepared sample is then clamped at one point and measured quantity of load was applied on the free end as shown in figure 4.11. The change in resistance due to deflection of the beam is shown in figure 4.12. Principle mechanism is same as earlier, but unlike longitudinal strain, here the strain is due to bending of the beam. Bending due to the load was estimated by beam deflection formula and is tabulated in 4.3.

$$\delta_{max} = \frac{Fl^3}{3EI} \quad \text{where} \quad I = \frac{bh^3}{12} \quad (4.2)$$

where  $\delta_{max}$  being maximum deflection at the free end of the cantilever for the corresponding load  $F$ , ( $b \times h \times l$ ) are dimensions of the beam in m,  $I$  is moment of inertia

2d polymer/metal nanocomposite

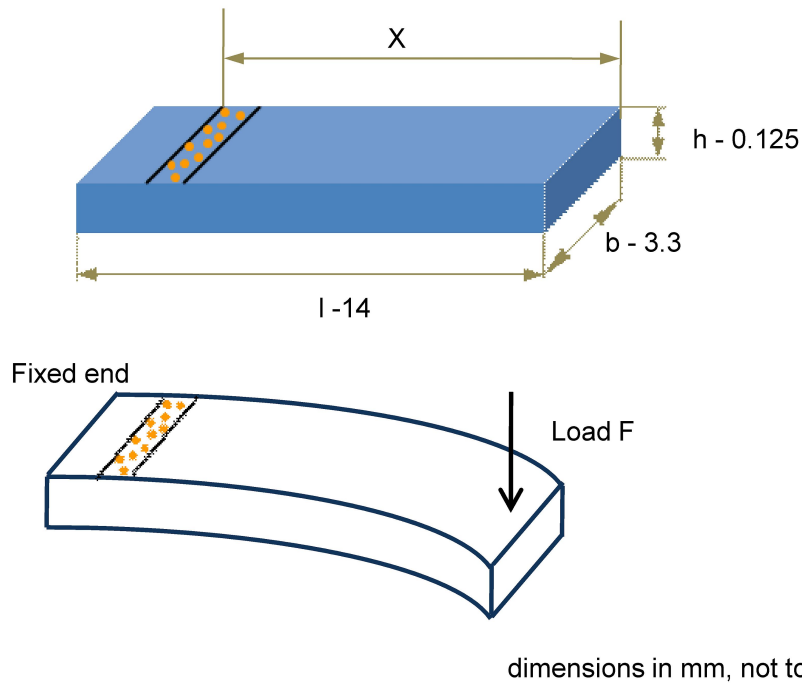


Figure 4.11: Schematic of the cantilever type model for testing the quasi 2d metal/polymer nanocomposite

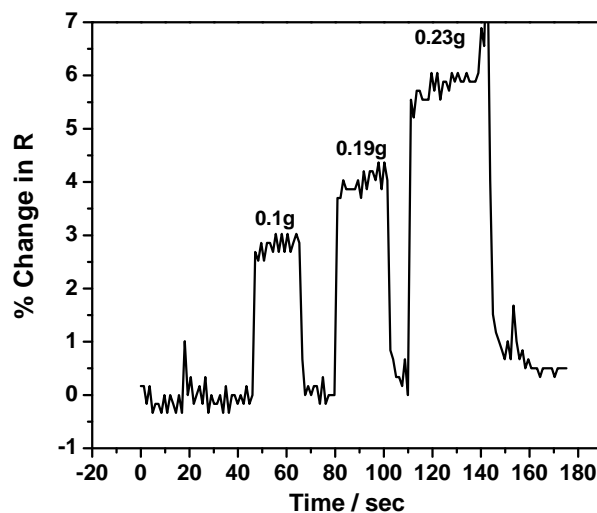


Figure 4.12: Changes in the resistance due bending of cantilever beam with point load at the free end. The spikes seen in the measurement curve originate from small vibrations caused while placing/removing the load manually.

Load (g)	Force (N)	deflection $\delta_{max}$ ( $\mu m$ )	$\Delta R$ (%)	strain (%)
0.11	0.0010	612	3	0.052
0.19	0.0018	1058	4.5	0.09
0.23	0.0022	1280	6	0.11

Table 4.3: Maximum deflection at the free end and the strain in the region where the sensor is placed due to the bending estimated from beam formula.

and  $E$  Young's modulus of the beam material<sup>3</sup>. The strain on the surface of the beam at any section  $X$  is given by

$$\epsilon(X) = \frac{6M(X)}{Ebh^2} \quad \text{where} \quad M(X) = F.X \quad (4.3)$$

The model experiment demonstrates that the metal/polymer functional layer can be used in cantilever as well.

---

<sup>3</sup> E=3GPa for Polyimide (kapton) foil, source Goodfellow GmbH



## 5 3D Nanocomposites Exhibiting Tunnel Magnetoresistance

In the previous chapter polymer based nanocomposite was discussed in detail with respect to its preparation and application as strain sensors. It has some limitations due to its dimensionality because of which it can not be applied universally. In 3D nanocomposite, metal nanoparticles are dispersed uniformly in an insulating matrix which can be made into films of micrometer thickness preserving the metal to insulator ratio. In this chapter, nanocomposites consisting of  $\text{Fe}_{50}\text{Co}_{50}$  (hence forth FeCo) as ferromagnetic component in a ceramic matrix will be presented. In comparison to the previous hybrid material here Au is replaced by FeCo and polymer by  $\text{TiO}_2$ . The need for the ceramic matrix arises because of chemical reactions between magnetic material and the organic matrix during co-sputtering [12]<sup>1</sup>. It is known that, nanoparticles are very reactive due to extremely high surface area to volume ratio. Fluorine and carbon being the main elements in the polymer (Teflon-AF), forming of metal fluorides are very likely during co-deposition (evaporation and sputtering). Presence of Oxygen compounds in Teflon AF as well as the residual gas in the chamber makes it more complicated. Due to which the resulting nanocomposites are no more ferromagnetic in nature thus depriving it of the possible applications. Chemical reaction are not expected to be severe in the case of ceramic matrix assuming that the oxygen is tightly bound to the matrix material, especially for  $\text{TiO}_2$ , and formation of metal fluorides does not exist. Therefore ceramic matrix was opted instead of polymer.

Following chapter deals with the tunnel magnetoresistance in FeCo- $\text{TiO}_2$  system. As discussed in chapter 2, the functional properties of nanocomposite can be tuned depending on the metal volume fraction (MVF). Therefore the characteristics and the

---

<sup>1</sup>page no. 77

functional properties of nanocomposites were characterized in terms of MVF.  $\text{TiO}_2$  was chosen as matrix because so far it was only investigated in multilayer configuration but not in nanocomposites. Since the discovery of tunnel magnetoresistance (TMR) in granular films [91, 92] they have attracted great deal of interest. These composites have applications in spintronics [3] and GHz rf circuits [93]. In relation to the metal volume fraction, they exhibit three electrical regimes; dielectric, transition and metallic with each regime having distinct properties. Composites typically containing 30% to 40% MVF show superparamagnetism and room temperature (RT) tunnel magnetoresistance which arises from tunnelling of spin-polarized electrons [44, 94]. Most of the following results are excerpted from own publication Kulkarni *et al* [95].

### Preparation

Composite films of FeCo- $\text{TiO}_2$  were sputter deposited at RT in an argon atmosphere on a copper coated TEM grid and a specially designed Si/SiO<sub>2</sub> substrate for TMR measurement. As described in chapter 3.2 customized sputtering chamber was used here.

A compositional spread was achieved within one deposition by co-sputtering from two sources. The sources were mounted at 30° with respect to normal and the sample holder was centrally mounted and held stationary. By using this effect, in one sputtering process as many as five samples with distinct MVF were fabricated. The base pressure was lower than  $5 \times 10^{-7}$  mbar, FeCo was sputtered by a DC magnetron source and  $\text{TiO}_2$  by a RF magnetron source. The substrates for TMR were prepared by photolithography with Au/Cr electrodes of 30/5 nm thickness and an interspacing of 25  $\mu\text{m}$  (figure 5.1).

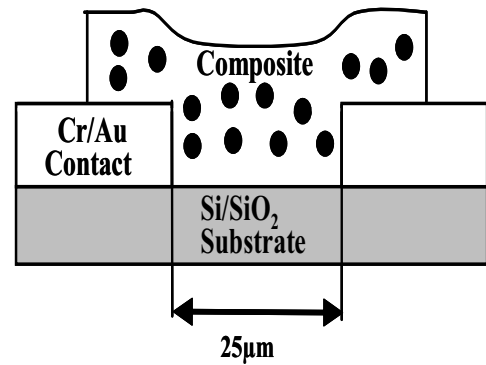


Figure 5.1: The substrate for tunnel magnetoresistance measurement

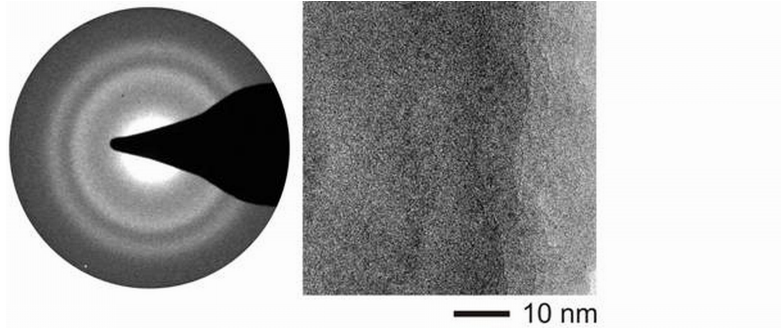


Figure 5.2: SAED pattern (left) and bright-field image (right) of freshly prepared (MVF  $\approx$  25-30 %).

## 5.1 Evolution of morphology with respect to metal volume fraction

TEM analyses were employed extensively to study chemistry and structure of the composite material. The structural ordering of FeCo particles incorporated inside the amorphous  $\text{TiO}_2$  matrix depends on the MVF. Figure 5.2 shows HRTEM image and the corresponding selected area electron diffraction pattern (SAED) for FeCo- $\text{TiO}_2$  nanocomposite with  $\text{MVF} < 35\%$ . HRTEM micrographs (figure 5.2 right) display no structural ordering even at nanoscale thus it can be said that the material does not contain any crystalline component of significant dimension. The FeCo particles are amorphous, cf., the diffracted intensity on a broad concentric circle at  $d = 0.20(1)$  nm as seen in figure 5.2 left. In spite of the well known problems of quantification light elements by EDX, test measurements on distinct oxide materials point to a sufficient reliability of the setup for a semi-quantitative interpretation, even in such critical field. In the case of freshly prepared composite films, the quantification of data gives a ratio O : Ti between 1.8 to 2.5. Hence, the chemical nature of these freshly prepared films correspond to a composite material made of FeCo and  $\text{TiO}_2$ . Finding of amorphous FeCo nanoparticles is very interesting from the fundamental point of view because FeCo is not expected to be a glass forming alloy even at high quenching rates. Amorphous structure seems to be a result of the very small particle size and the resulting interfacial stress which can better be accommodated by an amorphous structure.

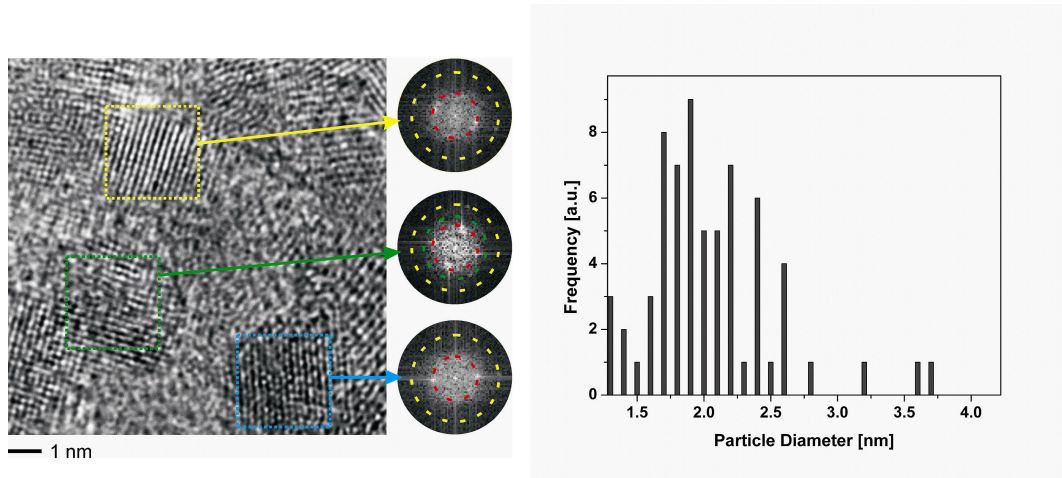


Figure 5.3: (a) HRTEM micrograph of the nanocomposite (38% MVF) with the Fourier transforms from the marked nanoparticles showing the lattice fringes  $d(011) = 0.204(10)$  nm,  $d(002) = 0.141(10)$  nm and b) the particle size distribution from the corresponding sample, not from the figure 5.3 a.

Figure 5.3 shows the HRTEM micrograph recorded on a freshly prepared composite film with  $MVF \approx 38\%$  and the particle size distribution from the corresponding sample respectively. The lattice fringes matched to the structure of FeCo as demonstrated by the accompanying Fourier transforms which were calculated inside the marked areas e.g.  $d(011) = 0.204(10)$  nm,  $d(002) = 0.141(10)$  nm (reference values [96]: 0.203 nm, 0.143 nm). Thus suggesting presence of nanoscale FeCo crystallites at higher MVF.

### 5.1.1 Annealing

Frequently, these nanocomposites are subjected to post preparation processes in order to tailor the properties, e.g., field annealing and the integration into the CMOS process involves heat treatments [97]. Annealing of nanogranular films change the microstructure and magneto transport properties and this is particularly important, e.g., in TMR sensors [98]. Therefore the temperature appears as one of the demanding criterion for the nanocomposites functional properties and structures. In-situ heating in the transmission electron microscope (TEM) is a powerful technique for understand-

ing such temperature effects by real-time observation at high spatial resolution. In order to ascertain the specific changes introduced upon *in-situ* heating, it is important that the films do not change their microstructure during electron beam impact. Fortunately, these films did not show irradiation induced artefacts even after increasing the dose highly by removing the condenser aperture. Considering that the films were amorphous in nature no crystallization was observed thus making it possible to do *in-situ* TEM heating experiments.

Figure 5.4 shows the microstructure changes observed in the initially amorphous film. At a temperature of 450 °C separation of bright field contrast by formation of nanosized crystallites with strong diffraction contrast was observed. These species are embedded inside the amorphous matrix and are frequently faceted, e.g., enlarged section in figure 5.4. 3a. EDX analyses performed on the strongly diffracting crystallites indicate a considerable decrease of the Fe : Co ratio to typical values in the range of 0.05 - 0.1, while in the surrounding matrix only traces of Co can be detected. This finding can be rationalized by assuming Co as the initially formed crystalline phase. The SAED patterns, figure 5.4 b and c, were recorded on single and multiple crystallites, respectively. All d-values agree well with the reference values [99] for cubic high temperature modification of Co. As exemplified by the HRTEM analysis, the initially formed Co crystals contain crystal defects. It is not clear whether such features are interrelated with strain or local changes of the chemical composition, e.g., a partial oxidation of Co. In addition figure 5.4 3d, depicts the STEM-EDX elemental maps which confirm the segregation of Co after the *in-situ* heating. The TMR in heated samples (MVF 25 -30%) vanishes due to a huge increase in the mean particle distance and phase separation of Fe and Co, as obvious from the TEM analysis.

## 5.2 Magnetic properties

Figure 5.5 shows in-plane magnetization curves measured at RT for as deposited FeCo-TiO<sub>2</sub> nanocomposite films. Nanocomposite films with MVF fraction < 50% exhibit superparamagnetism. Superparamagnetic behavior requires well separated magnetic

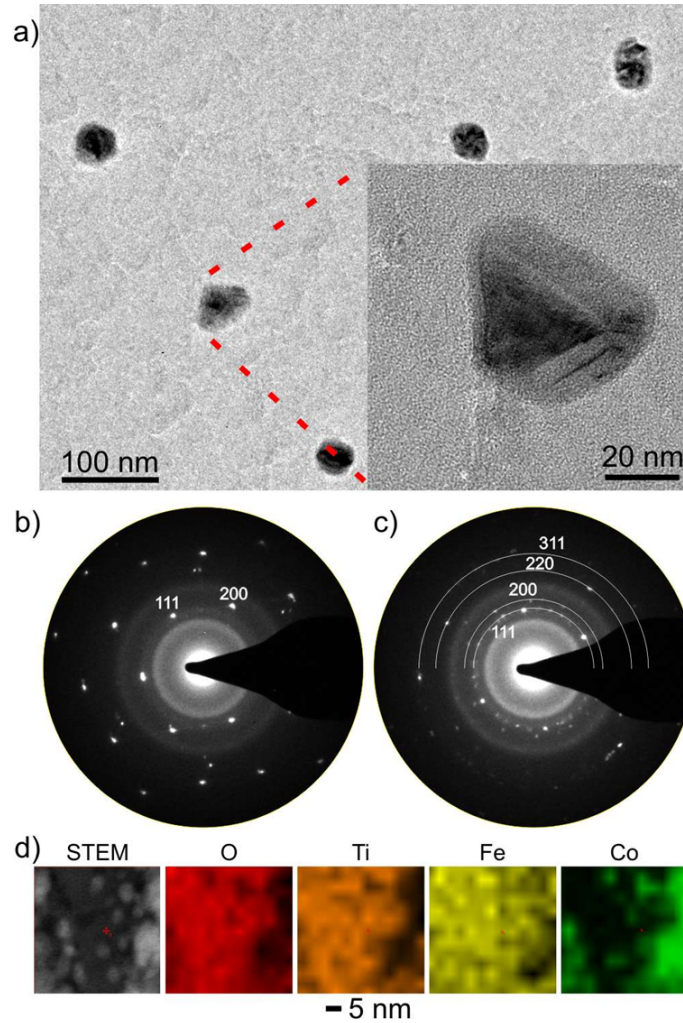


Figure 5.4: (a) Microstructure of the initially amorphous film  $\text{Fe}_{50}\text{Co}_{50}\text{-TiO}_2$  after *in-situ* heating. Inset: enlarged section of a Co nanocrystal; (b) SAED patterns recorded on a single nanocrystal, [110], and (c) on multiple crystals of fcc-cobalt. The d-values of  $d(111) = 0.205(5)$  nm and  $d(200) = 0.178(5)$  nm (b) and  $d(111) = 0.205(5)$  nm;  $d(200) = 0.178(5)$  nm,  $d(220) = 0.126(5)$  nm,  $d(311) = 0.107(5)$  nm (c) convincingly agree with the reference values. (d) STEM image (left) and EDX elemental maps recorded after *in-situ* heating indicate the phase separation of Fe and Co.

particles and particles with average diameter less than the single domain particle size (chapter 2.2). In contrast, the composite films with 53% MVF are ferromagnetic with coercive field of 60 Oe. VSM measurements indicate that with an increase in the MVF, the composite films transit from superparamagnetic to ferromagnetic. The increase in

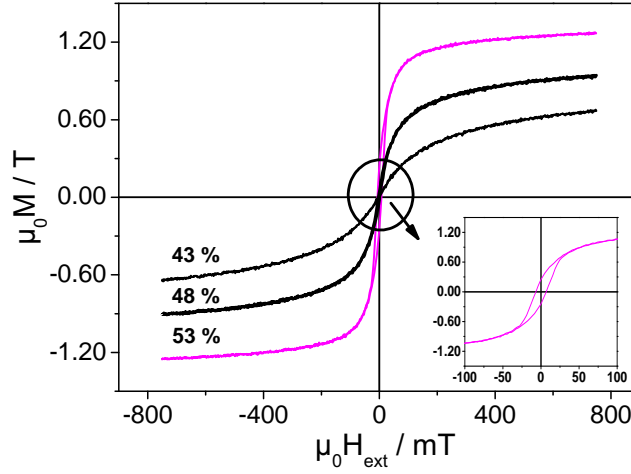


Figure 5.5: In plane magnetization curves of  $\text{Fe}_{50}\text{Co}_{50}\text{-TiO}_2$  measured at RT for various metal volume fractions as indicated. The inset shows the magnified view of hysteresis loop for 53% MVF.

saturation magnetization measured at  $H_{max}$  with increasing MVF could be partially due to incomplete saturation of the superparamagnetic films at RT and due to the formation of a thin oxide shell which has less influence on larger particles. This has also been observed in other granular films [22, 27]. As mentioned earlier, FeCo forms coalesced crystallites in the  $\text{TiO}_2$  matrix at higher filling factors resulting in opening up of the hysteresis loop. Here the magnetization process is governed by domain wall motions whereas magnetization reversal can only occur via rotational processes in the composites containing well separated single domain particles [25].

The critical particle size at which the transition from superparamagnetic to ferromagnetic behavior occurs is an interesting information. Particle size can be qualitatively derived by fitting the experimental magnetization curve with classical Langevin function [100]. It describes the magnetization in superparamagnetic state by

$$\frac{M}{M_o} = L(\alpha) = \coth\left(\frac{\mu H}{k_B T} - \frac{k_B T}{\mu H}\right) \quad (5.1)$$

$$\mu = M_s V = M_s \frac{4\pi}{3} \left(\frac{d}{2}\right)^3 \quad (5.2)$$

where,  $M_o$  is the saturation magnetization of the sample at a given temperature  $T$ ,  $M_s$  saturation magnetization of the bulk phase,  $H$  is the applied field and the particle diameter is given by  $d$ . It is a known fact that, the particle size  $d$  has a certain distribution and the type of size distribution function is linked to the method of preparation [28]. Log normal distribution function [29] fits well for the PVD method. It is defined as

$$P(d) = \frac{1}{\sqrt{2\pi} \ln \sigma} \exp\left(-\frac{(\ln d - \ln d_m)^2}{2 \ln^2 \sigma}\right) \quad (5.3)$$

where,  $d_m$  and  $\sigma$  are statistical median and standard deviation, which describe the probability distribution function  $P(d)$ . Here the measured curves are fitted to the Langevin function by least square approach. Figure 5.6 shows the calculated magnetization as a function of the applied field and the particle size distribution function which gives best fit.

The average particle size and the width of distribution increases, as the metal volume fraction increases. This is also the characteristic of the deposition technique. According to domain theory and experiments [26] on ultra fine particles, for Fe Co maximum coercivity was reached for diameter of 21 nm and 20 nm respectively. The transition to the superparamagnetic regime occurs below these dimensions ( $d < 20$  nm). Estimations of critical size for spherical particles with no shape anisotropy made by Kittel as mentioned in the reference [28] were also in the same range. In the present case, average particle diameter for 48% MVF is 5.3 nm and the distribution function has large tail towards the end. Further increase in the MVF is bound to increase the particle diameter and width. This point marks the commencement of opening up of hysteresis loop and hence, it can be said that the change in the magnetization behavior occurs above diameter 6 nm. It should be noted that as the filling factor increases the clusters come closer and there exists a possibility of coalescence. The particle size distribution obtained from TEM for 38% volume fraction is 2 nm, which is inline with the observation made here. Therefore, one can say that the average particle size for MVF < 38% might be less than 2 nm and some of the metal present could be still in atomic form.

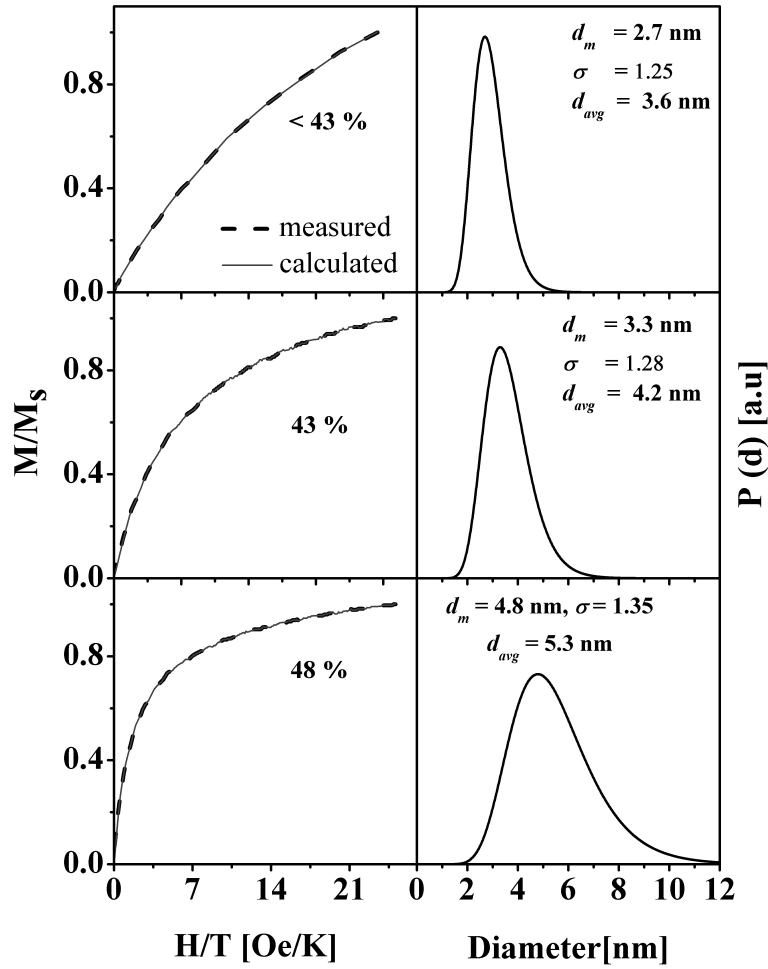


Figure 5.6: Calculated magnetization curves (solid line) from Langevin function and the corresponding particle size distribution estimated by least square method for different MVFs.

### 5.3 Magneto-transport properties

The type of electrical transport mechanism in the composites is closely related to the morphology of the composites. TMR should occur in a region where the electrical conductivity shows tunnel type transport mechanism. This can be verified by measuring the temperature dependence of electrical resistance. Such a measurement is shown in figure 5.7. The temperature coefficient of resistance is negative for 43% and 48%

MVF, suggesting non metallic type conductivity. It shifts to positive values for 53% above 150 K, indicating the onset of metallic behavior due to percolation. For 53% MVF, the resistance reaches to a minimum value at 150 K before climbing up again. For metal-insulator composites, Helamn and Abeles [92] observed that the temperature dependence of resistance should follow an exponential law involving temperature  $T$  and activation energy  $C$  responsible for the process.

$$R(T) = R_0 \exp\left(\sqrt{C/k_B T}\right) \quad (5.4)$$

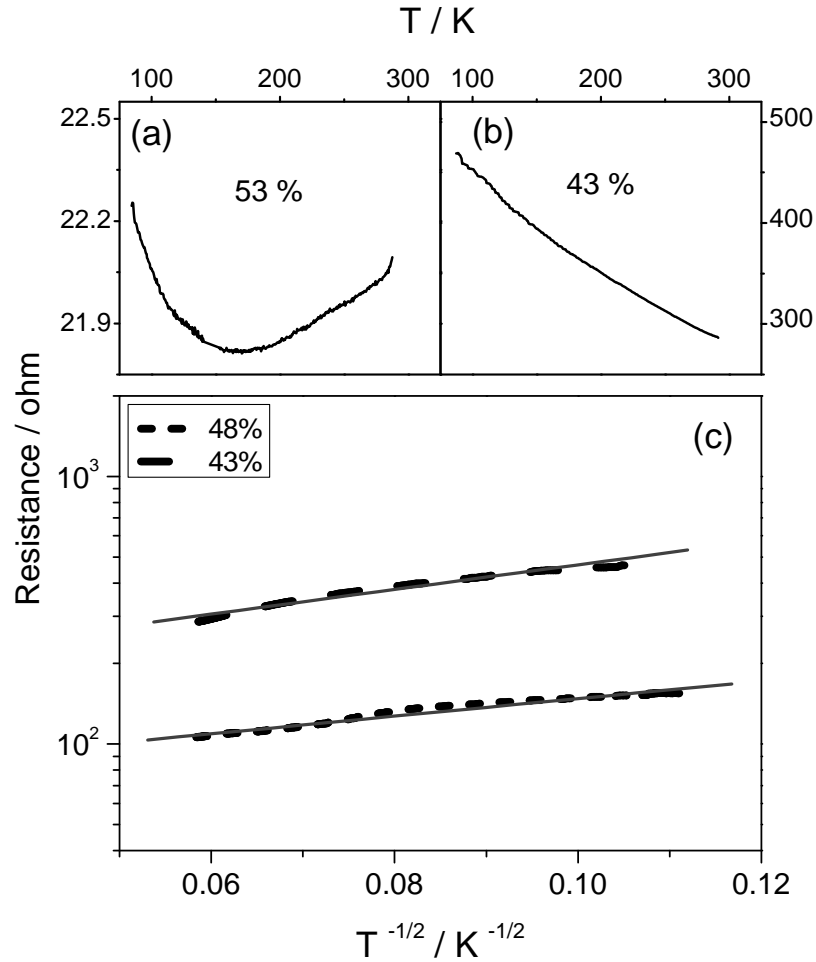


Figure 5.7: Relationship between temperature and electrical resistance for MVF (a) 53%, (b) 43% and (c) plotted in  $\log R - T^{-1/2}$  scale, the solid lines in (c) are approximate fit to  $\log R \exp(C/T)^{-1/2}$ .

As shown in figure 5.7c, a logarithm of  $R$  plot is approximately linear to  $T^{-0.5}$  for 43% and 48% MVF. These measurements correlate well with the fact that the maximum of magnetoresistance corresponds to the sample showing non metallic transport behavior.

The dependency of electrical resistance on the external magnetic field for FeCo-TiO<sub>2</sub> composites with different MVF, measured at RT, is depicted in figure 5.8. The relative change in the resistance is called as magnetoresistance (chapter 2.3).

All the films show a decrease in the resistance upon the application of an external magnetic field. A maximum change of 4% was measured for a composite with 48% MVF within the range of applied field. The TMR was found to be present for amorphous as well as crystalline FeCo particles and higher for the later. As seen in figure 5.8, the TMR amplitude increases with increase in the MVF up to 48% and then decreases. The results for FeCo-TiO<sub>2</sub> reported here possess same course of TMR as a function of FeCo volume fraction, as reported for aforementioned other granular films [98].

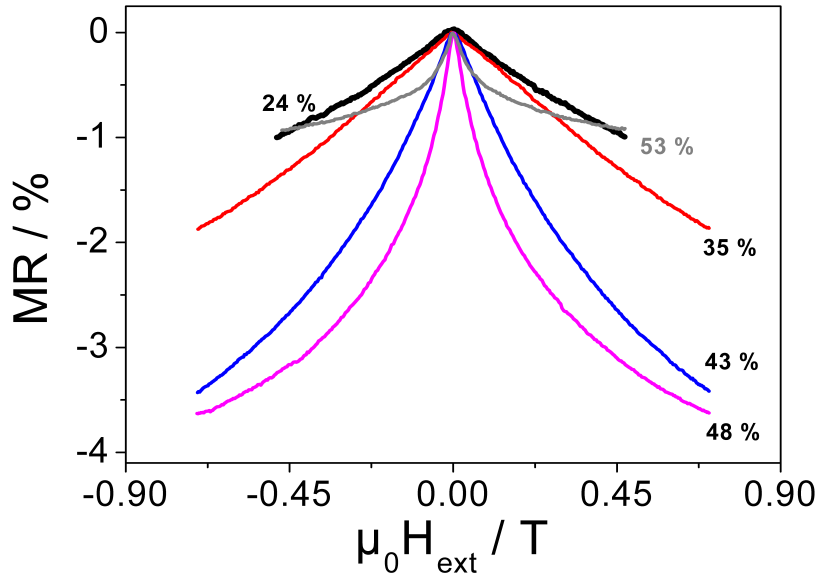


Figure 5.8: Dependence of electrical resistance on the applied magnetic field at RT for Fe<sub>50</sub>Co<sub>50</sub>-TiO<sub>2</sub> composite with different MVF as indicated.

In the beginning FeCo Particles are few and far apart, i.e., the thickness of oxide tunnel is larger than the spin diffusion length giving rise to smaller TMR amplitude. The TMR curves do not show hysteresis and are unsaturated. As the MVF advances the metallic particles tend to grow in size, resulting in decrease of inter-particle separation and as noted earlier crystalline FeCo particles were observed above 35% MVF. The still increasing TMR indicates that the grains are separate and an optimum configuration for spin dependent tunneling occurs at 48% MVF. In this context, it is difficult to determine in which proportion the change in inter-particle separation and the formation of crystalline particles contribute to the increase in TMR. Further increase in the MVF leads to coalescence between neighbouring particles. Coalescences cause formation of clusters of particles with multidomain structure due to magnetic inter particle interaction which is reflected in butterfly shaped TMR hysteresis (figure 5.11 inset). The TMR results along with the magnetic behavior showing the characteristics of magnetic single-domain particles and superparamagnetism demonstrate spin-dependent tunneling between well separated magnetic particles give further evidence of the presence of distinct FeCo particles.

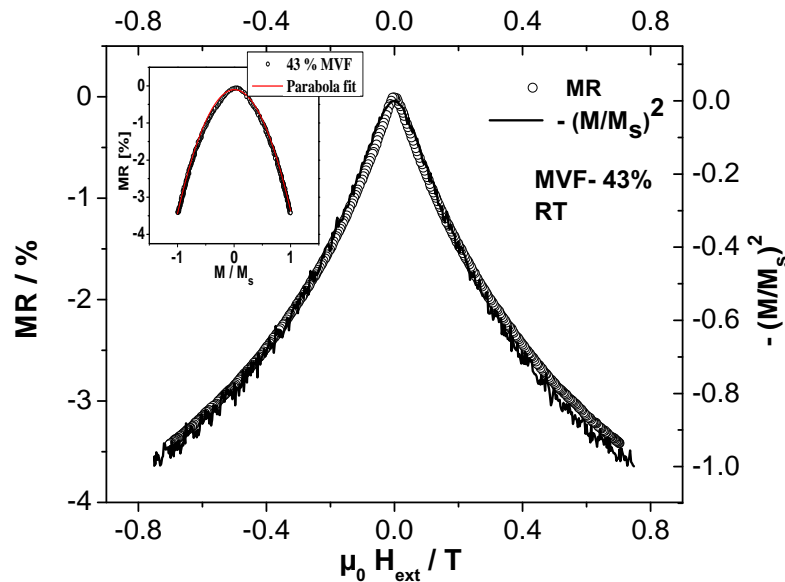


Figure 5.9: TMR as a function of applied magnetic field and square of normalized magnetization  $-(M/M_s)^2$  from VSM measurements at RT for 43%, inset TMR vs magnetization

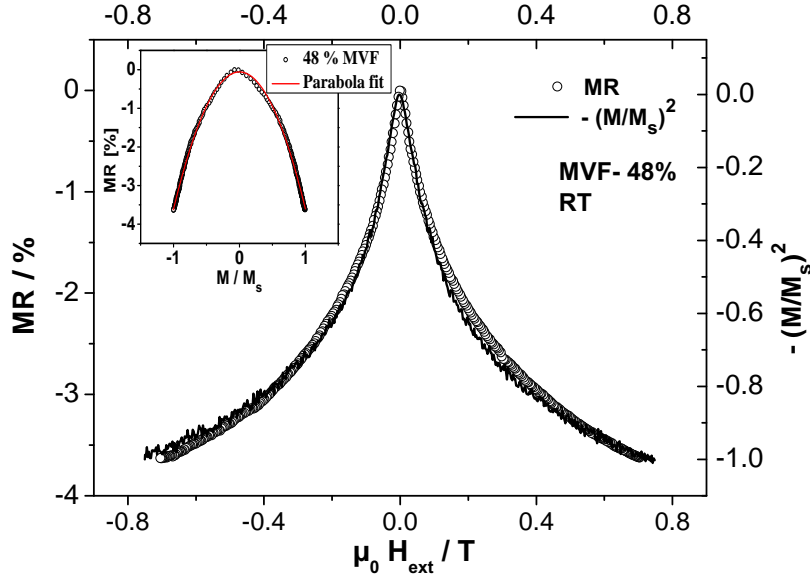


Figure 5.10: TMR as a function of applied magnetic field and square of normalized magnetization  $-(M/M_s)^2$  from VSM measurements at RT for 48%, inset TMR vs magnetization

Inoue *et al.* [44] explained the change in electrical resistance for granular films by spin dependent tunneling of electrons between metal nanograins embedded in an insulating matrix (chapter 2.3). The magnetic moments of the granules in as-deposited composite films are randomly oriented at RT [57]. In the external magnetic field, the relative orientation of magnetization between adjacent grains rotates into a parallel configuration causing increase in tunneling probability. For uniform size superparamagnetic particles with uncorrelated moments, the TMR ratio will be proportional to the square of the relative magnetization of the system,  $\langle \cos\theta \rangle = m^2$  ( $m = M/M_s$ ) where,  $M_s$  is the saturation magnetization [44]. Figure 5.9, 5.10 and 5.11 shows the relationship between MR and the corresponding magnetization curve. The experimental data for MVF 43% and 48% follow quite well the relation  $\Delta R/R_0 \propto -(M/M_s)^2$  implying spin dependent tunneling in FeCo-TiO<sub>2</sub> composite films. For fitting this relation with TMR curves, magnetization  $M$  at  $H = 7.5 \text{ KOe}$  is taken as the saturation magnetization. The inset of figure 5.9 and 5.10 shows the quadratic behaviour of magnetoresistance vs the global magnetisation. However, as expected, the film with

composition near to 53% MVF does not obey this quadratic law (figure 5.11), which means there exists a possibility of interparticle interaction. At this filling factor the FeCo exhibits particle coalescence resulting in multi domain formation. The TMR amplitude rapidly drops and originates from the uncoupled small superparamagnetic particles still present where as the magnetisation is dominated by coalesced clusters.

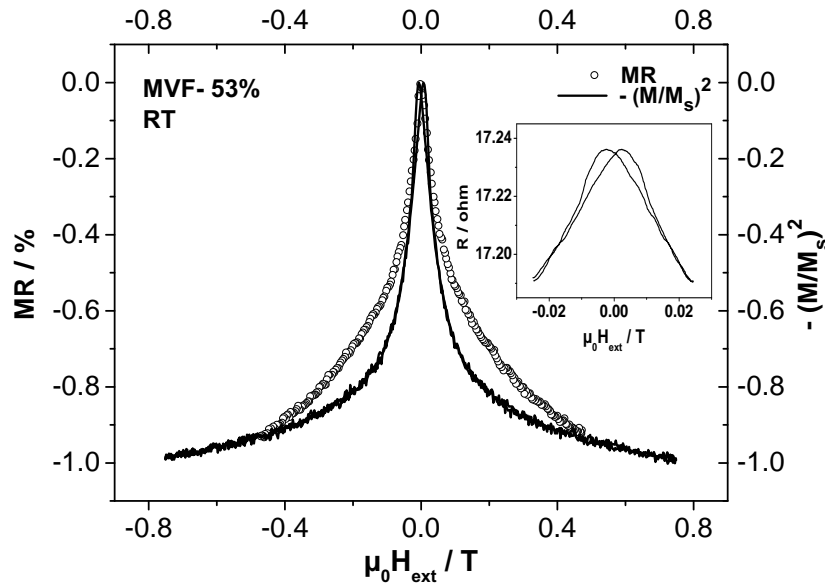


Figure 5.11: TMR as a function of applied magnetic field and square of normalized magnetization- $(M/M_s)^2$  from VSM measurements at RT for 53%, inset TMR vs magnetization

### 5.3.1 Aging

As discussed in the previous chapter the importance of aging in commercial application, the aging behavior of 3D nanocomposite thin films were also studied. Structural changes in the film stored in air for two months (labeled "Aged films") were studied through TEM and EDX. EDX analyses on films (MVF  $\approx$  25 - 30%) indicate an increase of the oxygen content, thus implying the presence of highly oxidized and thus fully ceramic material. In case of the aged films with low MVF, all components are again fully amorphous as supported by bright-field images exhibiting no diffraction

contrast and HRTEM (figure 5.12). Just very broad diffuse intensity concentrating on a concentric circle is seen in the SAED pattern (figure 5.2 left). The diameter of the circle was determined to be  $d \approx 0.27(1)$  nm. The aged films appear chemically and optically homogeneous, and like for the freshly prepared films, the equiatomic ratio of Fe and Co is well adjusted even at nanoscale. EDX nanoprobe-analyses (average of five point measurements, distinct areas) display the homogeneity of the material by low variance of the metal content, Ti : Fe : Co = 43.1(7) at% : 28.3(5) at% : 28.7(1.4) at%. Thus, aging of the films does not produce a detectable segregation of distinct phases. Based on the ceramic nature of the films, the atomic ratio of O : Ti was significantly larger than the expected value of 2.0 for a freshly prepared composite, namely in the range of 3.3 - 3.8. Hence, Fe and Co must be incorporated in an oxidized form inside the materials to meet the criterion of charge balance. Assuming Fe and Co in trivalent and bivalent states, the charge balance is approximately met by the average composition close to  $\text{Co}_{0.56}\text{Fe}_{0.56}\text{Ti}_{0.8}\text{O}_3$ . Such finding confirmed the formation of a homogeneous ceramic film from an amorphous composite by aging. The degradation of the material has no significant influence on the functional properties. Thus, it can be concluded that the aging is restricted to a thin surface layer which protects the internal areas of thicker films against further oxidation.

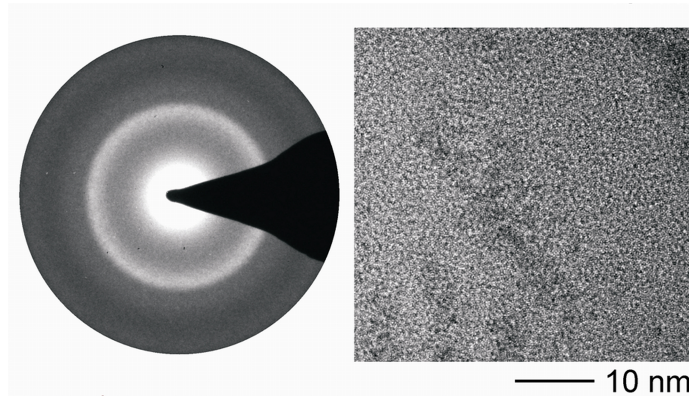


Figure 5.12: SAED pattern (left) and bright-field image (right) of aged nanocomposite film (MVF  $\approx$  25-30%)

The TMR of granular structures is substantially lower than TMR values reported for the best TMR devices fabricated by advanced lithography techniques involving epitaxial oxide layers [101]. Nevertheless due to simple fabrication process the granular TMR approach is tempting for low-cost magnetic field sensors, where highest sensi-

tivity is not required. The knowledge of the morphology and possibility to tune the nanocomposites was utilized in adaptation of the composite as core material for high frequency devices which is the topic of the next chapter.

## 6 3D Nanocomposites as Core Material for High Frequency Application

Another significant field of application for nanocomposites which has been under serious investigation is as core materials for integrated passive components [4, 5, 102]. Ongoing demands for miniaturization in mobile electronic devices as well as steadily increasing operating frequencies of electronic circuits into GHz range are the driving forces [74]. Use of high permeable magnetic cores in the integrated micro-inductors would lead to miniaturization of the geometry, reduction of stray fields compared to air-core coil inductors and increased inductance provided that losses are avoided. As pointed out in chapter 2.4.2, many material properties simultaneously govern the high frequency properties and major factors that limit the performance are eddy currents which arise due to conductivity and frequency limitation due to ferromagnetic resonance. Therefore core material must simultaneously have high electrical resistivity, high saturation magnetization and high permeability in the interested frequency regime to create the desired effects in the devices (chapter 2.4). Several approaches have been developed over the years for the preparation of high frequency materials which complies to above said material properties. One of the approach is use of amorphous alloys such as FeCoBSi [103], CoTaZr [104] and CoNbZr [105]. The resonance frequencies for most of these materials range between 1.5 to 5.0 GHz, permeabilities range between 100 - 500 and have typical electrical resistivity of  $100 \mu\Omega cm$ . These thin films are typically used with an induced in-plane uniaxial anisotropy. Good high frequency properties in these films are resultant of highest possible saturation magnetization and appropriate anisotropy field (1-5 mT). However, a general disadvantage of these amorphous layers is that the eddy current losses appear for film thickness of several hundred nanometers and thereby reducing the cut-off frequency and quality factor of the layer. To circumvent this problem these films have been deposited with

insulating layers in a multilayer arrangement [106, 107, 108] reduction of eddy current losses by using segmented / patterned core by lithography [102, 109].

Another approach to produce high frequency materials is nanocomposites where ferromagnetic particles are incorporated in an electrically insulating matrix. Several kinds of nanocomposites, also known as metal insulator nanogranular films, have been studied in wide range of metal volume fractions. Fe, Co and FeCo with  $\text{Al}_2\text{O}_3$ [110],  $\text{SiO}_2$  [111], ZrO [112], HfO [113, 114],  $\text{MgF}_2$  as insulating matrix have been produced either by reactive sputtering, co-sputtering from two sources, and in some cases by synchronous triple-rf magnetron sputtering. The excellent soft magnetic property is thought to be due to ferromagnetic exchange coupling between magnetic particles. Metal volume fraction is the key parameter to tune the properties of films, e.g., resistivity can be varied from  $100 \mu\Omega\text{cm}$  to  $4000 \mu\Omega\text{cm}$  for 88% to 50% MVF respectively [111]. Thus eddy currents can be effectively suppressed due to high electrical resistivity in these materials. Good high frequency properties have been obtained in MVF ranging between 56% to 75.5%. Ohnunma [112, 93] fabricated FeCo-Zr-O nanogranular soft magnetic thin films with very high magnetic flux density ( $\mu_0 M_s = 2.3 \text{ T}$ ) and permeability of 400, but the imaginary part starts increasing well below 10 MHz resulting in very poor quality factors. Most of the above mentioned composites have been prepared in an external magnetic field during fabrication to obtain an in plane uniaxial anisotropy. However, except in some cases the material quality factor is not in the desired range ( $Q \geq 10$  at 1 GHz). Secondly, in toroidal shape coils the magnetization must be aligned perpendicular to the HF field as in-plane uniaxial anisotropy will lead to interruption of the field distribution. The problem of anisotropy alignment can be overcome by using isotropic cores, radial anisotropy, crossed anisotropy core [115] or by perpendicular anisotropy as proposed by Ramprasad *et al.* [4].

Thus, in this work the focus was to find optimum conditions for isotropic FeCo-SiO<sub>2</sub> nanocomposite films to achieve good material quality factors in the GHz frequency range, high electrical resistivity and reasonable permeability even for film thickness in micrometer range. Fe<sub>50</sub>Co<sub>50</sub> which has highest saturation magnetization ( $\mu_0 M_s = 2.4 \text{ T}$ ) among the ferromagnetic materials [24] may lead to very high self-resonant frequency thus makes the alloy a promising candidate for high frequency applications. In this thesis, apart from ceramic based composites, polymer based

nanostructured materials which was the topic of doctoral thesis of H. Greve [12] were further investigated. In the later part of this chapter, successful integration into toroidal micro-inductor which is a joint DFG project at the Faculty of Engineering, Kiel, will be presented. The HF characterization of composites was carried out at Microwave group held by R. Knöchel at Institute of Electrical and Information Engineering. Toroidal micro-inductors were fabricated by the group of E. Quandt at Institute of Materials Science-Inorganic Functional Materials into which ceramic and polymer based nanocomposites were integrated.

## 6.1 FeCo-SiO<sub>2</sub> system

The FeCo-SiO<sub>2</sub> nanocomposites were prepared by co-sputtering from FeCo alloy and SiO<sub>2</sub> targets by magnetron sputtering. Metal volume fraction was varied by keeping the power on FeCo target constant and varying that of SiO<sub>2</sub>. Nanocomposites were deposited on Si/SiO<sub>2</sub> substrates (5 x 5 mm and 2 x 10 mm) for magnetic and high frequency characterizations respectively and on TEM grids for microstructure analysis. In plane uniaxial anisotropy was induced by an external magnetic field during deposition. High frequency permeability was measured by high frequency permeameter (chapter 3.4.3).

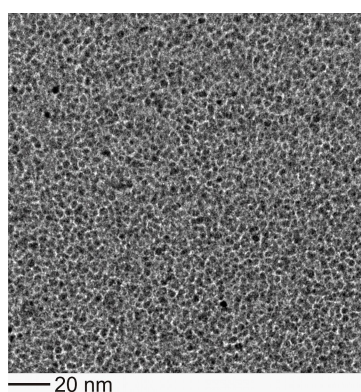


Figure 6.1: Bright field Transmission electron microscopy image for 30 nm FeCo-SiO<sub>2</sub> nanocomposite film with 50% MVF.

Figure 6.1 shows a TEM bright field image for FeCo-SiO<sub>2</sub> nanocomposite film consists of FeCo nanoparticles embedded in an insulating SiO<sub>2</sub> matrix. FeCo nanoparticles are crystalline in nature with average size of 4 - 5 nm and SiO<sub>2</sub> is amorphous. The morphology is in line with the discussion presented in chapter 5.1 in detail.

Figure 6.2 shows the effect of metal volume fraction on resistivity and saturation magnetization of the nanocomposite films. Electrical resistivity changes several orders of magnitude, from 10<sup>6</sup> μΩcm to 10<sup>2</sup> μΩcm for 35% to 70% MVF respectively. At ≈ 48% metal volume fraction it decreases rapidly. This change in electrical resistivity as function of metal volume fraction can be explained by percolation theory (chapter 2.1.1). At low MVF nanoparticles are isolated from each other and as it increases the resistivity decreases as connecting network of nanoparticles start to form and hence more paths are available for conduction through the film. From purely theoretical considerations for spherical particles the calculated percolation value is 29%. However experimentally determined percolation threshold value for many granular films is in the range of 50% to 60% [1, 116, 117] as in real systems one has to consider particle size distribution, deposition process etc. Still the resistivity for 65% MVF film is 2000 μΩcm which is three orders of magnitude higher than the bulk material. As it is seen later, this magnitude does not cause eddy currents which are crucial for the high frequency applications.

Prior to the deposition of nanocomposite, FeCo film was sputter deposited in order to make sure that the saturation magnetization is reached to the specified value of the target material. Typical μ<sub>0</sub>M<sub>s</sub> values of 2.1 T - 2.2 T were obtained for 100 nm thick FeCo films. As seen from figure 6.2 addition of SiO<sub>2</sub> decreased the saturation magnetization. Unlike in the films co-deposited from ferromagnetic and organic compound, where the films completely lose their ferromagnetic property due to chemical reactions, in case of ceramic matrix the reactions are not that severe. However, formation of thin oxide shell around FeCo particles cannot be overruled as the saturation magnetization decreased on addition of SiO<sub>2</sub>.

The magnetization loops of the nanocomposite films with different metal volume fraction are shown in figure 6.2. As discussed in chapter 5.2, magnetization curves correlate strongly with the metal volume fraction. For FeCo-TiO<sub>2</sub> system superparamagnetic

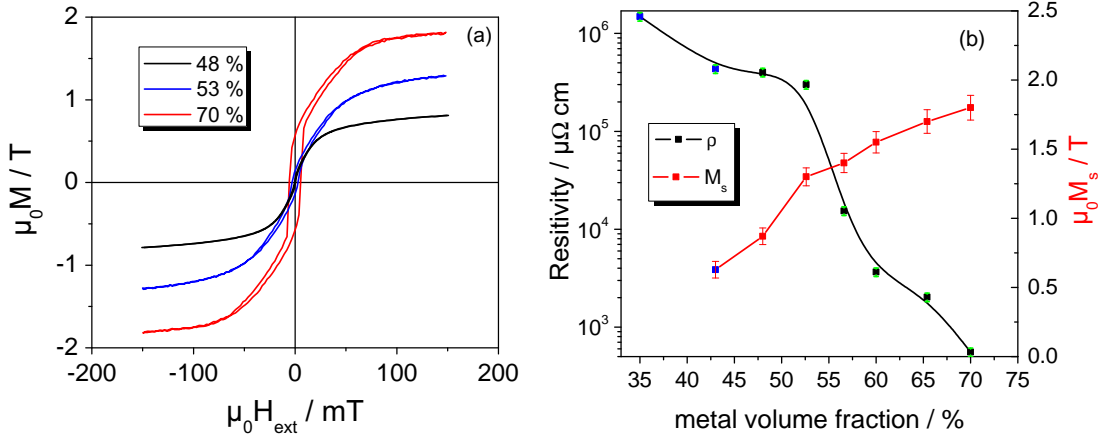


Figure 6.2: (a) Magnetization loops for FeCo-SiO<sub>2</sub> with different metal volume fraction (b) Resistivity and saturation magnetization as a function of metal volume fraction for FeCo-SiO<sub>2</sub> and FeCo-TiO<sub>2</sub> films (blue symbol); in figure (b) lines are just guidelines to the eye.

behavior was observed below 50% MVF. Same phenomena was seen in FeCo-SiO<sub>2</sub> system as well. As seen in figure 6.2 the magnetization curves show distinct behavior with respect to MVF, changing from the superparamagnetic to ferromagnetic state. As the metal volume fraction increases FeCo clusters grow in size and separation between them decreases. When the metal volume fraction is above the percolation threshold coalescence between neighboring particles occurs. Coalescences cause formation of clusters with multidomain structure. Asakura *et al.* [23] in their work on  $\text{Co}_x\text{-(SiO}_2\text{)}_{100-x}$  granular films observed that the domain formation and its structure strongly correlates to the electrical percolation (chapter 2.1.1). For concentration below percolation composition ( $x_p$ ) 45%, domain structure disappears and stripe domain were observed in the Co-rich region.

The high frequency permeability spectra for films prepared without magnetic field during deposition are shown in figure 6.3. The permeability increases as the filling factor increases and the ferromagnetic resonance frequency is between 2-3 GHz. Ramprasad *et al.* [4] in their work on magnetic nanoparticles dispersed in polymer matrix showed that the effective permeability of the composite increases with particle volume fraction, which is the case here. Further, for the materials parameters ( $\mu_0 M_s = 2.4T$ ,  $\mu_0 H_k = 49mT$  and conductivity  $\sigma = 1.10^7 S/m$ ) they showed that the composites with

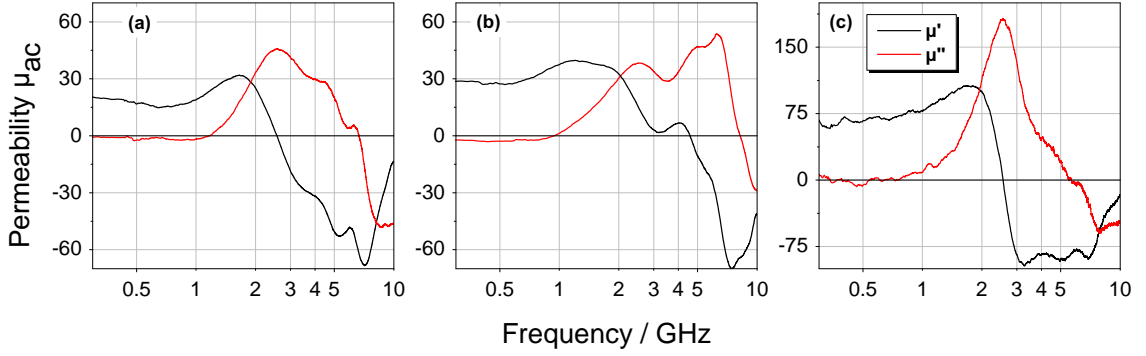


Figure 6.3: High frequency permeability of 200 nm thick FeCo-SiO<sub>2</sub> with different metal volume fraction (a) 53%, (b) 65% and (c) 70%

nearly spherical particles and filling factor between 0.45 to 0.55 are expected to have a permeability of  $\mu_{eff} = 3 - 18$  and resonant frequency  $f_{FMR} = 18 - 10GHz$ . It should be kept in mind while designing the nanocomposites that in co-sputtering process, as the metal volume fraction is increased the particles may touch and the effective size will eventually be higher than 100 nm which will lead losses due to eddy currents.

Apart from the normal eddy current losses, other structural effects like domain structure, demagnetization fields, magnetization dispersion have significant influence on HF characteristics of the material [118]. These effects could be investigated by applying external DC field perpendicular to the HF field [119]. Biasing is also useful to fix the direction of anisotropy, shift the cut-off frequency to higher values and change the permeability [118]. Figure 6.4 shows the effect of external static magnetic field on the permeability and FMR frequency of FeCo-SiO<sub>2</sub> nanocomposite film. Directions of fields involved are shown schematically in figure 6.4 inset. According to theory,  $f_{FMR} \propto \sqrt{M_s(H_k + H_{dc})}$  and  $\mu = \frac{M_s}{(H_k + H_{dc})} + 1$ , by applying additional DC field perpendicular to the HF field FMR frequency can be shifted to higher values and as a result the permeability should go down. However, for the nanocomposite films deposited without magnetic field, the permeability first increases from 50 to 400 and then gradually decrease. The FMR shifts from 2 GHz to 6 GHz as predicted by ferromagnetic resonance theory. From the behavior of permeability with respect to external field it may be inferred that, initially not all the magnetic moments are aligned perpendicular to the HF field and the additional  $H_{DC}$  during measurement aligns them. This in principle indicates that the films deposited without external magnetic field

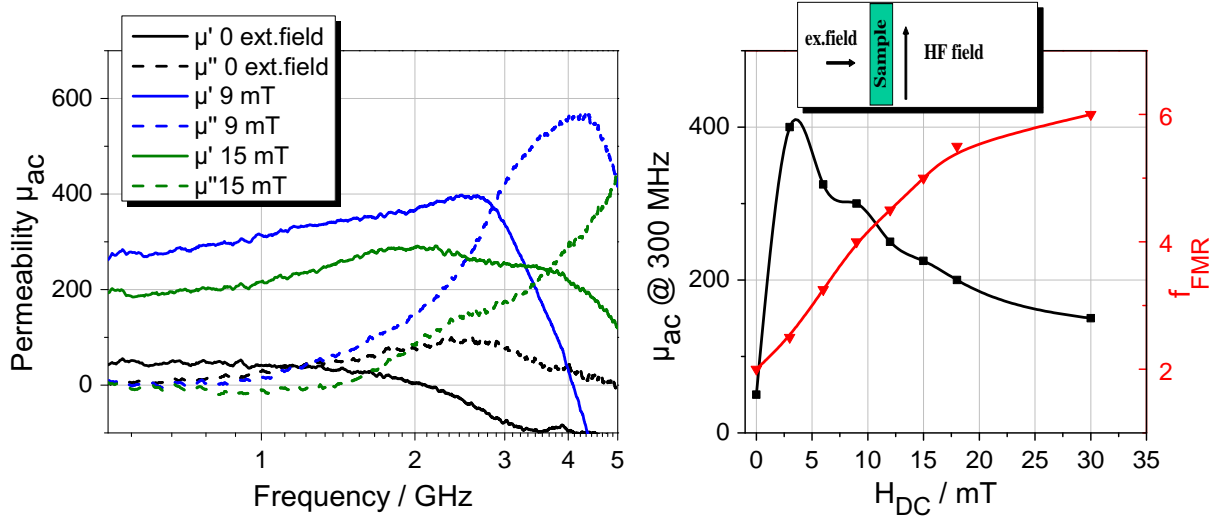


Figure 6.4: Permeability and ferromagnetic resonance frequency as a function of external  $H_{DC}$  field applied in the direction perpendicular to HF field. Sample under investigation is FeCo-SiO<sub>2</sub> with 70% MVF.

are magnetically inhomogeneous and permeability can be further increased to large extent by optimization of the nanocomposite morphology to achieve soft magnetic properties.

### Deposition with an external magnetic field

Magnetic hysteresis loop of FeCo-SiO<sub>2</sub> containing 65% metal volume prepared under magnetic field (250 mT) is shown in figure 6.5. Coercive field along easy and hard directions are 5.7 mT and 4.8 mT respectively. For the films with same filling factor prepared under magnetic field, the permeability spectrum is dramatically better (figure 6.6). The HF permeability is five folds high compared to the films without induced anisotropy. Ferromagnetic resonance frequency is around 3.1 GHz and material quality factor  $Q$ , given by  $\mu'/\mu''$ , is quite high below 2 GHz. The imaginary part of the permeability shows a narrow peak width which is advantageous as the magnetic loss around FMR frequency depends on the line width [120]. Compared to the films prepared without external magnetic field (figure 6.2) these films are easy to saturate which probably explains the increased permeability. FeCo-SiO<sub>2</sub> nanocomposites show reasonably good HF properties in spite of slight reduction in the saturation magnetization.

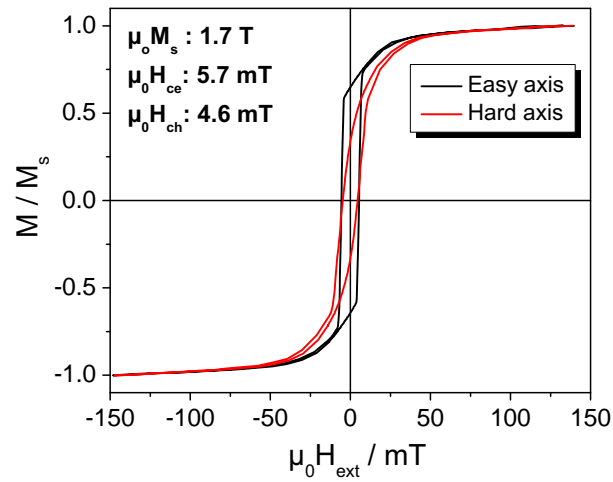


Figure 6.5: Magnetization loop of 200 nm thick FeCo-SiO<sub>2</sub> with 65 % MVF deposited under an applied magnetic field during sputtering

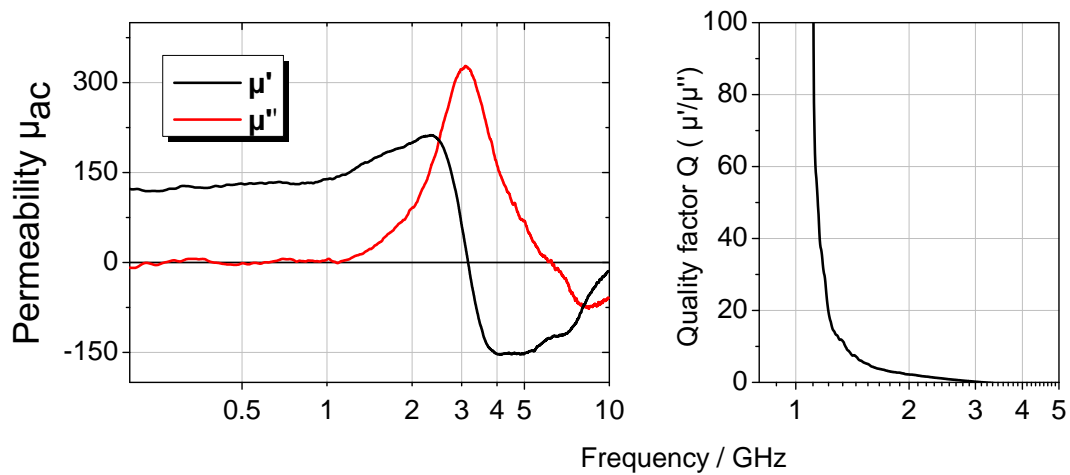


Figure 6.6: High frequency permeability of 200 nm thick FeCo-SiO<sub>2</sub> with 65 % MVF along hard axis and the corresponding quality factor. The films were prepared under an external field

### Microstructure and HF characteristics upon annealing

It is important to understand how the functional properties change when subjected to post preparation annealing. Two sets of nanocomposite films were selected for the annealing experiments: one in which MVF is in the vicinity of percolation threshold (53%) and other above percolation (70%). The films were annealed in vacuum,  $1 \times 10^{-6}$

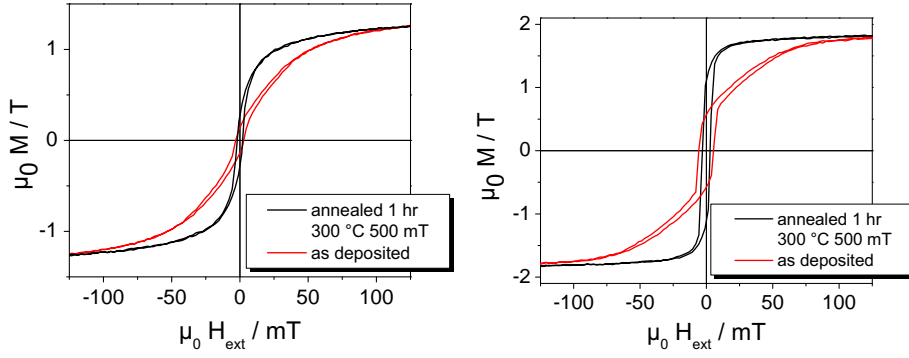


Figure 6.7: Magnetization of loops of as deposited and field annealed composite film for 53 % MVF (left) and 70 % MVF (right)

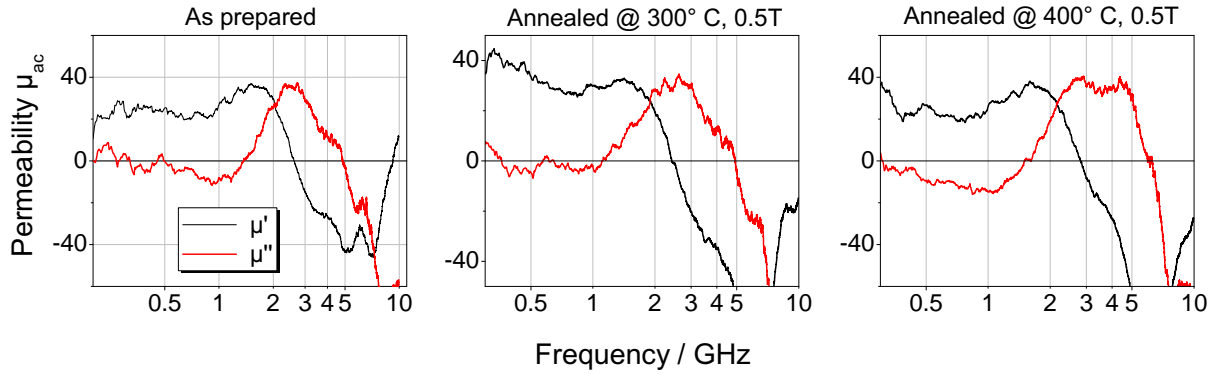


Figure 6.8: HF permeability of 200 nm thick FeCo-SiO<sub>2</sub> composite film with 53% MVF field annealed under different conditions.

mbar for 1 hour with and without external magnetic field. Both sets of films show distinct behavior in comparison to each other upon annealing. The magnetization loops for as prepared and annealed films under different conditions for 53 % MVF are shown in figure 6.7. The loops become softer when compared to as prepared films with no change in coercivity and also no in-plane anisotropy was observed from the magnetization loops. The corresponding HF characteristics are shown in figure 6.9. The permeability tends to increase by  $\approx 50\%$ .

The scenario is quite different for films with considerably higher MVF (figure 6.9). In general, post-deposition annealing is associated with microstructural changes such as grain growth and relaxation of residual stresses. After annealing at moderate temperatures, already percolating network has higher probability to form electrically conduct-

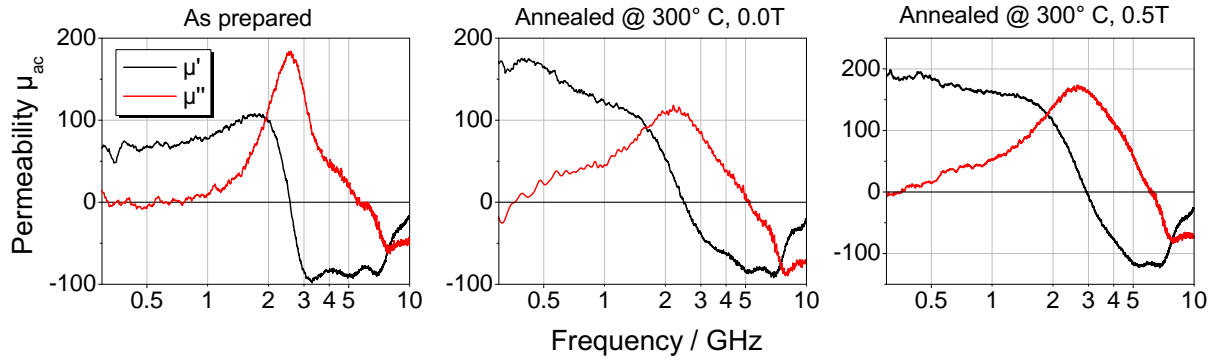


Figure 6.9: HF permeability of 200 nm thick FeCo-SiO<sub>2</sub> composite film with 70% MVF annealed under different conditions

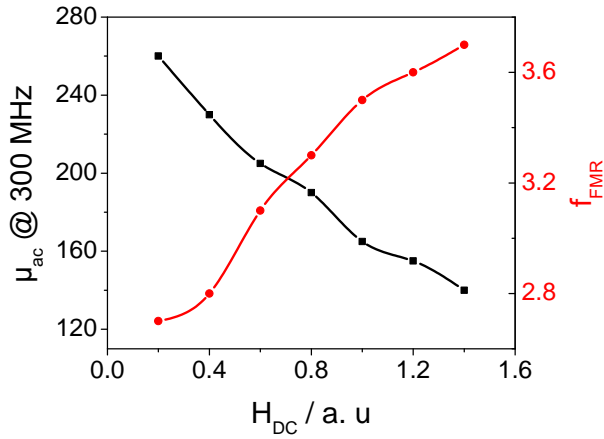


Figure 6.10: Permeability and ferromagnetic resonance frequency as a function of external  $H_{DC}$  field applied in the direction perpendicular to HF field. Sample under investigation is 200 nm thick FeCo-SiO<sub>2</sub> composite film with 70% MVF annealed at 300° C for 60 min; lines are just guidelines to the eye

ing networks. The HF permeability of annealed films show close to three times increase in permeability but the imaginary part starts increasing well below GHz, which results in poor quality factors. These films were also characterized by applying external static field (figure 6.10). Unlike as seen in the previous section the permeability instead of increasing, decreases as the magnitude of the external static field is increased, demonstrating characteristics of closed film [118]. Therefore one could say that poor quality factors are results of eddy currents. Also, the real part of permeability does not show well resolved resonance peak. Increase in the permeability is accounted by

considering the fact that upon annealing films show soft magnetic characteristics with considerable increase in  $M_r/M_s$  ratio compared to the non-annealed film. Therefore, for integration of the core material into toroidal micro-inductor a filling factor which is between 60 and 70 is chosen to avoid the effects of eddy currents.

### **Nanocomposite film with 1 micron thickness**

Often thick core materials in the range of few micrometers are necessary to sufficiently influence the flux amplification in the magnetic devices they are integrated into. Therefore 1  $\mu m$  thick FeCo-SiO<sub>2</sub> film was prepared and characterized with respect to resistivity and HF permeability. Even though the composite films deposited under magnetic field showed superior HF properties 6.6 compared to the films prepared without an external magnetic field during deposition, the later was used for integration into toroids. The reason being, as mentioned before in-plane uniaxial anisotropy will lead to interruption of the field distribution in the toroid. Increase in film thickness from 200 nm to 1  $\mu m$  resulted in decrease in electrical resistivity from  $2000\mu\Omega cm$  to  $900\mu\Omega cm$  which is still considerably higher than the amorphous alloys. Deposition of additional SiO<sub>2</sub> layers for every 100 nm FeCo-SiO<sub>2</sub> composite layer resulted in increase in the electrical resistivity to  $1800\mu\Omega cm$ . HF permeability and the quality factor for 1  $\mu m$  thick film are shown in figure 6.11. The material quality factor Q is greater than 25 at 1 GHz and shows reasonable permeability of 20. The thickness of the film used must be lower than the skin depth in order to avoid induced eddy current losses. Skin depth  $\delta$  is a function of resistivity and frequency, the calculated values for different scenarios are presented in figure 6.12.

## **6.2 FeNiCo/PTFE multilayer**

Nanostructured FeNiCo/PTFE multilayer thin films have been investigated previously in detail with regard to their microstructure and magnetic properties in the work of H. Greve [121]. The multilayer films show excellent high frequency characteristics with permeabilities above 100 and FMR frequency up to 5 GHz. Highest permeability of

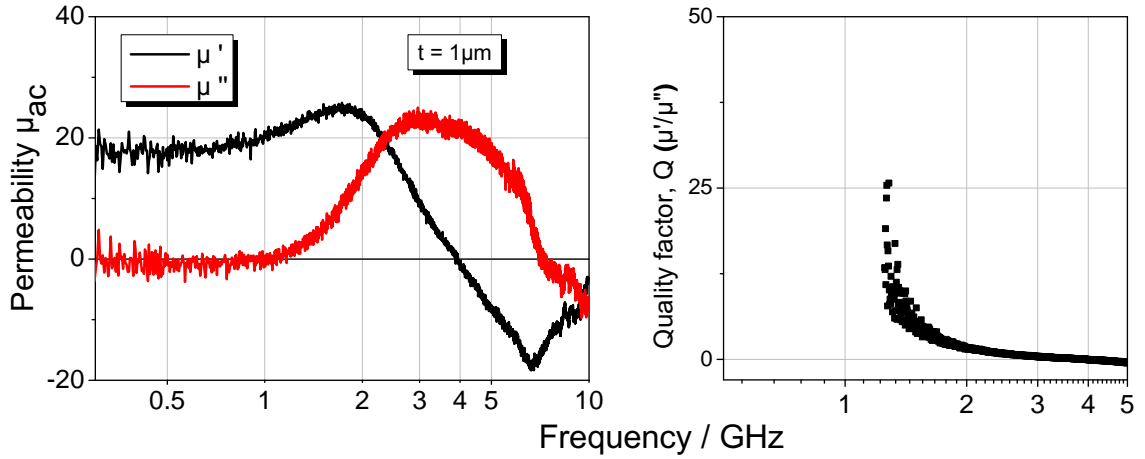


Figure 6.11: HF permeability and quality factor of 1  $\mu m$  thick FeCo-SiO<sub>2</sub> nanocomposite film with 65% MVF prepared without the external magnetic field during deposition.

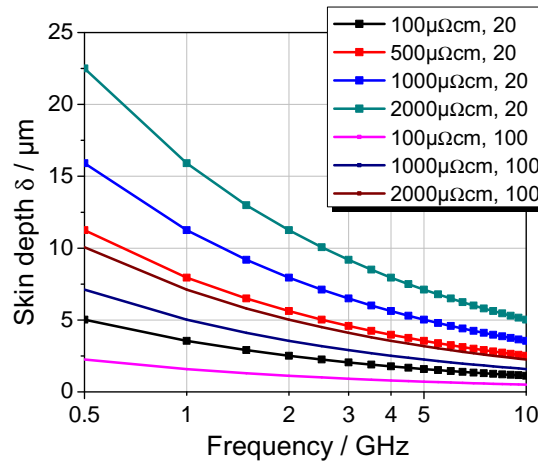


Figure 6.12: Skin depth estimated for different values of resistivity and permeability. Resistivity for 1 micrometer thick FeCo-SiO<sub>2</sub> nanocomposite film is 1800  $\mu\Omega cm$ .

175 at 100 MHz was achieved for (20 nm FeNiCo / 10 nm PTFE) multilayer film. In continuation with this work, effects of post preparation thermal treatment on HF properties were investigated. The films did not show any degradation up to 300 °C. Since substantially thick core is required for the micro-inductor, 1.5 micron thick FeNiCo/PTFE multilayer were prepared for integration into toroidal micro-inductor.

Figure 6.13 shows the magnetization curve and the HF permeability spectra of films consisting 38 alternating layers of FeNiCo (25 nm) and PTFE (10 nm). The films have permeability up to 175 and FMR occurs at 3.0 GHz.

When compared to FeCo-SiO<sub>2</sub> prepared without magnetic field during deposition, isotropic FeNiCo/PTFE show higher permeability. However, films prepared under magnetic field show opposite behavior, the nanocomposites system have almost twice the permeability as that of FeNiCo/PTFE (also prepared under magnetic field [122]). A comparison between two systems is given in figure 6.14.

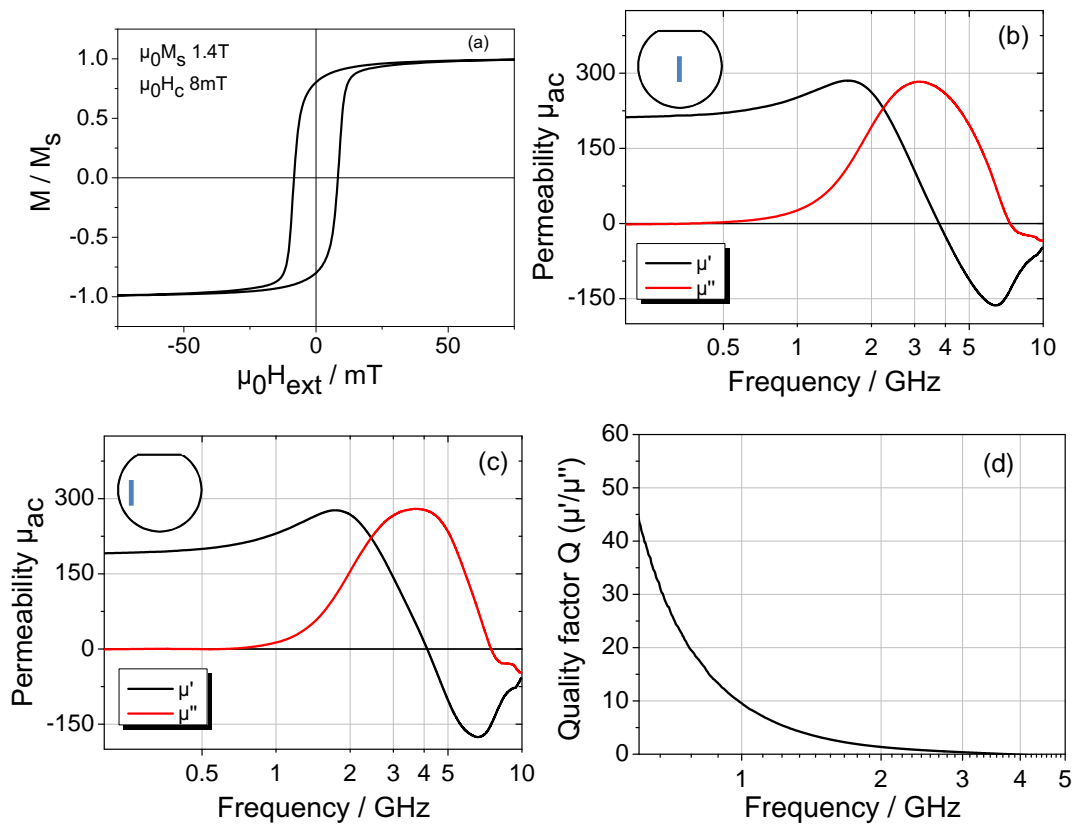


Figure 6.13: (a) Magnetization curve (b) and (c) the HF permeability (d) the corresponding material quality factor of 1.5 micron thick multilayer film consisting of 38 (25 nm FeNiCo/10nm PTFE) layers. Also indicated is the sample position on a 4 inch wafer.

Type	Parameters	$\mu'$ @ 500 MHz	$f_{\text{FMR}}$ / GHz
FeCo-SiO <sub>2</sub>	200 nm without induced anisotropy	20	3
FeCo-SiO <sub>2</sub>	1000 nm without induced anisotropy	20	3
38(25 nm FeNiCo + 10 nm PTFE)	1500 nm without induced anisotropy	175	3
4(30 nm FeNiCo + 10 nm PTFE)	160 nm with induced anisotropy	60	4.8
FeCo-SiO <sub>2</sub>	200 nm with induced anisotropy	140	3.2

Figure 6.14: Comparison of HF characteristics of FeCo-SiO<sub>2</sub> (65 % MVF) and FeNiCo/PTFE systems

### 6.3 Integration of core into toroidal thin film inductor

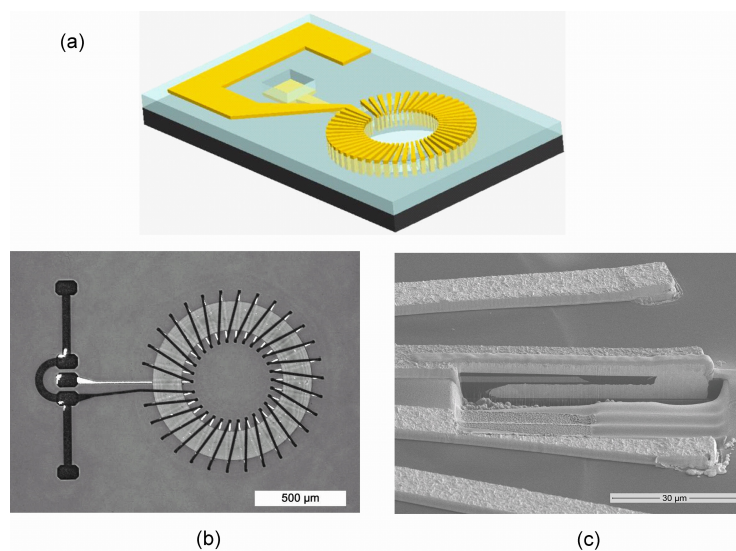


Figure 6.15: Schematic representation of the toroidal micro-inductor (b) Light microscope image with composite magnetic core 1mm dia, 30 windings (c) cross-sectional SEM image of the completed micro-inductor

Toroidal shape inductor has optimum properties for application in HF devices especially as it has closed magnetic ring core hence stray fields can be minimized to greater extent [123]. Schematic representation of such micro-inductor is shown in figure 6.15. The wafer consists of number of inductors with diameter 0.3 mm and 1 mm with 15 and 30 winding respectively. The fabrication consists of several steps involving combination of electroplating and photolithography [124]. As substrates, Si wafers were used. For electrical insulation and to ensure a homogeneous surrounding, 34  $\mu\text{m}$  of Cyclotene 4026-46, a photosensitive polymer based on B-staged benzocyclobutene (BCB) were applied. Since the bottom coil wiring and the vias were deposited by electroplating, 100 nm of Au as seed layer and 20 nm of Cr as adhesion promoter were deposited by magnetron sputtering. Structuring the negative photoresists ma-N 440 and ma-N 490 (Micro resist technology GmbH) for use as a mask for electroplating was done by UV lithography. Gold was deposited by electroplating for the bottom coil windings and the vias with a thickness of 9  $\mu\text{m}$  and 3.5  $\mu\text{m}$  respectively. After removal of the seeding layer by IBE, BCB was spin coated to get a layer of a thickness of 20  $\mu\text{m}$ . It was then dry etched using an ICP-RIE system to leave an insulation of less than 1  $\mu\text{m}$  on top of the bottom coil wiring. Then, the magnetic core of 1  $\mu\text{m}$  thick was deposited. After structuring using IBE and the positive photoresist AZ 6632 (Micro Chemicals) as a mask, BCB was deposited and etched until the top of the vias was free. Then, the top coil wiring were deposited by electroplating in the same manner as the bottom coil wiring before, now for a thickness of 20  $\mu\text{m}$ . Both PTFE/FeNiCo composites and FeCo-SiO<sub>2</sub> nanocomposite were integrated into the toroidal micro-inductor. The HF properties of integrated toroidal micro-inductor were characterized by network analyzer [73].

Figure 6.16 shows the frequency dependence of inductance of 1 mm dia toroid with integrated magnetic core. The enhancement in inductance on addition of magnetic core in both the systems is in the range of 20-30%. The roll-off in inductance occurs at 3 GHz in both the systems. What is interesting to see is that even though the permeability of metal/polymer system is much larger than the FeCo-SiO<sub>2</sub> system, it is not reflected in the flux amplification. Even though the inductors operate above 1GHz, the enhancement in the inductance and quality factor is of concern. It is still not sufficient enough to compete with the existing air core inductors. One reason could be the low filling factor, i.e., the volume of the magnetic core of the present inductor

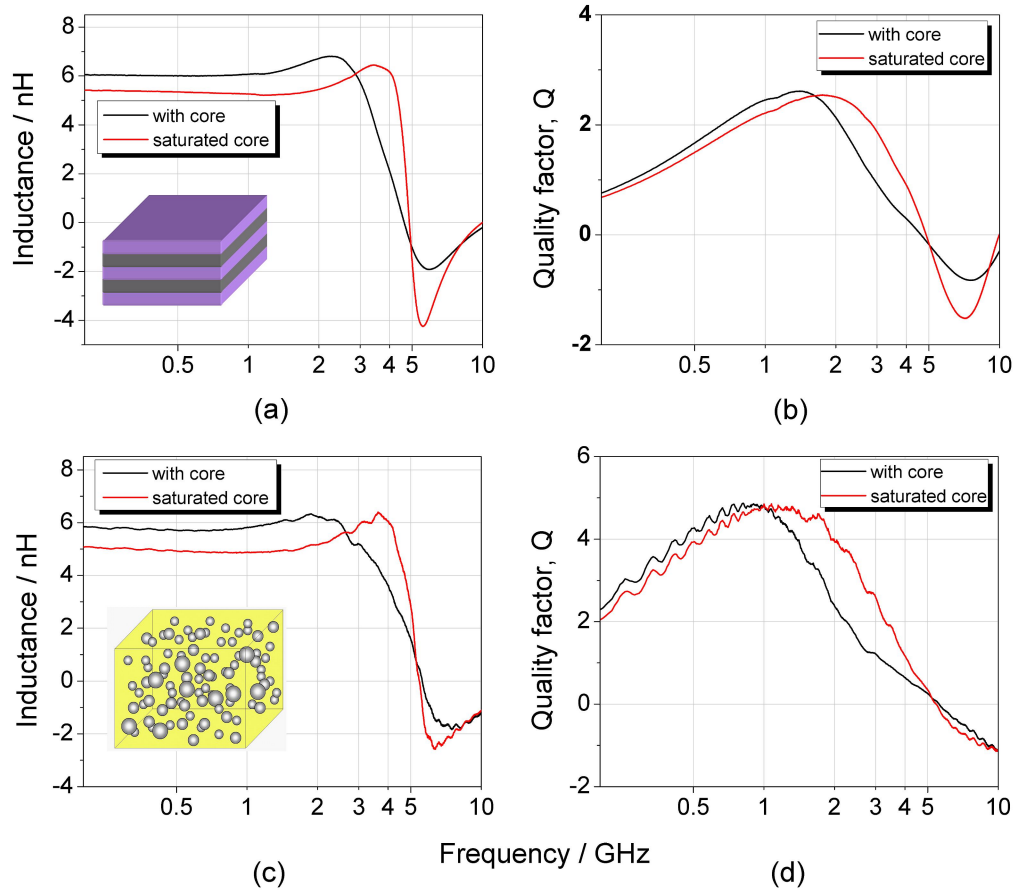


Figure 6.16: Inductance and quality factor of toroidal micro-inductor with magnetic core (a),(b) 38(25 nm FeNiCo/10 nm PTFE multilayer) and (c),(d) 1 micron thick FeCo-SiO<sub>2</sub>.

( $\approx 10\%$ ). In order to ascertain this, simulations were performed for thicker core material using electromagnetic field simulation tool HFSS at the Institute of Electrical Engineering, Technical Faculty CAU Kiel. The high frequency characteristics of FeCo-SiO<sub>2</sub> (figure 6.11) was taken as the reference material. Simulation results show that the inductance increases linearly as the thickness of core material increases (figure 6.18). With the thicker core it is possible to achieve fivefold increase in the inductance and the corresponding quality factor can be also be increased by adjusting the dimensions of the vias (i.e., lowering the dc resistance). At present, the preparation of thicker core material is limited by the possible size of the sputtering target material used in deposition chambers. Nevertheless, the high frequency behavior of thicker core must be studied with respect to eddy currents and the peak broadening effects if any.

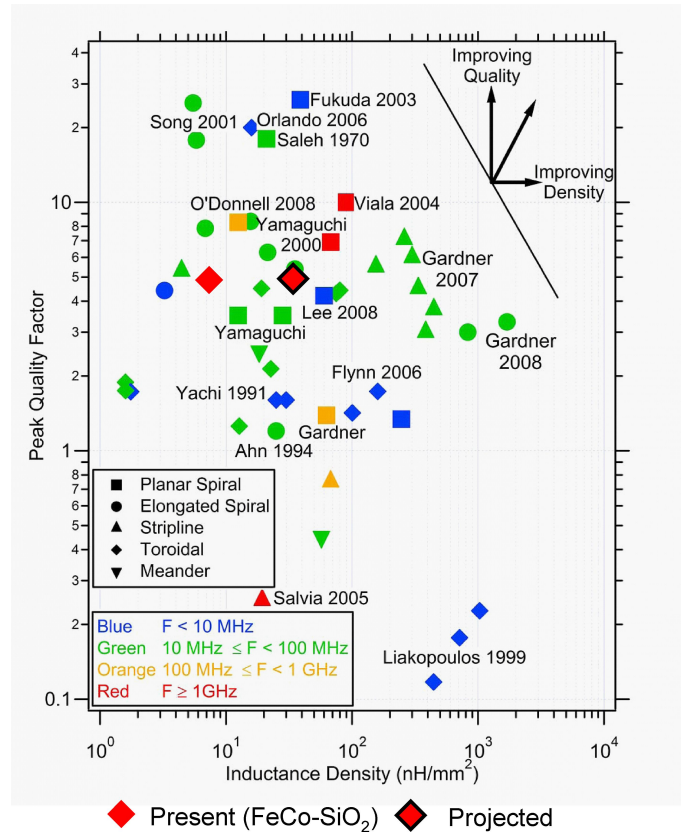


Figure 6.17: Inductance density versus peak quality factor of integrated inductors from [125]. Also indicated is the inductor fabricated during this work and projected based on simulations.

In figure 6.17 shown is a picture describing a survey of on-chip inductors from work of Gardner *et al.* [125]. According to the survey, there exist only three instances showing stripline and planar spiral micro-inductors operating at frequency above GHz (red marking). Results of the inductor from this work have also been put on the graph for comparison and it is unique in terms of being the only toroidal micro-inductor operating in GHz regime. The survey highlights the technological challenges in developing a core material and its integration considering the optimization of complex web of material properties. Part of the above discussion are excerpted from a publication Schürman *et al* [124].

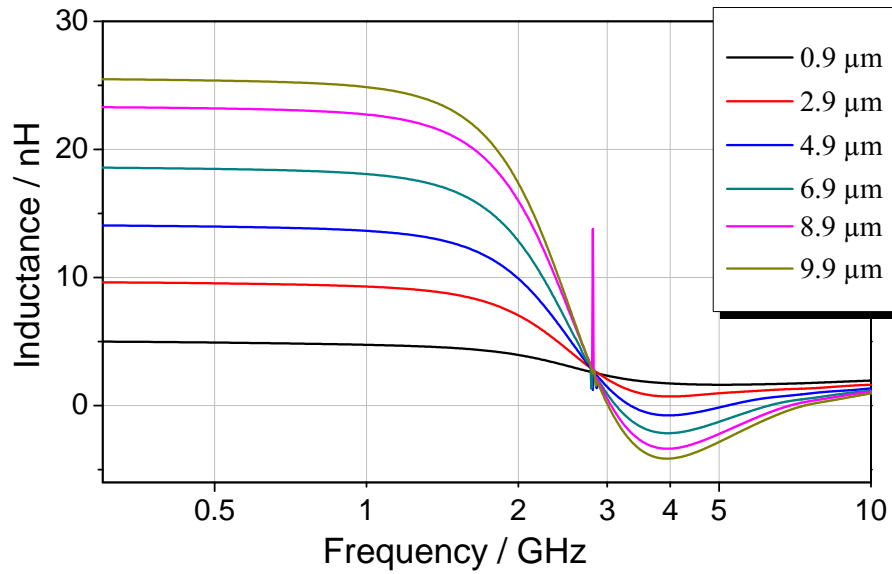


Figure 6.18: Simulation results for 1 mm dia with 30 windings toroid for different magnetic core heights keeping other parameters constant.

## 6.4 Alternative approaches

Nanocomposites/nanoparticle arrays can be synthesized by number of other ways than physical vapor deposition technique presented here. Nanoparticle arrays are of great interest because of their potential applications in plasmonics [126], as a catalyst for growth of other materials and sensors [127]. For well ordered nanoparticles top down lithography techniques are most suitable as they offer excellent control over size and inter particle distance. As the dimension goes down the process becomes increasingly difficult and expensive. Nanoparticle arrays can also be formed by dewetting of a thin film deposited on a substrate [128, 129, 130]. With the templated substrate [131] it is even possible to control the feature size and shape. In case of magnetic nanoparticles directional growth can be achieved by an external magnetic field during heating process.

In following section formation of Co nanoparticles through annealing of Co-SiO<sub>2</sub> multilayer will be presented. Ramprasad *et al.* [4] showed that particles approximately between sphere and rod with aspect ratio 2 have optimum low frequency permeability and high FMR frequency. So the idea here is to anneal the multilayer films in magnetic

field to align the easy axis in the direction needed and to induce shape anisotropy by dewetting. In this direction, initial experiments were performed without the magnetic field.

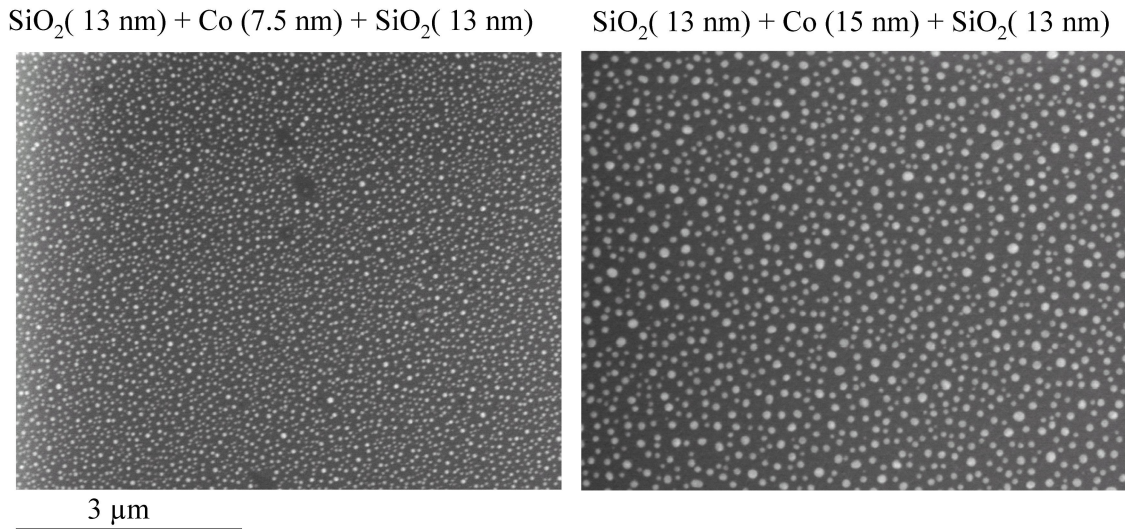


Figure 6.19: SEM image of trilayer films on Si/ SiO<sub>2</sub> substrate: a) 13nm SiO<sub>2</sub> + 7.5nm Co + 13nm SiO<sub>2</sub> and b) 13nm SiO<sub>2</sub> + 15nm Co + 13nm SiO<sub>2</sub>

To start with, annealing of cobalt thin film (7.5 nm and 15 nm) sandwiched between two SiO<sub>2</sub> layer was carried out. Films were prepared by sequential deposition of Co and SiO<sub>2</sub> in magnetron sputtering system by separate targets. Annealing was done in ultra high vacuum ( $1 \times 10^{-7}$  mbar) for an hour at 800° C. Figure 6.19 shows SEM images of Co nanoparticles formed through annealing of SiO<sub>2</sub>/Co/SiO<sub>2</sub> trilayers. Dewetting is a self-agglomeration phenomenon due to annealing at high temperature [132]. The average size and the interparticle distance depend on the initial Co film thickness. Figure 6.20 shows the bright field TEM images taken during *in-situ* annealing. Co films begin to change after 600 °C. At temperature of 800 °C of the heating stage one can see the dewetting and agglomeration. Since the heating stage was cooled down immediately after reaching the desired temperature (850 °C), enough time was not available for completion of dewetting.

Likewise, alternating layers of Co (10 nm) and SiO<sub>2</sub> (10 nm) deposited onto a Si/SiO<sub>2</sub> substrate were annealed at 800° C in vacuum for 60 minutes. Figure 6.21 shows in-plane magnetization loops of as deposited and annealed Co-SiO<sub>2</sub> multilayer films. The

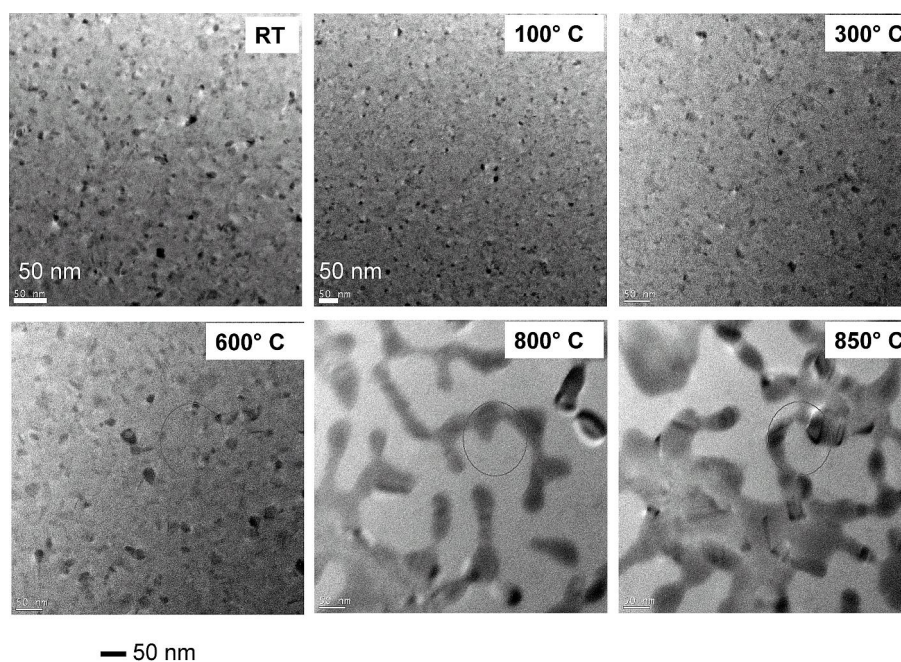


Figure 6.20: TEM bright field images taken at different temperatures during *in-situ* heating of trilayer 13nm SiO<sub>2</sub> + 7.5nm Co + 13nm SiO<sub>2</sub>. Please note the scale difference w.r.t to the SEM image of figure 6.19, the black spots seen in TEM images do not represent the nanoparticles.

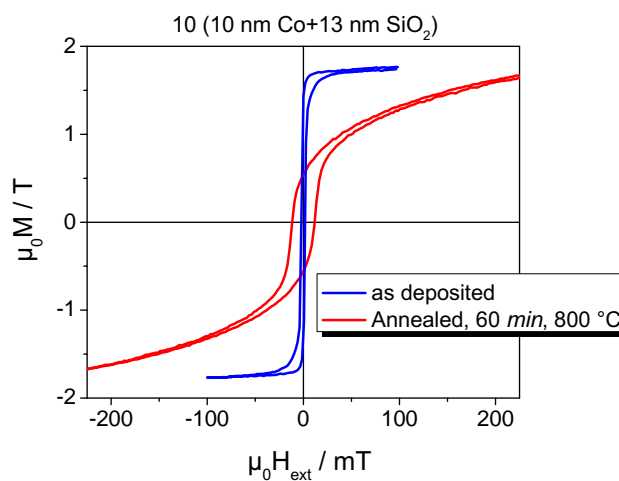


Figure 6.21: Comparison of magnetization loops of as deposited and annealed Co-SiO<sub>2</sub> multilayer. Annealing was done in vacuum  $1 \times 10^{-7}$  mbar for 60 min at 800 °C

as deposited film shows soft magnetic property with 2 mT coercive field and saturation field of 30 mT. The saturation magnetization is 1.7 T which is very close to bulk values of Co (1.8 T [24]). The annealed films show sixfold increase in coercivity (12 mT) perhaps due to single domain particles. If it is to be believed that the morphology in multilayer system is similar to that of trilayer (figure 6.19), then the magnetization loop corresponds well with the microstructure. Annealing at this temperature will destroy the initial multilayer structure due aggregation of Co layer [133].

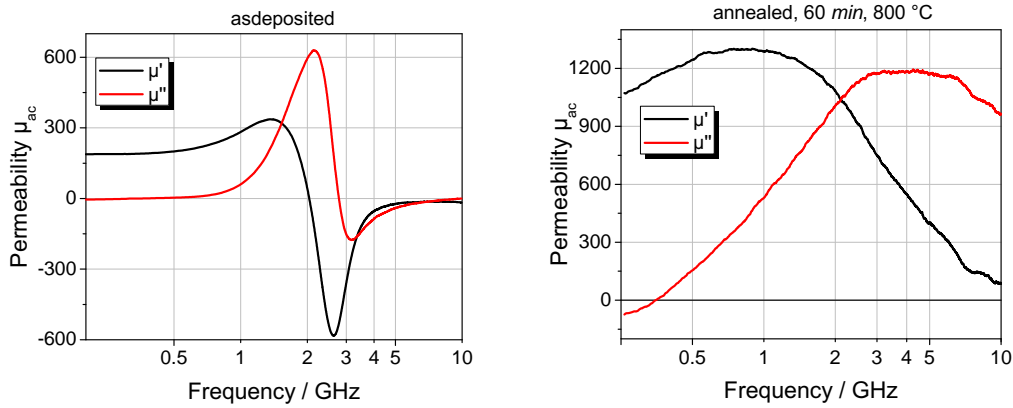


Figure 6.22: High frequency permeability spectra of as deposited and annealed Co-SiO<sub>2</sub> multilayer. The films were annealed in vacuum  $1 \times 10^{-7}$  mbar for 60 min at 800 °C

The high frequency characteristics of these films are shown in figure 6.22. As deposited films have permeability of 100 with good material quality factor comparable to PTFE/FeNiCo multilayer films discussed before. The narrow line width and FMR frequency well over 1 GHz also makes them good candidate for high frequency applications. Annealed samples show tenfold increase in permeability but the imaginary part of the complex permeability increase well below GHz frequency. A plausible explanation would be that the particles are in multi domain state as for a random distribution of magnetization, single domain particles would be expected to show remanence of 0.5 but we see a value which is clearly smaller (figure 6.21). Domain walls in nanoparticles can also respond to high frequencies (due to short distances) which would then lead to high losses as observed here. Further experiments are necessary in the direction of increasing the annealing time to complete the dewetting into separated particles, to understand the HF response.



## 7 Summary and Outlook

This dissertation addresses preparation and characterization of polymer and ceramic based nanocomposites and explores their potential application in the field of tunnel magnetoresistance, as strain sensor and as materials for high frequency application. They can be prepared in different configurations ranging from nanoparticles on a surface to more complex 3D composites where nanoparticles are dispersed in a matrix. The host and filler materials can be chosen according to the need of the application thus offering additional degree of freedom.

### **Quasi two dimensional metal / polymer nanocomposite**

The functional nanocomposite was prepared in two steps: drop casting of polymer and thermal evaporation of Au onto its surface. Since noble metals have higher cohesive energy compared to polymers and due to their weak polymer interaction, the evaporation results in the formation of metal nanoparticles. In the vicinity of percolation threshold, electronic transport in these nanocomposites occurs via inter-particle tunneling and the tunnel current is exponentially dependent on the inter particle separation. This exponential dependence can be utilized as a detection mechanism for a process which changes the inter-particle separation. In this dissertation precisely this mechanism has been used to monitor the strain produced by magnetostrictive material. Inter-particle separation was controlled by amount of Au evaporated which was monitored by means of *in-situ* resistance measurement. A maximum change of 6% was observed in the electrical resistance of the nanocomposite layer for strain of approximately 0.07%. The sensitivity (gauge factor) was about 80 which is two orders of magnitude higher than the commercially available metallic strain gauges and competes with semiconductor strain gauges.

Aging processes which often adversely affect the stability of sensors were also studied in detail in this thesis. In this context aging refers to deterioration of tunneling resistance of the nanocomposites over a period of time. It was observed that after six months the tunneling resistance had increased considerably to eight times of that on day one, though the QMR magnitude stayed in the same region with bit of degradation. The change in tunneling resistance appears to be characteristic of such two dimensional system which stems from the mobility of nanoparticles on the polymer matrix [84, 134]. Otherwise one should not see such a change in the tunneling resistance over the time. Embedding of Au nanoparticles into the underlying polymer was used as a tool to stabilize the nanoparticles which in turn inhibits the aging process. Embedding was done by heating the nanocomposite above glass transition temperature of the polymer. The embedded sample was also stored for six months and when remeasured, the increase in tunneling current was merely 22% as compared to eight fold increase in case of non-embedded sample. Most importantly during all this process the QMR amplitude did not change significantly. Hence, it can be said that the embedding technique can be successfully employed to stabilize the tunneling resistance over a period of time. Additionally a protective layer (e.g., PTFE) can also be deposited on top of Au nanoparticles. The sensor presented here demonstrates that the electrical resistance of the nanocomposite layer allows direct measurement of the magnetically induced strain and can thus be used as a feedback sensor for the magnetostrictive actuator.

The concept of the sensor presented here is promising for applications due to several aspects. As quantum tunneling is an exponential effect, only a small change in distance is required to obtain a relatively high signal, which gives rise to a high sensitivity and a high gauge factor. This effect is expected to be even more pronounced when the metal nanoparticles are arranged in a regular array instead of being randomly arranged as presented here. Due to its good scaling capability, the presented functional layer is able to address emerging needs of miniaturization. The functional layer can be downscaled to sub-micrometer dimensions, where other strain measurement techniques become more and more complex and costly. Furthermore, the usage of the functional polymer/Au-nanocluster layer in combination with magnetostrictive cantilever-type actuators [135, 136] has particular advantage that the functional layer is non-magnetic, therefore on one hand, it is not affected by any magnetic field present in close proximity

---

to the layer and on the other hand, does not affect the magnetic field distribution itself. It is thus very appropriate for a feedback sensor for magnetostrictive actuators which is often required for compensation of hysteresis, load and temperature effects, given that the average strain on the surface of the cantilever is in the range required by the 2-d functional layer.

In general, the presented technique provides an alternative method to detect strain. It is also applicable to other substrates, e.g., MSM single crystals that have huge magnetic field induced strains in the order of 6% [137]. This would further increase the QMR of the system significantly.

### **3D nanocomposite**

Unlike in 2D system, where metal nanoparticles are on the surface or just below the surface after embedding, in 3D nanocomposite they are incorporated in the matrix, thus it can be made into thin films of several micrometer in thickness. These nanocomposites were prepared at room temperature by co-sputtering from two sources. RF magnetron source was used for  $\text{TiO}_2$  /  $\text{SiO}_2$  and DC magnetron source for FeCo. FeCo- $\text{TiO}_2$  were evaluated with respect to tunnel magnetoresistance and FeCo- $\text{SiO}_2$  as core material for microinductors. Microstructure and magnetic properties of the nanocomposite films were characterized with respect to metal volume fraction. The metal volume fractions can be controlled by varying the sputtering power of the individual components. The need for the ceramic matrix arises because of reactions between magnetic material and the organic matrix during co-sputtering. Due to which the resulting nanocomposites are no more ferromagnetic in nature thus depriving it of the possible applications. Alternatively, sequential deposition of the ferromagnetic material and the organic material can be used to minimize the reactions.

High resolution transmission electron microscopy analysis reveals that the microstructure of the nanocomposites depend on the MVF which determines the particle size and separation. In FeCo- $\text{TiO}_2$  composites containing MVF up to 35%, FeCo nanoparticles are amorphous, whereas FeCo starts forming crystallites at MVF greater than 35% with average size about 2 nm. The finding of amorphous FeCo nanoparticles is very interesting from the fundamental point of view because FeCo is not expected to be

a glass forming alloy even at high quenching rates. The amorphous structure seems to be a result of the very small particle size and the resulting interfacial stress which can better be accommodated by an amorphous structure. Particle size distribution was also obtained by fitting the experimental magnetization curves (showing superparamagnetism) with Langevin function and log normal distribution function for the particle size. The average particle size and width of distribution increases with MVF which is characteristics of the deposition method employed.

The type of electrical transport mechanism in the composites is closely related to the morphology of the composites. Electrical resistivity changes several orders of magnitude, from  $10^6 \mu\Omega cm$  to  $10^2 \mu\Omega cm$  for 35% to 70% MVF respectively. Percolation threshold which is one of the key characteristics of composites was determined by measuring the dependence of electrical resistance vs MVF. In FeCo-TiO<sub>2</sub> for metal volume fractions below 53% the resistance increases with decrease in temperature. The typical conductivity mechanism associated with this type of behavior is of hopping type. As the MVF increases the resistivity comes down as connecting network of nanoparticles start to form and hence more paths are available for conduction through the film. The percolation threshold value depends on many factors like particle size, shape and the preparation method. Typically for such nanocomposites the percolation was found to be in the range of 50% to 60% [1, 116, 117].

Magnetization curves show distinct behavior with respect to MVF, changing from the superparamagnetic state to ferromagnetism. For FeCo-TiO<sub>2</sub> system superparamagnetic behavior was observed below 50% MVF, same phenomena was seen in FeCo-SiO<sub>2</sub> system as well. Superparamagnetic behavior requires separated single domain particles. Along with MVF the crystallites of FeCo grow in size and the separation between them decreases. This leads to the ferromagnetic exchange between the particles and the system behaves like a multidomain. Increase in the MVF would also results in coalescence between neighboring particles with multidomain structure. In the same way saturation magnetization also increases with increase in MVF as the magnetic moment increases due to increase in the size of FeCo grains.

Composite films containing MVF below 53% show decrease in electrical resistance under external magnetic field. This change was explained by spin dependent tunneling

---

process. Magnetic moments are supposed to be randomly oriented under zero magnetic field and when the external magnetic field is applied the relative orientation of the magnetization moment rotates in to parallel configuration thus increasing the tunneling probability. A maximum change of 4% was observed for 48% MVF under applied field of 0.5 T at room temperature. MR curves obey  $\Delta R/R_0 \propto -(M/M_s)^2$  relation thus suggesting the spin dependent tunneling phenomena. TMR of nanocomposites is substantially lower than TMR values reported for the TMR devices fabricated by advanced lithography techniques involving epitaxial oxide layers. Nevertheless, due to simple fabrication process, the granular TMR approach is tempting for low-cost magnetic field sensors, where highest sensitivity is not required.

For high frequency applications, the dielectric constant of the matrix must be as low as possible to avoid capacitive losses, therefore  $\text{TiO}_2$  was replaced with  $\text{SiO}_2$ . The high frequency properties were evaluated for MVF range from 48% to 70 %. It was observed that the high frequency permeability increases as the filling factor increases and the ferromagnetic resonance frequency is in the range of 2.5 to 3 GHz.

Improvements in high frequency characteristics were observed due to induced anisotropy by a static magnetic field during deposition. The hard axis permeability is about 140 and FMR around 3.1 GHz. Material quality factor Q, is quite high below 2 GHz. The imaginary part of the permeability shows a narrow peak width which is advantageous as the magnetic loss around FMR frequency depends on the line width [120].

Integration process of the high frequency material in to a magnetic device frequently involves heat treatment and microstructure undergo microstructural changes drastically modifying the functional properties. Therefore, heating experiments were performed *in-situ* in transmission electron microscope as well as *ex-situ* in vacuum. In case of FeCo- $\text{TiO}_2$  system, initially amorphous film showed formation of nanosized crystallites at temperature of 450 °C. EDX analyses performed on these crystallites indicate that they are Co crystallites. STEM-EDX elemental maps confirm the segregation of Co after annealing. TMR in heated samples (MVF 25-30%) vanishes due to a large increase in the mean particle distance and phase separation of Fe and Co. FeCo- $\text{SiO}_2$  system (MVF 53% and 70%) were annealed in vacuum in the presence of external magnetic field. Annealing was done for 60 mints in the temperature range from 200 to

400 °C. The magnetization loops become softer when compared to as prepared films with no change in coercivity. Composites with 53% MVF show an increase in permeability of about  $\approx 50\%$  with no change in the FMR frequency. However, 70% MVF films show close to three times increase in permeability but show poor quality factors due to eddy currents.

Therefore, a filling factor which is between 60 and 70 was chosen for integration of the core material into toroidal micro-inductor as when the filling factor is lesser than 53%, it results in superparamagnetic films and when it is as high as 70% upon annealing results in eddy currents. One micron thick core was optimized which has material quality factor greater than 25 at 1 GHz. The nanocomposite films were prepared without an external magnetic field during deposition as the in-plane uniaxial anisotropy will lead to interruption of field distribution in the toroids. For every 100 nm FeCo-SiO<sub>2</sub> additional SiO<sub>2</sub> of few nm in thickness were incorporated which resulted in electrical resistivity of 1800  $\mu\Omega\text{cm}$ . Skin depth at 3 GHz was found to be more than five microns. FeCo-SiO<sub>2</sub> one micron thick film was successfully integrated into toroidal micro-inductors. The inductance stays constant up to 3 GHz which is very promising. The enhancement in the inductance on addition of magnetic core is in the range of 20-30% which would not make the added processing steps worthwhile. However, magnetic volume of the present inductor is approximately 10% which can be increased. Simulations performed for thicker core material using electromagnetic field simulation tool HFSS show that the inductance increases linearly as the thickness of core material (figure 6.18). With a five micron core a threefold increase in the inductance could be possible which is very encouraging. The corresponding quality factor can also be increased by adjusting the dimensions of the vias (lowering the DC resistance).

In addition to the co-sputtering technique, nanocomposite were also fabricated from dewetting of alternate layers of metal and matrix. In future by this technique it may be possible to align the easy axis in the direction needed by introducing shape anisotropy by annealing the multilayer in a magnetic field. Another possibility of fabricating the nanocomposite, which is under development, is based on gas aggregation cluster source [138, 139]. In this technique cluster formation and the matrix deposition

---

process are separated thus it may be possible to circumvent the problem of undesired chemical reactions during co-sputtering of magnetic and organic materials.



# Bibliography

- [1] C. L. Chien, Granular magnetic solids, *Journal of Applied Physics*, 69, 8: p. 5267 (1991). 1, 6.1, 7
- [2] V. Zaporozhchenko, R. Podschun, U. Schürmann, A. Kulkarni and F. Faupel, Physico-chemical and antimicrobial properties of co-sputtered Ag-Au/PTFE nanocomposite coatings, *Nanotechnology*, 17, 19: pp. 4904–4908 (2006). 1
- [3] H. Fujimori, S. Ohnuma, N. Kobayashi and T. Masumoto, Spintronics in metal-insulator nanogranular magnetic thin films, *Journal of Magnetism and Magnetic Materials*, 304, 1: pp. 32–35 (2006). 1, 5
- [4] R. Ramprasad, P. Zurcher, M. Petras, M. Miller and P. Renaud, Magnetic properties of metallic ferromagnetic nanoparticle composites, *Journal of Applied Physics*, 96, 1: p. 519 (2004). 1, 6, 6.1, 6.4
- [5] M. Yamaguchi, K. Suezawa, K. I. Arai, Y. Takahashi, S. Kikuchi, Y. Shimada, W. D. Li, S. Tanabe and K. Ito, Microfabrication and characteristics of magnetic thin-film inductors in the ultrahigh frequency region, *Journal of Applied Physics*, 85, 11: p. 7919 (1999). 1, 6
- [6] S. Behrens, Preparation of functional magnetic nanocomposites and hybrid materials : recent progress and future directions., *Nanoscale*, 3: pp. 877–892 (2011). 1

- [7] F. Faupel, V. Zaporojtchenko, H. Greve, U. Schürmann, V. S. K. Chakravadhanula, C. Hanisch, A. Kulkarni, A. Gerber, E. Quandt and R. Podschun, Deposition of Nanocomposites by Plasmas, *Contributions to Plasma Physics*, 47, 7: pp. 537–544 (**2007**). 2.1
- [8] F. Faupel, V. Zaporojtchenko, H. Greve, U. Schürmann, H. Takele, C. Pochstein, V. S. K. Chakravadhanula, A. Biswas, A. Gerber, E. Quandt and R. Podschun, Polymer Nanocomposites for Functional Applications (Invited), in A. Hashmi, S. A. Chandra, A. C. (Eds) and S. C. S. Ed.), editors, *Electroactive Polymers - Materials and Devices, Vol. II*, volume II, pp. 78–88, Allied Publishers Pvt. Ltd. 2007 (**2007**). 2.1
- [9] V. Zaporojtchenko, T. Strunskus, H. Greve, H. Takele, C. Hanisch, V. S. K. Chakravadhanula, N. Ni, A. Gerber, E. Quandt, R. Podschun and F. Faupel, Functional Polymer Nanocomposites, *Polymers & Polymer Composites*, 16: pp. 471–481 (**2008**). 2.1
- [10] C. Hanisch, *Polymer-Metall-Nanokomposite nahe der Perkolationschwelle für sensorische Anwendungen*, Ph.D. thesis, Technische Fakultät der Christian-Albrechts-Universität zu Kiel (**2009**). 2.1
- [11] U. Schürmann, *Eigenschaften von Polymer-Silber-Nanokompositen hergestellt durch Co-Sputtern*, Ph.D. thesis, Technische Fakultät der Christian-Albrechts-Universität zu Kiel (**2006**). 2.1, 3.2.1, 3.3.1
- [12] H. Greve, *Magnetische Metall / Polymer Nanokomposite für Hochfrequenzanwendungen*, Ph.D. thesis, Technische Fakultät der Christian-Albrechts-Universität zu Kiel (**2007**). 2.1, 3.6, 3.2.1, 5, 6
- [13] M. Ohring, *Materials science of thin films*, Academic Press, 1st edition (**1992**). 2.1, 3.1.2, 3.2.1
- [14] F. Faupel, V. Zaporojtchenko, T. Strunskus, J. Erichsen, K. Dolgner and M. Kiene, Fundamental aspects of polymer metallization, in E. Sacher, editor,

- 
- Metallization of polymers 2*, pp. 73–96, Springer (**2002**). 2.1
- [15] V. Zaporojtchenko, K. Behnke, A. Thran, T. Stunskus and F. Faupe, Condensation coefficients and initial stages of growth for noble metals deposited onto chemically different polymer surfaces, *Applied Surface Science*, 144-145: pp. 355–359 (**1999**). 2.1
- [16] U. Schürmann, W. Hartung, H. Takele, V. Zaporojtchenko and F. Faupel, Controlled syntheses of Ag-polytetrafluoroethylene nanocomposite thin films by co-sputtering from two magnetron sources, *Nanotechnology*, 16, 8: pp. 1078–1082 (**2005**). 2.1, 3, 3.3.1
- [17] H. Takele, U. Schürmann, H. Greve, D. Paretkar, V. Zaporojtchenko and F. Faupe, Controlled growth of Au nanoparticles in co-evaporated metal/polymer composite films and their optical and electrical properties, *Eur. Phys. J. Appl. Phys.*, 33: pp. 83–89 (**2006**). 2.1
- [18] A. L. Efros, *Physics and Geometry of Disorder*, Mir Publishers Moscow, revised first edition (**1986**). 2.1.1
- [19] D. Stauffer and A. Aharony, *Introduction to Percolation Theory*, Taylor & Francis, 2nd revised edition (**2003**). 2.1.1, 2.2
- [20] E. Garboczi, K. Snyder and J. Douglas, Geometrical percolation threshold of overlapping ellipsoids, *Physical Review E*, 52: pp. 819–828 (**1995**). 2.3, 2.1.1
- [21] H. Takele, S. Jebril, T. Strunskus, V. Zaporojchenko, R. Adelung and F. Faupel, Tuning of electrical and structural properties of metal-polymer nanocomposite films prepared by co-evaporation technique, *Applied Physics A*, 92, 2: pp. 345–350 (**2008**). 2.1.1, 2.4
- [22] S. Honda, T. Okada, M. Nawate and M. Tokumoto, Tunneling giant magnetoresistance in heterogeneous Fe-SiO<sub>2</sub> granular films, *Physical Review B*, 56, 22: pp. 14,566–14,573 (**1997**). 2.1.1, 2.4, 5.2

- [23] S. Asakura, S. Ishio, A. Okada and H. Saito, Magnetic domain percolation of  $\text{Co}_x(\text{SiO}_2)_{100-x}$  granular films, *Journal of Magnetism and Magnetic Materials*, 240, 1-3: pp. 485–487 (**2002**). 2.1.1, 2.5, 6.1
- [24] B. D. Cullity and C. D. Graham, *Introduction to Magnetic Materials*, IEEE Press, 2nd edition (**2009**). 2.2, 2.2, 2.2, 2.4, 2.5, 6, 6.4
- [25] R. C. O’Handley, *Modern Magnetic Materials: Principle and Applications*, Wiley-Interscience (**1991**). 2.2, 2.6, 2.2, 5.2
- [26] W. Gong and H. Li, Small Particles and Quasicrystals Ultrafine particles of Fe, Co, and Ni ferromagnetic, *Journal of Applied Physics*, 69, 8: pp. 5119–5121 (**1991**). 2.1, 5.2
- [27] B. Hattink, M. García del Muro, Z. Konstantinović, X. Batlle, A. Labarta and M. Varela, Tunneling magnetoresistance in Co-ZrO(2) granular thin films, *Physical Review B*, 73, 4: pp. 1–9 (**2006**). 2.2, 2.3, 5.2
- [28] D. L. Leslie-Pelecky and R. D. Rieke, Magnetic Properties of Nanostructured Materials, *Chemistry of Materials*, 8: pp. 1770–1783 (**1996**). 2.2, 5.2, 5.2
- [29] C. G. Granqvist, Ultrafine metal particles, *Journal of Applied Physics*, 47, 5: pp. 2200–2219 (**1976**). 2.2, 5.2
- [30] C. Wang, A phenomenological theory of the granular size effect on the giant magnetoresistance of granular films, *Journal of Magnetism and Magnetic Materials*, 277, 3: pp. 273–280 (**2004**). 2.2
- [31] Z. Konstantinović, M. G. D. Muro, M. Varela, X. Batlle and A. Labarta, Particle growth mechanisms in Ag-ZrO(2) and Au-ZrO(2) granular films obtained by pulsed laser deposition., *Nanotechnology*, 17, 16: pp. 4106–4111 (**2006**). 2.2
- [32] X. Battle and A. Labarta, Finite-size effects in fine particles: magnetic and transport properties, *Journal of Applied Physics D: Applied Physics*, 35: pp.

- 
- R15–R42 (**2002**). 2.2.1
- [33] R. Skomski, RKKY interaction between nanomagnets of arbitrary shape, *Europhysics Letters (EPL)*, 48: pp. 455–460 (**1999**). 2.2.1
- [34] P. Allia, M. Knobel, P. Tiberto and F. Vinai, Magnetic properties and giant magnetoresistance of melt-spun granular Cu(100-x) - Co(x) alloys, *Physical Review B*, 52, 21: pp. 15,398–15,411 (**1995**). 2.2.1
- [35] D. Altbir, J. d’Albuquerque e Castro and P. Vargas, Magnetic coupling in metallic granular systems, *Physical review. B, Condensed matter*, 54, 10: pp. R6823–R6826 (**1996**). 2.2.1
- [36] G. Herzer, Soft Magnetic Nanocrystalline Materials, *Scripta Metallurgica et Materialia*, 33: pp. 1741–1756 (**1995**). 2.2.1
- [37] E. P. Wohlfarth, Relations between Different Modes of Acquisition of the Remanent Magnetization of Ferromagnetic Particles, *Journal of Applied Physics*, 29, 3: p. 595 (**1958**). 2.2.1
- [38] P. Kelly, K. O’Grady, P. Mayo and R. Chantrell, Switching mechanisms in cobalt-phosphorus thin films, *IEEE Transactions on Magnetism*, 25, 5: pp. 3881–3883 (**1989**). 2.2.1
- [39] O. Henkel, Remanenzverhalten und Wechselwirkungen in hartmagnetischen Teilchenkollektiven, *Physica Status Solidi (B)*, 7, 3: pp. 919–929 (**1964**). 2.2.1
- [40] R. E. Hummel, *Electronic Properties of Materials*, Springer, 3rd edition (**2001**). 2.3
- [41] J. G. Simmons, Generalized Formula for the Electric Tunnel Effect between Similar Electrodes Separated by a Thin Insulating Film, *Journal of Applied Physics*, 34, 6: p. 1793 (**1963**). 2.3

- [42] M. Julliere, Tunneling between ferromagnetic films, *Physics Letters*, 54A: pp. 225–226 (**1975**). 2.3
- [43] J.-G. Zhu and C. Park, Magnetic tunnel junctions, *materialstoday*, 9, 11: pp. 36–45 (**2006**). 2.8, 2.3
- [44] J. Inoue and S. Maekawa, Theory of tunneling magnetoresistance in granular magnetic films., *Physical review. B, Condensed matter*, 53, 18: pp. R11,927–R11,929 (**1996**). 2.3, 5, 5.3
- [45] H. Fujimori, S. Mitani and S. Ohnuma, Tunnel-type GMR in metal-nonmetal granular alloy thin films, *Materials Science and Engineering B*, 31, 1-2: pp. 219–223 (**1995**). 2.3
- [46] T. Zhu and Y. J. Wang, Enhanced tunneling magnetoresistance of Fe-Al(2)O(3) granular films in the Coulomb blockade regime, *Physical Review B*, 60, 17: pp. 11,918–11,921 (**1999**). 2.3
- [47] S. Mitani, H. Fujimori, K. Takanashi, K. Yakushiji, J.-G. Ha, S. Takahashi, S. Maekawa, S. Ohnuma, N. Kobayashi, T. Masumoto, M. Ohnuma and K. Hono, Tunnel-MR and spin electronics in metal-nonmetal granular systems, *Journal of Magnetism and Magnetic Materials*, 198-199, 1-3: pp. 179–184 (**1999**). 2.3
- [48] S. Mitani, S. Takahashi, K. Takanashi, K. Yakushiji, S. Maekawa and H. Fujimori, Enhanced magnetoresistance in insulating granular systems: evidence for higher-order tunneling, *Physical Review Letters*, 81, 13: pp. 2799–2802 (**1998**). 2.3, 2.9
- [49] S. Ju and Z.-Y. Li, Tunneling magnetoresistance in granular composites, *Journal of Applied Physics*, 92, 9: p. 5281 (**2002**). 2.3
- [50] C. Kittel, On the theory of ferromagnetic resonance absorption, *Physical Review*, 73: pp. 155–161 (**1948**). 2.4.2

- 
- [51] E. Kneller, *Ferromagnetismus*, Springer-Verlag Berlin (**1962**). 2.4.3
- [52] S. Chikazumi, *Physics of Ferromagnetism*, Oxford University press, 2nd edition (**1997**). 2.4.3, 2.5
- [53] F. Schatz, M. Hirscher, M. Schnell, G. Flik and H. Kronmüller, Magnetic anisotropy and giant magnetostriction of amorphous TbDyFe films, *Journal of Applied Physics*, 76, 9: pp. 5380–5382 (**1994**). 2.5
- [54] A. Ludwig and E. Quandt, Giant magnetostrictive thin films for applications in microelectromechanical systems (invited), *Journal of Applied Physics*, 87: pp. 4691–4695 (**2000**). 2.5
- [55] S. Bhaduri and B. Bhaduri, S, Recent Developments in Ceramic Nanocomposites, *JOM Journal of the Minerals, Metals and Materials Society*, 50: pp. 44–51 (**1998**). 3
- [56] X. Lu, G. Liang and Y. Zhang, Structure and magnetic properties of FeCo-SiO(2) nanocomposite synthesized by a novel wet chemical method, *Materials Letters*, 61, 27: pp. 4928–4931 (**2007**). 3
- [57] H. Y. Kwong, M. H. Wong, Y. W. Wong and K. H. Wong, Magnetoresistivity of cobalt-polytetrafluoroethylene granular composites, *Applied Physics Letters*, 89, 17: p. 173,109 (**2006**). 3, 5.3
- [58] Z. Konstantinović, M. García del Muro, M. Kovylyna, X. Batlle and A. Labarta, ac conductance in granular insulating Co-ZrO<sub>2</sub> thin films: A universal response (**2009**). 3
- [59] J. Park, J. Joo, S. G. Kwon, Y. Jang and T. Hyeon, Synthesis of monodisperse spherical nanocrystals., *Angewandte Chemie (International ed. in English)*, 46, 25: pp. 4630–4660 (**2007**). 3

- [60] H. Greve, A. Biswas, U. Schürmann, V. Zaporojtchenko and F. Faupel, Self-organization of ultrahigh-density Fe-Ni-Co nanocolumns in Teflon AF, *Applied Physics Letters*, 88, 12: pp. 123,103 1–2 (**2006**). 3
- [61] F. C. Krebs, Fabrication and processing of polymer solar cells: A review of printing and coating techniques, *Solar Energy Materials and Solar Cells*, 93, 4: pp. 394–412 (**2009**). 3.1.1
- [62] A. Biswas, Z. Marton, J. Kanzow, J. Kruse, V. Zaporojtchenko and F. Faupel, Controlled Generation of Ni Nanoparticles in the Capping Layers of Teflon AF by Vapor-Phase Tandem Evaporation, *Nano Letters*, 3: pp. 69–73 (**2003**). 3.1.2
- [63] B. Chapman, *Glow Discharge Processes: Sputtering and Plasma Etching*, Wiley-VCH (**1980**). 3.2.1, 3.2.1
- [64] G. Wehner and G. Anderson, *Hand book of thin film technology*, McGraw-Hill (**1970**). 3.2.1, 3.4
- [65] R. Waits, Planar magnetron sputtering, *Journal of Vacuum Science & Technology*, 15: pp. 179–187 (**1978**). 3.2.1
- [66] H. Takele, *Optical and Electrical Properties of Metal-Polymer Nanocomposites Prepared by Vapor-Phase Co-evaporation*, Ph.D. thesis, Technische Fakultät der Christian-Albrechts-Universität zu Kiel (**2007**). 3.2.1
- [67] E. Fuchs, H. Oppolzer and H. Rehme, *Particle Beam Microanalysis*, VCH (**1990**). 3.3.1, 3.3.2
- [68] D. Williams and C. Carter, *Transmission electron microscopy*, Springer Verlag (**2009**). 3.3.2
- [69] S. Foner, Versatile and Sensitive Vibrating Sample Magnetometer, *Review of Scientific Instruments*, 30: pp. 548–557 (**1959**). 3.4.1

- 
- [70] C. Bechtold, *Entwicklung von Fe(70) Pd(30)-Dünnschichtsensoren zur Bestimmung von Dehnung mittels des inversen magnetischen Formgedächtniseffektes*, Ph.D. thesis, Technische Fakultät der Christian-Albrechts-Universität zu Kiel (2010). 3.4.1
- [71] F. Hettstedt, U. Schürmann, R. Knochel and E. Quandt, Permeameter for the Characterization of Magnetic Thin Films up to 15 GHz, *2008 38th European Microwave Conference*, , October: pp. 797–800 (2008). 3.4.3, 3.11
- [72] F. Hettstedt, U. Schürmann, R. Knochel and E. Quandt, Double Coil Permeameter for the Characterization of Magnetic Materials, *2009 German Microwave Conference*, pp. 1–3 (2009). 3.4.3
- [73] F. Hettstedt, *Weichmagnetische Nanokomposite und deren Anwendungen in der Hochfrequenztechnik*, Ph.D. thesis, Technische Fakultät der Christian-Albrechts-Universität zu Kiel (2011). 3.4.3, 6.3
- [74] M. Yamaguchi, Magnetic Films for Planar Inductive Components and Devices., in M. H. Francombe, editor, *Handbook of Thin Film Devices*, Academic Press (2000). 3.4.3, 6
- [75] D. Pain, M. Ledieu, O. Acher, A. L. Adenot and F. Duverger, An improved permeameter for thin film measurements up to 6 GHz, *Journal of Applied Physics*, 85, 8: p. 5151 (1999). 3.4.3
- [76] A. Ludwig, M. Tewes, S. Glasmachers, M. Löhndorf and E. Quandt, High-frequency magnetoelastic materials for remote-interrogated stress sensors, *Journal of Magnetism and Magnetic Materials*, 242-245: pp. 1126–1131 (2002). 3.4.3
- [77] J. van Suchtelen, Product properties: A new application of composite materials, *Philips Res. Repts*, 27: pp. 28–37 (1972). 4.1
- [78] S. Dong, J.-F. Li and D. Viehland, Ultrahigh magnetic field sensitivity in laminates of TERFENOL-D and  $\text{Pb}[\text{Mg}(1/3)\text{Nb}(2/3)]\text{O}(3)\text{-PbTiO}(3)$  crystals, *Ap-*

- plied Physics Letters*, 83, 11: pp. 2265–2267 (**2003**). 4.1
- [79] S. Stein, M. Wuttig, D. Viehland and E. Quandt, Magnetoelectric effect in sputtered composites, *Journal of Applied Physics*, 97, 10: p. 10Q301 (**2005**). 4.1
- [80] M. Wun-Fogle, J. Restorff, K. Leung, J. Cullen and E. Clark, A, Magnetostriction of Terfenol-D heat treated under compressive stress, *IEEE Transactions on Magnetics*, 35, 5: pp. 3817–3819 (**1999**). 4.2
- [81] D. Meyners, T. von Hofe, M. Vieth, M. Rühlig, S. Schmitt and E. Quandt, Pressure sensor based on magnetic tunnel junctions, *Journal of Applied Physics*, 105, 7: p. 07C914 (**2009**). 4.2.1
- [82] C. Farcau, H. Moreira, B. Viallet, J. Grisolia, D. Ciuculescu-Pradines, C. Amiens and L. Ressier, Monolayered Wires of Gold Colloidal Nanoparticles for High-Sensitivity Strain Sensing, *The Journal of Physical Chemistry C*, 115, 30: pp. 14,494–14,499 (**2011**). 4.2.1
- [83] J. Herrmann, K.-H. Müller, T. Reda, G. R. Baxter, B. Raguse, G. J. J. B. de Groot, R. Chai, M. Roberts and L. Wiczorek, Nanoparticle films as sensitive strain gauges, *Applied Physics Letters*, 91, 18: p. 183,105 (**2007**). 4.2.1
- [84] C. Hanisch, A. Kulkarni, V. Zaporozhchenko and F. Faupel, Polymer-metal nanocomposites with 2-dimensional Au nanoparticle arrays for sensoric applications, *Journal of Physics: Conference Series*, 100, 5: p. 052,043 (**2008**). 4.2.3, 7
- [85] C. Pakula, V. Zaporozhchenko, T. Strunskus, D. Zargarani, R. Herges and F. Faupel, Reversible light-controlled conductance switching of azobenzene-based metal/polymer nanocomposites., *Nanotechnology*, 21, 46: p. 465,201 (**2010**). 4.2.3

- [86] F. Faupel, R. Willecke and A. Thran, Diffusion of Metals in Polymers, *Materials Science and Engineering, R22*, 22 (1998). 4.2.3
- [87] T. Strunskus, V. Zaporozhchenko, K. Behnke, C. v. Bechtolsheim and F. Faupel, Tailoring the Morphology of Metal/Polymer Interfaces, *Advanced Engineering Materials*, 2, 8: pp. 489–492 (2000). 4.2.3
- [88] R. J. Andrews and E. A. Grulke, *Polymer Handbook vol VI*, Wiley-Interscience: New York, 4th edition (1999). 4.2.3
- [89] F. Battiston, J.-P. Ramseyer, H. Lang, M. Baller, C. Gerber, J. Gimzewski, E. Meyer and H.-J. Güntherodt, A chemical sensor based on a microfabricated cantilever array with simultaneous resonance-frequency and bending readout, *Sensors and Actuators B: Chemical*, 77, 1-2: pp. 122–131 (2001). 4.3
- [90] T. Akiyama, U. Staufer, N. F. de Rooij, D. Lange, C. Hagleitner, O. Brand, H. Baltes, A. Tonin and H. R. Hidber, Integrated atomic force microscopy array probe with metal-oxide-semiconductor field effect transistor stress sensor, thermal bimorph actuator, and on-chip complementary metal-oxide-semiconductor electronics, *Journal of Vacuum Science & Technology B: Microelectronics and Nanometer Structures*, 18, 6: p. 2669 (2000). 4.3
- [91] S. B. Gittlemann, J. Y. Goldstein, Magnetic properties of granular Nickel films, *Physical Review B*, 5: pp. 3609–3621 (1972). 5
- [92] J. Helman and B. Abeles, Tunneling of Spin-Polarized Electrons and Magnetoresistance in Granular Ni Films, *Physical Review Letters*, 37: pp. 1429–1432 (1976). 5, 5.3
- [93] S. Ohnuma, M. Ohnuma, H. Fujimori and T. Masumoto, Metal-insulator type nano-granular soft magnetic thin films investigations on mechanism and applications, *Journal of Magnetism and Magnetic Materials*, 310, 2: pp. 2503–2509 (2007). 5, 6

- [94] K. Yakushiji, S. Mitani, F. Ernult, K. Takanashi and H. Fujimori, Spin-dependent tunneling and Coulomb blockade in ferromagnetic nanoparticles, *Physics Reports*, 451, 1: pp. 1–35 (**2007**). 5
- [95] A. Kulkarni, V. S. K. Chakravadhanula, V. Duppel, D. Meyners, V. Zaporozhchenko, T. Strunskus, L. Kienle, E. Quandt and F. Faupel, Morphological and magnetic properties of TiO<sub>2</sub>/Fe<sub>50</sub>Co<sub>50</sub> composite films, *Journal of Materials Science*, 46, 13: pp. 4638–4645 (**2011**). 5
- [96] A. Díaz-Ortiz, R. Drautz, M. Fähnle, H. Dosch and J. Sanchez, Structure and magnetism in bcc-based iron-cobalt alloys, *Physical Review B*, 73, 22 (**2006**). 5.1
- [97] K. Seemann, H. Leiste and V. Bekker, A new generation of CMOS-compatible high frequency micro-inductors with ferromagnetic cores: Theory, fabrication and characterisation, *Journal of Magnetism and Magnetic Materials*, 302, 2: pp. 321–326 (**2006**). 5.1.1
- [98] C. Wang, P. Zhang, L. Zheng, X. Xiao and Y. Rong, Influence of annealing on microstructure and magnetic-transport of FeCo-Al(2)O(3) nanogranular films, *Thin Solid Films*, 516, 10: pp. 3422–3430 (**2008**). 5.1.1, 5.3
- [99] E. A. Owen and D. M. Jones, Effect of Grain Size on the Crystal Structure of Cobalt, *Proceedings of the Physical Society. Section B*, 67, 6: pp. 456–466 (**1954**). 5.1.1
- [100] G. Xiao and C. L. Chien, Giant magnetic coercivity and percolation effects in granular Fe-(SiO<sub>2</sub>) solids, *Applied Physics Letters*, 51, 16: p. 1280 (**1987**). 5.2
- [101] S. S. P. Parkin, C. Kaiser, A. Panchula, P. M. Rice, B. Hughes, M. Samant and S.-H. Yang, Giant tunnelling magnetoresistance at room temperature with MgO (100) tunnel barriers., *Nature materials*, 3, 12: pp. 862–7 (**2004**). 5.3.1

- [102] Y. Shimada, M. Yamaguchi, S. Ohnuma, T. Itoh, S. Ikeda and H. Nagura, Granular thin films with high RF permeability, *IEEE Transactions on Magnetics*, 39, 5: pp. 3052–3056 (**2003**). 6
- [103] I. Fergen, K. Seemann, A. Weth and A. Schüppen, Soft ferromagnetic thin films for high frequency applications, *Journal of Magnetism and Magnetic Materials*, 242-245: pp. 146–151 (**2002**). 6
- [104] D. S. Gardner, G. Schrom, P. Hazucha, F. Paillet, T. Karnik and S. Borkar, Integrated On-Chip Inductors With Magnetic Films, *IEEE Transactions on Magnetics*, 43, 6: pp. 2615–2617 (**2007**). 6
- [105] M. Yamaguchi, M. Baba and K.-I. Arai, Sandwich-type ferromagnetic RF integrated inductor, *IEEE Transactions on Microwave Theory and Techniques*, 49, 12: pp. 2331–2335 (**2001**). 6
- [106] M. Senda and O. Ishii, High frequency magnetic properties of CoFe/SiO/sub 2/ multilayer film with the inverse magnetostrictive effect, *IEEE Transactions on Magnetics*, 30: pp. 155–158 (**1994**). 6
- [107] W. P. Jayasekara, J. A. Bain and M. H. Kryder, High Frequency Initial Permeability of NiFe and FeAlN, *IEEE Transactions on Magnetics*, 34, 4: pp. 1438–1440 (**1998**). 6
- [108] M. Frommberger, A. Ludwig, A. Sehrbrock and E. Quandt, High-Frequency Magnetic Properties of FeCoBsi/SiO<sub>2</sub> and (FeCo/CoB)/SiO<sub>2</sub> Multilayer Thin Films, *IEEE Transactions on Magnetics*, 39, 5: pp. 3166–3168 (**2003**). 6
- [109] F. Hettstedt, U. Schürmann, R. Knöchel and E. Quandt, Toroid Microinductors Using Segmented Magnetic Cores, in *IMS*, pp. 1348–1351 (**2010**). 6
- [110] S. Ohnuma, N. Kobayashi, T. Masumoto, S. Mitani and H. Fujimori, Magnetostriction and soft magnetic properties of (Co<sub>1-x</sub>Fe<sub>x</sub>)-Al-O granular films with high electrical resistivity, *Journal of Applied Physics*, 85, 8: p. 4574 (**1999**). 6

- [111] S. Ge, D. Yao, M. Yamaguchi, X. Yang, H. Zuo, T. Ishii, D. Zhou and F. Li, Microstructure and magnetism of FeCo-SiO(2) nano-granular films for high frequency application, *Journal of Physics D: Applied Physics*, 40: pp. 3660–3664 (2007). 6
- [112] S. Ohnuma, H. Fujimori, T. Masumoto, X. Y. Xiong, D. H. Ping and K. Hono, FeCo-Zr-O nanogranular soft-magnetic thin films with a high magnetic flux density, *Applied Physics Letters*, 82, 6: p. 946 (2003). 6
- [113] L. Li, A. M. Crawford, S. X. Wang, A. F. Marshall, M. Mao, T. Schneider and R. Bubber, Soft magnetic granular material Co-Fe-Hf-O for micromagnetic device applications, *Journal of Applied Physics*, 97: p. 10F907 (2005). 6
- [114] J. Huijbregtse, F. Roozeboom, J. Sietsma, J. Donkers, T. Kuiper and E. van de Riet, High-frequency permeability of soft-magnetic Fe-Hf-O films with high resistivity, *Journal of Applied Physics*, 83, 3: p. 1569 (1998). 6
- [115] M. Frommberger, J. Mccord and E. Quandt, Crossed anisotropy magnetic cores for integrated inductors, *Journal of Magnetism and Magnetic Materials*, 290-291: pp. 1487–1490 (2005). 6
- [116] B. Abeles, *Applied Solid State Science: Advances in Materials and Device Research*, Academic, New York (1976). 6.1, 7
- [117] B. Abeles, P. Sheng, M. Coutts and Y. Arie, Structural and electrical properties of granular metal films, *Advances in Physics*, 24, 3: pp. 407–461 (1975). 6.1, 7
- [118] G. Rieger, G. Rupp, G. Gieres, R. Losehand, W. Hartung, W. Maass and W. Ocker, High frequency performance of laminated soft magnetic films (NiFe, FeAlN, and amorphous CoFeBSi) in external fields, *Journal of Applied Physics*, 91, 10: p. 8447 (2002). 6.1, 6.1
- [119] K. Kempter and H. Hoffmann, Investigation of the Structure of Ferromagnetic Films by Means of the Differential Susceptibility, *Physica Status Solidi (B)*, 34,

- 
- 1: pp. 237–249 (**1969**). 6.1
- [120] K. Ikeda, CoFeSiO/SiO<sub>2</sub> Multilayer Granular Films With Very Narrow Ferromagnetic Resonant Linewidth, *IEEE Transactions on Magnetics*, 45, 10: pp. 4290–4293 (**2009**). 6.1, 7
- [121] H. Greve, C. Pochstein, H. Takele, V. Zaporojtchenko, F. Faupel, A. Gerber, M. Frommberger and E. Quandt, Nanostructured magnetic Fe-Ni-Co/Teflon multilayers for high-frequency applications in the gigahertz range, *Applied Physics Letters*, 89, 24: pp. 242,501 1–3 (**2006**). 6.2
- [122] F. Faupel, V. Zaporojtchenko, T. Strunskus and M. Elbahri, Metal-Polymer Nanocomposites for Functional Applications, *Advanced Engineering Materials*, 12: pp. 1177–1190 (**2010**). 6.2
- [123] M. Frommberger, C. Schmutz, M. Tewes, J. McCord, W. Hartung, R. Losehand and E. Quandt, Integration of crossed anisotropy magnetic core into toroidal thin-film inductors, *IEEE Transactions on Microwave Theory and Techniques*, 53, 6: pp. 2096–2100 (**2005**). 6.3
- [124] U. Schürmann, A. Gerber, A. Kulkarni, F. Hettstedt, V. Zaporojtchenko, R. Knöchel, F. Faupel and E. Quandt, Fabrication of Toroidal Microinductors for RF Applications, *IEEE Transactions on Magnetics*, 45, 10: pp. 4770–4772 (**2009**). 6.3, 6.3
- [125] D. S. Gardner, G. Schrom, F. Paillet, B. Jamieson, T. Karnik and S. Borkar, Review of On-Chip Inductor Structures With Magnetic Films, *IEEE Transactions on Magnetics*, 45, 10: pp. 4760–4766 (**2009**). 6.17, 6.3
- [126] S. A. Maier, P. G. Kik, H. A. Atwater, S. Meltzer, E. Harel, B. E. Koel and A. A. G. Requicha, Local detection of electromagnetic energy transport below the diffraction limit in metal nanoparticle plasmon waveguides., *Nature materials*, 2, 4: pp. 229–32 (**2003**). 6.4

- [127] J. Spadavecchia, P. Prete, N. Lovergine, L. Tapfer and R. Rella, Au nanoparticles prepared by physical method on Si and sapphire substrates for biosensor applications., *The journal of physical chemistry. B*, 109, 37: pp. 17,347–17,349 (2005). 6.4
- [128] C. Favazza, J. Trice, a. K. Gangopadhyay, H. Garcia, R. Sureshkumar and R. Kalyanaraman, Nanoparticle ordering by dewetting of Co on SiO<sub>2</sub>, *Journal of Electronic Materials*, 35, 8: pp. 1618–1620 (2006). 6.4
- [129] R. Felici, M. Jeutter, N, V. Mussi, F. Buatier de Mongeot, C. Boragno, U. Valbusa, A. Toma, Y. Wei Zhang, C. Rau and K. Robinson, I, In situ study of the dewetting behavior of Ni-films on oxidized Si(001) by GISAXS, *Surface Science*, 601, 18: pp. 4526–4530 (2007). 6.4
- [130] C. M. Müller, F. C. F. Mornaghini and R. Spolenak, Ordered arrays of faceted gold nanoparticles obtained by dewetting and nanosphere lithography, *Nanotechnology*, 19, 48: p. 485,306 (2008). 6.4
- [131] Y.-J. Oh, C. a. Ross, Y. S. Jung, Y. Wang and C. V. Thompson, Cobalt nanoparticle arrays made by templated solid-state dewetting., *Small*, 5, 7: pp. 860–5 (2009). 6.4
- [132] J. Bischof, D. Scherer, S. Herminghaus and P. Leiderer, Dewetting Modes of Thin Metallic Films: Nucleation of Holes and Spinodal Dewetting., *Physical review letters*, 77, 8: pp. 1536–1539 (1996). 6.4
- [133] M. Ishino, M. Koike, M. Kanehira, F. Satou, M. Terauchi and K. Sano, Thermal stability of Co/SiO<sub>2</sub> multilayers for use in the soft x-ray region, *Journal of Applied Physics*, 102, 2: p. 023,513 (2007). 6.4
- [134] C. Hanisch, N. Ni, A. Kulkarni, V. Zaporojtchenko, T. Strunskus and F. Faupel, Fast electrical response to volatile organic compounds of 2D Au nanoparticle layers embedded into polymers, *Journal of Materials Science*, 46, 2: pp. 438–445 (2010). 7

- [135] H. J. Mamin, B. A. Gurney, D. R. Wilhoit and V. S. Speriosu, High sensitivity spin-valve strain sensor, *Applied Physics Letters*, 72, 24: p. 3220 (**1998**). 7
- [136] E. Quandt, Magnetostrictive actuation in microsystems, *Sensors and Actuators A: Physical*, 81, 1-3: pp. 275–280 (**2000**). 7
- [137] S. J. Murray, M. Marioni, P. G. Tello, S. M. Allen and R. C. O’Handley, Giant magnetic-field-induced strain in Ni-Mn-Ga crystals: experimental results and modeling, *Journal of Magnetism and Magnetic Materials*, 220-230: pp. 945–947 (**2001**). 7
- [138] B. Gojdka, V. Hrkac, T. Strunskus, V. Zaporozhchenko, L. Kienle and F. Faupel, Study of cobalt clusters with very narrow size distribution deposited by high-rate cluster source., *Nanotechnology*, 22: p. 465,704 (**2011**). 7
- [139] T. Peter, M. Wegner, V. Zaporozhchenko, T. Strunskus, S. Bornholdt, H. Kersten and F. Faupel, Metal/polymer nanocomposite thin films prepared by plasma polymerization and high pressure magnetron sputtering, *Surface and Coatings Technology*, 205: pp. S38–S41 (**2011**). 7



## List of Publications

1. A. Kulkarni, B. Henkel, C. Bechtold, V. Zaporojtchenko, T. Strunskus, E. Quandt and F. Faupel. Monitoring magnetostriction by a quantum tunneling strain sensor. *Submitted to Sensors and Actuators: A. Physical*.
2. A. Kulkarni, V. S. K. Chakravadhanula, V. Duppel, D. Meyners, V. Zaporojtchenko, T. Strunskus, L. Kienle, E. Quandt and F. Faupel. Morphological and magnetic properties of TiO<sub>2</sub>/Fe<sub>50</sub>Co<sub>50</sub> composite films. *Journal of Material Science*, 46: pp. 4638-4645 **2011**.
3. V. S. K. Chakravadhanula, T. Hrkac, V. Zaporojtchenko, R. Podschun, V. G. Kotnur, A. Kulkarni, T. Strunskus, L. Kienle, F. Faupel. Nanostructural and functional properties of Ag-TiO<sub>2</sub> coatings prepared by co-sputtering deposition technique. *Journal of Nanoscience and Nanotechnology*, 11: pp. 1-7 **2011**.
4. C. Hanisch, N. Ni, A. Kulkarni, V. Zaporojtchenko, T. Strunskus and F. Faupel. Fast electrical response to volatile organic compounds of 2D Au nanoparticle layers embedded into polymers. *Journal of Material Science*, 46: pp. 438-445 **2010**.
5. V.S.K. Chakravadhanula, A. Kulkarni, A. Lotnyk, V. Zaporotchenko, F. Faupel and L. Kienle. Real Structure of FeCo-TiO<sub>2</sub> Nanocomposites. *In Zeitschrift für anorganische und allgemeine Chemie*, 636: p. 2090 **2010**.
6. V.S.K. Chakravadhanula, A. Kulkarni, A. Lotnyk, V. Duppel, V. Zaporotchenko, L. Kienle and F. Faupel. Morphological properties of TiO<sub>2</sub>/Fe<sub>50</sub>Co<sub>50</sub> composite

- films. *In Microscopy Conference 2009 in Graz (Multinational Conference on Microscopy and Dreiländertagung)*, 149-150, **2009**.
7. U. Schürmann, A. Gerber, A. Kulkarni, F. Hettstedt, V. Zaporojtchenko, R. Knöchel, F. Faupel, and E. Quandt. Fabrication of Toroidal Microinductors for RF Applications. *IEEE Transactions on Magnetics*, 45: pp. 4770-4772 **2009**.
  8. H. Takele, A. Kulkarni, S. Jebiril, V.S.K. Chakravadhanula, C. Hanisch, T. Strunskus, V. Zaporojtchenko and F. Faupel. Plasmonic properties of vapor-deposited polymer composites containing Ag nanoparticles and their changes upon annealing. *Journal of Physics D: Applied Physics*, 41 **2008**.
  9. C. Hanisch, A. Kulkarni, V. Zaporojtchenko and F. Faupel. Polymer-metal nanocomposites with 2-dimensional Au nanoparticle arrays for sensoric applications. *Journal of Physics: Conference Series*, 100, 52043 **2008**.
  10. F. Faupel, V. Zaporojtchenko, H. Greve, U. Schürmann, C. Hanisch, V.S.K. Chakravadhanula, A. Kulkarni, A. Gerber, E. Quandt and R. Podschun. Deposition of nanocomposites by plasmas. *Contributions to Plasma Physics*, 47: pp. 537-544 **2007**.
  11. V. Zaporojtchenko, R. Podschun, U. Schürmann, A. Kulkarni and F. Faupel. Physico-chemical and antimicrobial properties of co-sputtered Ag-Au/PTFE nanocomposite coatings. *Nanotechnology*, 17: pp. 4904-4908 **2006**.

# Abbreviations

CMOS	Complementary symmetry metal oxide semiconductor
DC	Direct current
EDX	Energy-dispersive X-ray spectroscopy
EELS	Electron energy loss spectroscopy
FMR	Ferromagnetic resonance
GMR	Giant magnetoresistance
HF	High Frequency
MMIC	Monolithic microwave integrated circuit
MTJ	Metal tunnel junction
MVF	Metal volume fraction
PVD	Physical vapor deposition
QMR	Quasi magnetoresistance
SAED	Selected area electron diffraction
SEM	Scanning electron microscopy
TEM	Transmission electron microscopy
TMR	Tunnel magnetoresistance
VSM	Vibrating sample magnetometer



# Acknowledgments

I express my deep gratitude to Prof. Dr. Franz Faupel, foremost for his trust, kindness and for offering me the opportunity to pursue PhD under his guidance. I benefited immensely from his scientific inputs during our numerous discussions. His door was always open for help on work related as well as personal issues. His positive attitude and highest standards will remain benchmark to me throughout my life.

Dr. Vladimir Zaporojtchenko, for offering me HiWi which was leading step towards developing my interest in this fascinating field. I also thank him for supervision and advice during this work. My sincere thanks to Dr. Thomas Strunskus for his friendly and supportive nature and providing valuable inputs to this work.

Special thanks to Dipl.-Ing. (FH) Stefan Rehders for his quick, perfect engineering solutions and design and also for design and construction of the PVD equipment and to Christoph Ochmann. Not to forget Dipl.-Ing.(FH) Rainer Kloth because of whom we could access the server any time and anywhere making life easier.

I would like to thank Prof. Dr. Klaus Rätzke for his timely practical advices in crisis situations and also for a friendly office environment during my opportunity to share office space with him.

I thank M.Sc. Bodo Henkel for his valuable contribution to this work through his Master thesis. M.Sc. Arnim Schuchardt for experiments and numerous friendly talks. Dr. rer. nat. Ulrich Schürmann and Dr.-Ing. Henry Greve for knowledge transfer and proof-reading.

I would like to thank Prof. Dr.-Ing. Eckhard Quandt profusely for his help and cooperation through joint projects and support through wonderful facilities built by his group. Almost half of my PhD time was spent in his group utilizing the facilities. I am also thankful to him for sharing his scientific knowledge during various project meetings.

I thank Dr. Dirk Meyners for his time and contribution towards publication of my results. I also thank Dr. Thomas Von Hofe for the fabrication of toroidal micro-inductors and Dr.-Ing. Christoph Bechtold for our joint subproject.

I am also grateful to Prof. Dr. Lorenz Kienle for discussions in understanding the TEM results and also for his keen involvement. Special thanks to Dr.-Ing. Venkata Sai Kiran Chakravadhanula not only for TEM analysis, but for being a good friend.

Many thanks to Prof. Dr.-Ing. Reinhard Knöchel for collaboration and sharing his knowledge during discussions and project meetings. Special thanks to Dr.-Ing. Falk Hettstedt and Denis Baron for numerous high frequency measurements and for their accommodative nature.

My sincere thanks to Prof. Dr. Jeffrey McCord for his timely crucial help in understanding certain concepts.

I would like to thank each and every member of Institute for Materials Science-Multicomponent Materials for very fantastic and happy environment. Especially Dipl.-Phys. Björn Gojdka, Dipl.-Phys. Tilo Peter and Dr. Christina Pakula and M.Sc. Sri Wahyuni Basuki for their friendship.

Last but not least my parents, agreeing with my decision to come Germany and their constant support and my wife who left her lucrative job back home to come here. I would also like to thank Madhu and Angela for making me feel at home in Kiel. Many thanks to all the people who have directly or indirectly contributed to my growth.